

All-Optical Processing of Optical-Network Signals using Distributed Feedback Amplifiers

by

Drew N. Maywar

Submitted in Partial Fulfillment
of the
Requirements for the Degree
Doctor of Philosophy

Supervised by
Professor Govind P. Agrawal

The Institute of Optics
The College
School of Engineering and Applied Sciences

University of Rochester
Rochester, New York

2000

To Rie

Curriculum Vitae

The author was born in Port Huron, Michigan, on March 1st, 1970. He began his undergraduate studies in 1988 at the University of Rochester. During the summer of 1990, he studied the Japanese language at the East Asian Summer Language Institute at Indiana University. He then received a Take-Five Scholarship from the University of Rochester to study the Japanese language and culture at Nanzan University, Japan, for the 1991–1992 academic year. He received the B.S. degree in optics with high distinction and the B.A. degree in religion with honors and highest distinction in 1993.

The author received a Fulbright Fellowship in 1993 for a year of study at Osaka University, Japan. His scientific research at Institute of Laser Engineering was on the temperature dependence of gain in Nd:glass laser amplifiers, and his language studies focused on technical Japanese, kanji, and the Osaka dialect.

The author began his graduate studies in 1994 at the Institute of Optics, University of Rochester. During the summer of 1995 and the following academic year, he studied the fabrication of complex-coupled distributed feedback lasers in the laboratory of Professor Thomas G. Brown. In the summer of 1996, he began his doctoral re-

search on distributed feedback semiconductor optical amplifiers under the direction of Professor Govind P. Agrawal. The author received the M.S. degree in optics in 1997, with a concentration in laser engineering. For one year beginning in October 1998, he performed a portion of his doctoral research under the guidance of Professor Yoshiaki Nakano at the University of Tokyo, as a recipient of a Dissertation Enhancement Award from the U.S. National Science Foundation.

Publications

- G. P. Agrawal and D. N. Maywar, “Semiconductor Optical Amplifiers with Bragg Gratings,” (chapter 10) in *Nonlinear Photonic Crystals*, B. Eggleton and D. Slusher, Eds., Springer-Verlag, in preparation.
- D. N. Maywar, G. P. Agrawal, and Y. Nakano, “All-Optical Hysteresis Control via Cross-Phase Modulation in Semiconductor Optical Amplifiers,” submitted to *J. Opt. Soc. Am. B* (2000).
- D. N. Maywar, Y. Nakano, and G. P. Agrawal, “1.3-to-1.5 μm Wavelength Conversion by Optically Pumping a Distributed Feedback Amplifier, *IEEE Photonics Tech. Lett.* **12**, 858–860 (2000).
- D. N. Maywar, G. P. Agrawal, and Y. Nakano, “Robust Optical Control of an Optical-Amplifier-Based Flip-Flop,” *Optics Express* **6**, 75–80 (2000).
- D. N. Maywar and G. P. Agrawal, “Low-Power All-Optical Switching in Active Semiconductor Chirped Periodic Structures,” *Optics Express* **3**, 440–446 (1998).
- D. N. Maywar and G. P. Agrawal, “Effect of Chirped Gratings on Reflective Optical Bistability in DFB Semiconductor Laser Amplifiers,” *IEEE J. Quantum Electron.*, **34**, 2364–2370 (1998).
- D. N. Maywar and G. P. Agrawal, “Transfer-Matrix Analysis of Optical Bistability in DFB Semiconductor Laser Amplifiers with Nonuniform Gratings,” *IEEE J. Quantum Electron.*, **33**, 2029–2037 (1997).

Presentations

- D. N. Maywar, G. P. Agrawal, and Y. Nakano, “Control of Nonlinear Index Change in Semiconductor Laser Amplifiers for Signal Processing,” OSA Annual Meeting, Rhode Island, October 2000.
- D. N. Maywar, Govind P. Agrawal, Y. Nakano, “Robust All-Optical Control of a Semiconductor Optical Amplifier Flip–Flop,” Optical Amplifiers and their Applications, Quebec, CA, July 2000.
- D. N. Maywar, Govind P. Agrawal, Y. Nakano, “Semiconductor Optical Memory Based on a DFB Amplifier,” IEICE Conference, Osaka, Japan, November 1999.
- D. N. Maywar, G. P. Agrawal, and Y. Nakano, “Wavelength Conversion Using an Optical Gain-Pump,” IEICE Conference, Chitose, Japan, August 1999.
- D. N. Maywar, Y. Nakano, and G. P. Agrawal, “All-Optical Set and Reset of a Semiconductor-Optical-Amplifier-Based Flip–Flop,” Post-Deadline Paper, Optical Amplifiers and their Applications, Nara, Japan, June 1999.
- D. N. Maywar, G. P. Agrawal, and Y. Nakano, “Optical Switching and Memory in Chirped-Grating DFB Amplifiers,” IEICE Conference, Osaka, Japan, January 1999.
- D. N. Maywar and G. P. Agrawal, “High-Contrast All-Optical Switching in Chirped-Grating DFB Amplifiers,” OSA Annual Meeting, Baltimore, MD, October 1998.
- G. P. Agrawal and D. N. Maywar, “All-Optical Switching with Chirped Gratings in Semiconductor Optical Amplifiers,” Invited Talk, Workshop on Novel Solitons and Nonlinear Periodic Structures, Victoria, British Columbia, Canada, March 1998.
- D. N. Maywar and G. P. Agrawal, “Low-Threshold Optical Switching in $\lambda/4$ -shifted DFB Amplifiers with Chirped Gratings,” OSA Annual Meeting, Long Beach, California, October 1997.

Patents

- D. N. Maywar, Y. Nakano, and G. P. Agrawal, “All-Optical Flip–Flop Device,” U.S. Patent Application No. 2-11150-904, filed June 2000, pending.
- D. N. Maywar, Y. Nakano, and G. P. Agrawal, “All-Optical Flip–Flop Device Using a Resonant-Type Semiconductor Optical Amplifier,” Japanese Patent Application No. 11-351397, filed December 1999, pending.

Acknowledgments

I am deeply grateful to Professor Govind Agrawal for a multi-faceted and rewarding doctoral experience. He shared a tremendous amount of time with me — I value our conversations on physics, mathematics, modeling, time budgeting, and on the process and techniques of writing technical papers. I am indebted to the flexibility and encouragement he provided to explore many aspects of research, including paper writing, conference presentations, patents, and overseas research.

I am privileged to have spent a year with Professor Yoshiaki Nakano at the University of Tokyo. I am thankful to him for the great deal of time he spent with me, and for supporting and believing in me whole heartedly; flip-flop experiments were successful because of his enthusiastic support throughout the year.

I thank Fouad El-Diasty for his technical assistance and for sharing with me his joy of experiments and approach to research.

I am grateful to Professor Thomas Brown for introducing me to distributed feedback and to semiconductor lasers.

I greatly appreciate the help that the staff at the Institute of Optics has provided during my graduate studies. In particular, I would like to thank Brian McIntyre and

Don Schertler for their Macintosh help and humor. Also, I am very grateful to Joan Christian for helping me prepare this thesis and for relaying the NSF funds to me while I was in Tokyo, which involved monthly paper work and trips to my Rochester bank.

I acknowledge financial support from the Institute of Optics, the Rochester Theory Center (RTC), the U.S. Department of Education, and the National Science Foundation (NSF), which funded the year in Tokyo. I am grateful to Professor Agrawal and the RTC for covering journal publication charges, and to Professor Agrawal, Professor Nakano and the University of Tokyo, and New Focus for providing travel funds for conferences.

I thank John Marciante, Rene-Jean Essiambre, Stojan Radic, and Guido van Tartwijk for their friendship, support, and lively group meetings during my first two years of doctoral research. Stojan and Guido, in particular, were instrumental in starting my education on bistability and semiconductor physics, respectively. I also thank Zhi Liao and Taras Lakoba for their good humor during the final year.

I am grateful for the friendships made with my classmates at the Institute of Optics. I especially thank Luis de Araujo, whose companionship greatly eased the pain of the first year, and was a treasure throughout the whole graduate program. I also thank David Aronstein, a great friend and inspiration to me. He has a wonderful grasp on math and physics, matched by an ability to explain them. I am very grateful for his help in preparation for and during my year in Tokyo, and in proofreading and

formatting this thesis. I enjoyed his good cheer, perspective, and sense of humor, all of which I will miss very much.

I am grateful to the members of Professor Nakano's research group for welcoming me. In particular, I thank Daisuke Inoue, Masaki Kato, and Gernot Schlögl for their technical assistance. I am indebted to M. Funabashi, T. Yamaguchi, K. Shimizu, Y. Katagiri, and Byongjin Ma for vital experimental equipment, and thank M. Tsurusawa for his encouragement of the flip-flop experiment. I also thank Takuro Tajima for his companionship, and thank Gernot for joining me in renovating Room 302 and for helping me wrap up.

I thank Rick Robbins — his phone calls and visits to Rochester and Tokyo brought a fresh perspective and much-needed energy.

I thank the architects of Whipple Park for creating such a beautiful and nurturing environment.

I am deeply grateful to my mom and dad for encouraging me to pursue my education, for teaching me the value of experiences, and for their love. Phone calls and holiday gatherings with my mom, dad, my brother Eric, and my sister Donna have meant a lot to me.

I am blessed to have become father to Ian James during graduate school. I thank him for his company, laughter, and love.

Most of all, I thank my wife, Rie. She has graced my life with her support, understanding, and love. I thank her for her sacrifice as I pursued my goals and

dreams in graduate school. Rie, I love you very much, and hope to return such generosity to you in our new life together.

Abstract

We study the nonlinear response and signal-processing capabilities of distributed feedback semiconductor optical amplifiers, and seek to advance their application to optical communication networks.

Bistability occurring for optical signals tuned near a Bragg resonance is useful for switching and memory applications, but traditionally exhibits a limited wavelength range. We relax this constraint by varying the grating pitch along the length of the distributed feedback amplifier. A transfer-matrix method is developed for simulating this improvement, and for studying changes in the shape of the hysteresis curve throughout this wavelength range. We predict a new hysteresis-curve shape on reflection, and show how the grating-pitch variation can suppress or enhance this shape.

Optical memory based on bistability is useful for sequential signal-processing applications, but previous control techniques operate with wavelengths only in the vicinity of the bistable-signal wavelength. We propose, model, and demonstrate control techniques via auxiliary optical signals that exhibit a very wide wavelength range. Set and reset signals vary the refractive index in opposite ways and shift the upward- and downward-switching thresholds, respectively, of the hysteresis curve through the

holding-beam input power, which is kept constant. We develop a numerical model and an experimental system to investigate the performance of the all-optical flip-flop pertaining to speed, power, polarization, and response to back-to-back ‘set’ pulses. We propose and numerically simulate a sequential processing application to fiber-optic networks — data format conversion from high-speed, return-to-zero signals to low-speed, non-return-to-zero signals.

We demonstrate data-wavelength conversion to a signal wavelength of 1547 nm (in the vicinity of the Bragg wavelength) from initial data signals at 1306 nm, 1466 nm, and 1560 nm. This research demonstrates that cross-phase-modulation-based conversion using signals that generate charge carriers (e.g., those at 1306 and 1466 nm) can be implemented in gain-biased amplifiers, a principle that is applicable to other semiconductor-optical-amplifier-based data-wavelength converters. We also demonstrate how to select the converted-data polarity and to achieve a digital-like transfer function.

Table of Contents

1	Introduction	1
1.1	Motivation: All-Optical Processing in Optical Communication Networks	1
1.2	Historical Review of Research in Resonant-Type Semiconductor Optical Amplifiers	3
1.2.1	Fabry–Perot Amplifiers	4
1.2.2	Distributed Feedback Amplifiers	6
1.3	Overview of Thesis	10
1.3.1	Principle of All-Optical Processing	10
1.3.2	Outline	11
2	Theoretical Foundation	15
2.1	Introduction	15
2.2	Coupled-Mode Equations	16
2.3	Carrier-Density Rate Equation	27

2.4	Small-Signal, Steady-State Solution	29
2.5	Transfer-Matrix Formulation	31
2.6	Bragg Resonances	32
2.7	Conclusion	36
3	Optical Bistability: Steady-State Analysis	38
3.1	Introduction	38
3.2	Physical Process of Bistability	38
3.3	Transfer-Matrix Analysis	40
3.4	Spectral Range and Uniformity	42
3.5	Reflective Bistability	45
3.6	Conclusion	49
4	Nonuniform Gratings	51
4.1	Introduction	51
4.2	Transfer-Matrix Analysis	52
4.2.1	Grating Nonuniformities	52
4.2.2	Small-Signal Amplification	55
4.2.3	Nonlinear Response	57
4.3	Chirped-Grating DFB SOAs	61
4.3.1	Spectral Range	61
4.3.2	Spectral Uniformity	64

4.3.3	Reflective Bistability	66
4.3.4	Large Amounts of Chirp	70
4.4	Conclusion	72
5	Optical Bistability: Time-Dependent Analysis	75
5.1	Introduction	75
5.2	Time-Dependent Model	75
5.3	Hysteresis	80
5.4	Conclusion	83
6	All-Optical Flip–Flop	84
6.1	Introduction	84
6.2	Principle of Operation	86
6.2.1	Control using Holding Beam	86
6.2.2	Control using Auxiliary Signals	90
6.3	Experimental Demonstration	101
6.3.1	Experimental System	101
6.3.2	Set–Reset Operation	106
6.4	Performance	107
6.4.1	Wavelength Range and Power	107
6.4.2	Direction and Polarization	109
6.4.3	Set-Pulse Power	110

6.4.4	Relative Strength of Control Signals	112
6.4.5	Speed	113
6.4.6	Back-to-Back ‘Set’ Signals	116
6.5	Applications	118
6.6	Conclusion	120
7	Data-Wavelength Conversion	123
7.1	Introduction	123
7.2	Experimental System	124
7.3	1306-to-1547 nm Conversion	125
7.3.1	Polarity Selection	126
7.3.2	Wavelength Range of Data Signals	127
7.3.3	Linear and Nonlinear Transfer Functions	129
7.3.4	Data and Probe Signals	129
7.3.5	Dependence on Data Rate	131
7.4	Conversion within the 1550-nm Spectral Window	132
7.5	Comparison with Related Research	132
7.5.1	1310-to-1550 nm Wavelength Converters	132
7.5.2	Interferometric-based Wavelength Converters	134
7.5.3	All-Optical Flip–Flop	134
7.6	Conclusion	135

8	Concluding Remarks	137
8.1	Overview	137
8.2	Spectral Range of Bistability	137
8.3	Shape of Bistable Hysteresis Curves	138
8.4	All-Optical Flip–Flop	139
8.5	Data-Wavelength Conversion	142
8.6	Summary of Contributions	144
	Bibliography	146
A	DFB SOA used in Experiments	155
B	Mounting Procedure	157

List of Tables

2.1	Parameter values used in simulations.	33
6.1	Parameter values for flip–flop control via holding beam.	89
6.2	Parameter values for flip–flop control via control signals.	99

List of Figures

1.1	Schematic of a distributed feedback semiconductor optical amplifier.	7
1.2	Bragg resonance structure of a DFB SOA.	11
2.1	Evolution of the small-signal transmittivity spectrum with change in gain.	34
2.2	Evolution of the small-signal reflectivity spectrum with change in gain.	35
3.1	Bistable hystereses for two signal wavelengths.	39
3.2	Spectral range of bistable switching.	43
3.3	Hysteresis curves spanning 12.5 GHz for a uniform-grating DFB SOA.	44
3.4	Variety of reflected-power hysteresis curves: short-wavelength side of photonic bandgap.	45
3.5	Variety of reflected-power hysteresis curves: long-wavelength side of photonic bandgap.	48
4.1	DFB SOA with a linearly chirped grating.	54

4.2	Effect of α on the small-signal transmittivity of a $\lambda/4$ -shifted DFB device.	55
4.3	Small-signal transmittivity of a $\lambda/4$ -shifted DFB SOA with spatial chirp.	57
4.4	Internal power of a $\lambda/4$ -shifted DFB SOA with and without spatial chirp.	58
4.5	Spectral evolution of the bistable hysteresis for a $\lambda/4$ -shifted DFB SOA with and without spatial chirp.	59
4.6	Gain tuning of the bistable hysteresis curve.	61
4.7	Small-signal transmittivity spectra for chirped-grating DFB SOAs. .	62
4.8	Improved spectral range of bistable switching.	63
4.9	Chirp-improved spectral uniformity of hysteresis curve.	65
4.10	Sub- μ W switching thresholds.	66
4.11	Bistable output over a 12.5-GHz spectral range for the P-direction. .	66
4.12	Small-signal reflectivity spectra for a linearly chirped DFB SOA. . .	67
4.13	Persistence of S-shaped hysteresis curve on reflection.	68
4.14	Low-threshold, loop-shaped hysteresis curves on reflection.	70
4.15	High-contrast hysteresis curve on reflection.	71
4.16	Double bistability.	72
4.17	Strong secondary Bragg resonances.	72
5.1	Bistable hysteresis curve using time-dependent model.	80

5.2	Comparison of time-dependent and steady-state models.	81
5.3	Modulation-period dependence of the hysteresis curve.	83
6.1	Schematic of all-optical flip–flop.	85
6.2	Flip–flop output states.	87
6.3	Flip–flop operation via holding-beam control.	88
6.4	Hysteresis curve during flip–flop operation via holding-beam control.	90
6.5	XPM-based optical set.	92
6.6	XPM-based optical reset.	93
6.7	Flip–flop operation via auxiliary optical signals.	100
6.8	Experimental system for all-optical flip–flop demonstration.	101
6.9	Reset-signal spectra.	103
6.10	All-optical flip–flop operation.	106
6.11	Broad spectral range of set signals.	108
6.12	Flip–flop operation using (b) 1537-nm set and 1306-nm reset signals, and (c) 1567-nm set and 1466-nm reset signals.	109
6.13	Set-pulse ledge.	111
6.14	Flip–flop operation at the high-speed limit of experimental system.	114
6.15	Flip–flop operation using a short set pulse.	115
6.16	Back-to-back set signals: experiment.	117
6.17	Back-to-back set signals: simulation.	118
6.18	High-speed RZ to low-speed NRZ conversion.	120

7.1	Experimental system for data-wavelength conversion.	125
7.2	1306-to-1547 nm data-wavelength conversion.	126
7.3	Polarity inversion of converted data.	127
7.4	1466-to-1547 nm data-wavelength conversion.	128
7.5	Digital-like transfer function.	130
7.6	Patterning effects at 900 Mb/s for RZ and NRZ signals with a ‘10110100’ data sequence.	131
7.7	1560-to-1547 nm data-wavelength conversion.	133
A.1	ASE spectrum of the DFB SOA used in experiments.	156

Chapter 1

Introduction

1.1 Motivation: All-Optical Processing in Optical Communication Networks

Optical communication systems have ushered in an information age of unparalleled capacity and growth. In such systems, data is represented by optical pulses and is sent along low-loss silica fiber. Optical signals currently carry about 6.5 petabits (10^{15} bits) per day over global public networks [1]; the majority of this data is for internet services such as graphics, video, music, and text, whereas the more traditional voice data is already a minority [2]. Demand for internet services will continue to fuel the growth in the capacity of fiber-optic communication systems. The capacity over public networks is expected to grow to between 64 and 160 petabits per day within the next two years (2001–2002) [1].

The successful delivery of information through such networks requires the optical signals to be manipulated or *processed* in some way; processing applications include amplification, regeneration, retiming, multiplexing and demultiplexing, reshaping, and routing. Commonly, data is processed by being converted from optical to elec-

trical signals, electronically processed, and then converted back to optical signals for transmission [2] (i.e., data is converted from the optical layer to the electrical layer and then back to the optical layer).

Electronic processing techniques, however, may not continue to be cost effective when they are scaled up to accommodate the growth in network capacity. In the mid-1990s, the technique of wavelength-division multiplexing (WDM), in which the capacity of a single fiber is increased \mathcal{N} times by simultaneously using \mathcal{N} different signal wavelengths [3], began to be implemented in fiber-optic communications systems. Using electronic regeneration for signals within WDM systems, however, would require demultiplexing the wavelength channels, detecting and electronically regenerating each individual channel, and then multiplexing all wavelength channels back together again; electronic processing would therefore be costly in high-capacity systems with large channel count \mathcal{N} [4]. WDM systems became affordable, in part, by the use of erbium-doped fiber amplifiers (EDFAs) to amplify data signals *at the optical layer* [5], without electronic conversion.

Optical-processing techniques will continue to be implemented in optical networks as long as they meet a capacity demand at a lower cost than electronic means [2]. An example of a promising application for optical processing is data-wavelength conversion, where data is transferred from one signal wavelength to another (see Chapter 7 for a discussion on the utility of data-wavelength conversion in WDM systems). Although data-wavelength conversion in the electrical domain is economical at present-day data rates of 10 gigabits/second (Gb/s) and slower, it is expected to be prohibitively more expensive at faster data rates [4]. All-optical techniques (in which only optical signals are used) have been used to demonstrate data-wavelength con-

version at speeds as fast as 100 Gb/s while using relatively inexpensive components [6].

This thesis explores the nonlinear response and all-optical signal-processing capabilities of distributed feedback (DFB) semiconductor optical amplifiers (SOAs), and seeks to advance their application to optical communication networks. A history of research on DFB SOAs is presented in the following section.

1.2 Historical Review of Research in

Resonant-Type Semiconductor Optical Amplifiers

Semiconductor optical amplifiers (SOAs) possess many characteristics that make them well suited for all-optical signal-processing applications. Gain saturation is accompanied by a significant change in the refractive index; this carrier-induced nonlinear refractive index has been estimated to have an effective Kerr nonlinearity $n_2 \sim 10^{-9} \text{ cm}^2/\text{W}$ [7], seven orders of magnitude greater than the value of n_2 in silica fiber. SOAs also have the advantages of being compact ($< 500 \text{ } \mu\text{m}^3$ active volume), integrateable with other devices, and operable at any wavelength used in fiber-optic communication systems [8]. Furthermore, since SOAs provide amplification (with modal gain $\sim 300 \text{ cm}^{-1}$, four orders of magnitude larger than that of erbium-doped silica), they allow high fan-out and high cascadability, which are general requirements for large photonic circuits and multi-component lightwave systems [9].

1.2.1 Fabry–Perot Amplifiers

In the 1980s, researchers began exploring the nonlinear response of SOAs within Fabry–Perot cavities. Such devices were readily available — they are just Fabry–Perot diode lasers driven below lasing threshold. In 1982, Otsuka and Iwamura of NTT presented a theoretical analysis of optical bistability in Fabry–Perot SOAs [10], and showed that the bistable-switching thresholds decrease as the strength of the nonlinearity increases, and as the detuning of the probe signal from the resonance decreases. Within a year, optical bistability was experimentally demonstrated in a GaAs semiconductor operating at $0.8\ \mu\text{m}$ by groups at the University of Tokyo [11] and NTT [12].

In 1985, research groups from British Telecom Research Laboratories (Adams, Collins, Henning, O’Mahony, Westlake, and Wyatt) and GTE Laboratories (Sharfin and Dagenais) reported new theoretical and experimental findings, and contributed over 15 journal papers on bistable Fabry–Perot SOAs by the end of 1987. Researchers have investigated basic bistable behavior (e.g., switching and hysteresis) [11], [13]–[21], multistability [22], and differential gain [11], [23], as well as applications for optical communications and computing, such as data-wavelength conversion [24]–[26], wavelength-division demultiplexing [27], [28], optical limiting [17], [23], signal regeneration [26], logic gates [9], [17], neural-network processing [29], and memory [23], [30]. Bistability was demonstrated in InGaAsP/InP amplifiers at 1310 nm [31], and at 1550 nm [14], as well as in bulk [11], strained quantum well [32], and multi-quantum well [33] active regions.

Bistable switching was found to occur at optical powers three orders of magnitude

smaller than those of bistable passive semiconductors (which operate via the Kerr nonlinearity) [34], at switching powers $\sim 1 \mu\text{W}$ [14], [31]. Thus, these devices easily operate at power levels available in fiber-optic communication systems. The largest reported on–off ratio for the switched signal has been 5:1 [35], and the largest optical gain through the Fabry-Perot SOAs has been 20 dB [23].

Rise and fall times of the switched output power have been measured to be as small as 0.5 ns [35], which are on the order of the carrier lifetime $\tau \sim 1$ ns. Rise and fall times were predicted to occur *faster* than the carrier lifetime for high-finesse cavities driven near 98% of lasing threshold [36]. Nonetheless, the repeatability of the bistable system is ultimately limited by the carrier lifetime τ ; for example, slow repeatability manifested as a substantial closing down of the bistable hysteresis curve even for an input signal having a 4-ns sinusoidal modulation period [37]. Repeatability is limited because, for example, although the initial fall time may a fraction of the carrier lifetime, switch–off is followed by a relatively slow recovery to the initial carrier density [35]. Moreover, the repeatability of the bistable system can also be limited by a switch–on delay (from the moment of pulse impact) [38]; attributed as “critical slowing down,” this delay is on the order of the carrier lifetime, but can be decreased below τ by choosing a high input optical power, or a small spectral detuning between the optical signal and the Fabry–Perot resonance [23].

Since typical switching times and powers are ~ 1 ns and $\sim 1 \mu\text{W}$, respectively, femtojoule switching energies are expected. The lowest energy reported thus far has been 500 attojoules ($0.5 \text{ ns} \times 1 \mu\text{W}$) [35], which corresponds to about 3000 photons for a signal wavelength of 1310 nm [27]. Fabry–Perot SOAs also exhibit a high

optical switching energy per gain (~ 100 fJ), and a large switching energy per unit surface area (~ 1 fJ / μm^2 [27]).

Although the optical energy for switching is low, a substantial amount of energy is still needed to operate the SOA. Namely, an electrical bias is required to maintain the device near lasing threshold [39]. For an injection current of 10 mA, a semiconductor bandgap energy of 1 eV, and a carrier lifetime of 1 ns, the required electrical energy is 10 pJ. This energy must be dissipated as heat, and this dissipation limits the number density of devices that can be placed within a given area of a single substrate. For a power consumption of 10 mW per SOA, and assuming a practical heat-sink power density of 1 W / cm^2 [39], each SOA requires a minimum area of 0.01 cm^2 . This results in a maximum number density of 100 / cm^2 . Thus, Fabry–Perot SOAs are limited to signal-processing applications requiring a small number of devices, and hence to low functionality [40].

Bistable switching in Fabry–Perot SOAs also exhibits a limited spectral range [39], [40]. This limited wavelength range has been quantified for devices biased near 98% of lasing threshold; upward switching below 0.1 mW was found to span a spectral range of less than 0.02 nm [20]. While some applications can make use of the narrow spectral response (e.g., wavelength-division demultiplexing [28]), this sensitivity to operating wavelength generally limits the application of such devices [17], [40].

1.2.2 Distributed Feedback Amplifiers

The all-optical signal-processing applications discussed in the previous section on Fabry–Perot amplifiers can also be achieved using other kinds of “resonant-type”

SOAs. In contrast to the “lumped” feedback occurring at each end of a Fabry–Perot cavity, feedback can be “distributed” along the SOA by using a built-in diffraction grating, as shown in Fig. 1.1. The resulting *distributed feedback* SOA exhibits Bragg resonances, as opposed to Fabry–Perot resonances. Dispersive optical bistability in nonlinear distributed feedback structures was first predicted in 1979 by Winful, Marburger, and Garmire for a device utilizing the Kerr nonlinearity [41]. In 1985, bistability was demonstrated using a DFB SOA, utilizing the strong carrier-induced nonlinearity of active semiconductors [42].

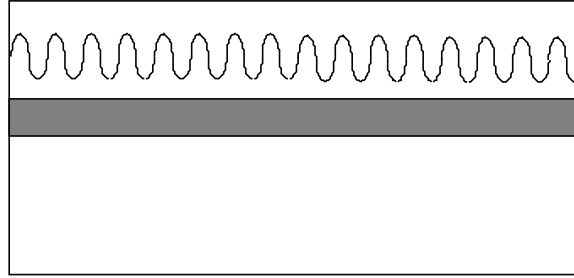


Figure 1.1: Schematic of a distributed feedback semiconductor optical amplifier. The grating is typically fabricated outside of the gain region (shaded grey).

From 1986–1987, researchers presented a time-dependent model for bistability in DFB SOAs, simulated bistable switching (including the switch-on delay), discovered a difference in the shape of the hysteresis curve for bistability at either side of the photonic bandgap [43], predicted a variety of shapes of the hysteresis curve on reflection [17], experimentally demonstrated an upward-switching power of $1 \mu\text{W}$ [43], and showed a relatively large on–off contrast ratio of 10:1 [44]. Further investigations demonstrated how a spike during upward switching dominates the output-pulse shape as the signal wavelength is detuned away from the Bragg resonance [45], and showed how a non-zero reflectivity at the SOA facets enhances bistable switching at one edge

of the photonic bandgap [46]. Optical bistability was also observed in studies of resonant amplification using uniform [47] and $\lambda/4$ -shifted [48] gratings. In addition, although largely unexplored, the same issues discussed above for Fabry–Perot devices also apply to DFB SOAs, and the same conclusions can be drawn regarding the switching speed and repeatability, switching energy, number density, and wavelength range of operation.

The relatively low number of investigations into the nonlinear response of DFB SOAs compared with Fabry–Perot SOAs is perhaps because of the availability of the latter during the mid-1980s. Fabry–Perot devices are easy to fabricate; cavities are formed simply by cleaving the semiconductor, and the semiconductor material is grown without stopping to create the feedback structure (i.e., facets). DFB SOAs require a more complicated fabrication procedure; Bragg gratings are created using techniques such as interferometric exposure or electron-beam lithography [49], and the growth of the semiconductor material is typically arrested during grating formation.

Despite these difficulties in fabrication, DFB SOAs have distinct advantages. Bragg gratings can be incorporated directly into a larger waveguide structure, allowing integration onto a single substrate with other photonic gates [43]. In addition, gratings also have more features that can be re-designed in pursuit of improved performance; such features include the grating’s shape (e.g., period and depth [50]) and composition (e.g., modulation of the refractive index, gain, loss, or any combination thereof [51]). These changes would come, however, at the probable expense of increasing the difficulty of fabrication.

These two kinds of resonant-type SOAs also differ in the number of strong res-

onances occurring within the SOA gain curve; Bragg gratings provide only a few strong modes, whereas Fabry-Perot cavities generally supports many. (The relatively small number of modes was the main reason for the development of DFB SOAs, more commonly used above threshold as DFB lasers.) This inherent spectral filtering property of DFB SOAs reduces the background noise, which appears as a DC offset and lowers the on-off switching ratio [9]. Also, since Fabry-Perot cavities have many modes, the strongest modes are determined by the gain curve and lie at the gain peak. The wavelengths of the dominant resonances of DFB SOAs, however, can be fabricated to occur anywhere in the SOA gain spectrum. This is advantageous since the strength of the carrier-induced nonlinearity varies along the gain curve; DFB SOAs thus allow a tunable strength of the nonlinearity.

In summary, nonlinear optical processing in resonant-type SOAs has the following advantages:

- low optical power and energy
- amplification
- availability
- wavelength compatibility with fiber-optic communications
- integrateability (for DFB SOAs)

While these advantages motivate us to use DFB SOAs for all-optical processing, the following limitations must be considered:

- wavelength range of operation

- speed
- number density

Advancing the application of DFB SOAs to fiber-optic communication systems by addressing these limitations is a major undercurrent of this thesis.

1.3 Overview of Thesis

1.3.1 Principle of All-Optical Processing

The two key ingredients used for nonlinear optical processing in DFB SOAs are symbolized by the right-hand side of the equation for the Bragg wavelength [52]

$$\lambda_B = 2\Lambda n. \quad (1.1)$$

Here, the Bragg wavelength λ_B of a first-order grating is proportional to the grating period Λ and the refractive index n . The grating period Λ symbolizes the existence of *Bragg resonances*, a key ingredient that provides resonant optical amplification, as shown in Fig. 1.2. The refractive index n is nonlinear, and symbolizes *the potential for optical signals to shift the spectral location of the Bragg resonances*. Both of these key ingredients are coupled to the SOA gain; changes in gain will change the strength of a Bragg resonance *and* shift its spectral location. Thinking in terms of the Bragg resonance and its signal-induced spectral shift is insightful, and we will use these concepts throughout the thesis.

This thesis explores the nonlinear response exhibited by DFB SOAs, and seeks to

advance their application to optical communication systems and networks. Much of our work focuses on overcoming the limited wavelength range of operation of such devices; we attack this issue by investigating new aspects of each key ingredient. Namely, we vary the Bragg period Λ along the length of the DFB SOA to increase the spectral range of the bistable signal. And, we demonstrate how to increase *or* decrease the refractive index n via auxiliary optical signals; this allows the bistable state of optical memory to be controlled over a very wide wavelength range.

1.3.2 Outline

Chapter 2 builds the foundation of our theoretical analyses. We derive coupled-mode equations for the optical signal that interacts with the Bragg grating, and derive a rate equation for the SOA gain. A small-signal, steady-state solution is also presented; although the optical processing of interest is nonlinear and time-dependent, this simple solution provides physical insight into nonlinear behavior, and is used later in computing nonlinear solutions. After formulating the small-signal solution as a transfer

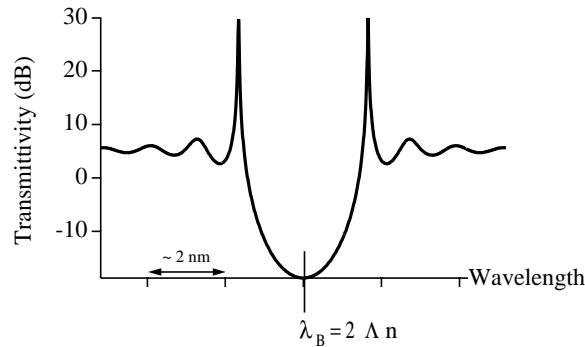


Figure 1.2: Bragg resonance structure of a DFB SOA, centered about the Bragg wavelength (for a uniform grating without facet reflections).

matrix, we show how the strength and spectral location of the Bragg resonances depend on gain.

Chapter 3 begins our investigation of optical bistability, a phenomenon in which an optical signal processes itself. We discuss the physical mechanism of bistability, and develop a transfer-matrix method to calculate the steady-state bistable behavior. With this model, we account for the intensity distribution along the DFB SOA, and study the spectral range, spectral uniformity, and shape of the hysteresis curve on transmission and reflection. The steady-state solutions help to introduce physical concepts used throughout the thesis, and to quantify the spectral limitations of bistability.

Chapter 4 explores the effects of nonuniform gratings on optical bistability in DFB SOAs, with an emphasis on increasing the spectral range of the bistable signal. We begin by discussing generalizations to the transfer-matrix method that incorporate grating nonuniformities. We then study how varying the grating pitch Λ along the device (i.e., spatial chirp) increases the spectral range of bistability, while simultaneously altering the switching powers, spectral uniformity, and shape of the hysteresis curve.

Chapter 5 begins our time-dependent analysis of optical bistability. We develop a simple model for the bistable system based on the governing equations presented in Chapter 2. Predictions from the time-dependent model are compared to those from the steady-state model of Chapter 3, and the time-dependent hysteresis curve is shown to warp as the modulation frequency of the input signal is increased. The model developed here serves as the basis for simulating all-optical processing in the following chapter.

Chapter 6 presents an experimental and numerical study of all-optical flip-flop operation, a processing technique based upon optical bistability. In the first section, we discuss novel control techniques that use auxiliary optical signals to set and reset the bistable output state, and we extend the model presented in Chapter 5 to simulate flip-flop operation. The new control techniques use cross-phase modulation (XPM) to shift the spectral location of the Bragg resonance relative to the bistable signal, thereby shifting the hysteresis curve relative to the bistable signal's input power. In the second section, we present our experimental system, discuss its operation and limitations, and demonstrate basic flip-flop operation using the new control techniques. In the third section, we investigate the flip-flop's performance, addressing issues such as speed, power, polarization, and response to back-to-back set pulses. We end this chapter with an application of the flip-flop to high-speed optical communication systems — conversion of high-speed return-to-zero (RZ) signals to low-speed non-return-to-zero (NRZ) signals. This application overcomes the three limitations summarized at the end of Section 1.2.2.

Chapter 7 investigates data-wavelength conversion, where an input data-signal shifts a Bragg resonance onto or off of another signal via XPM. This process may be assisted by bistable switching, although memory does not occur. We focus our study on 1310-to-1550 nm conversion, discussing the principle of operation, performance, and features such as selecting the converted-data polarity and achieving a digital-like transfer function. Then, we demonstrate wavelength conversion between signals within the 1550-nm spectral window, and compare our research with other all-optical techniques.

Chapter 8 summarizes the main findings and conclusions of the thesis, and discusses possible avenues for future research.

Chapter 2

Theoretical Foundation

2.1 Introduction

In this thesis, we study the nonlinear behavior of an optical signal interacting with a Bragg grating and the carrier density of a DFB SOA. In this chapter, we present equations that govern this interaction: namely, a rate equation incorporating the effect of the signal on the carrier density, and coupled-mode equations describing the effect of the grating on the signal. The latter are derived from first principles from Maxwell's equations. We present a simple solution to this set of equations, and use it to formulate a transfer matrix. The transfer matrix is then used to show how the Bragg resonances depend on the small-signal gain.

2.2 Coupled-Mode Equations

We begin our analysis of the propagation of an optical signal through a DFB SOA with Maxwell's equations. In the MKS system of units, these are [53]

$$\vec{\nabla} \times \vec{\mathcal{E}} = -\frac{\partial \vec{\mathcal{B}}}{\partial t}, \quad (2.1)$$

$$\vec{\nabla} \times \vec{\mathcal{H}} = \vec{\mathcal{J}} + \frac{\partial \vec{\mathcal{D}}}{\partial t}, \quad (2.2)$$

$$\vec{\nabla} \cdot \vec{\mathcal{D}} = \rho, \quad (2.3)$$

$$\vec{\nabla} \cdot \vec{\mathcal{B}} = 0, \quad (2.4)$$

where $\vec{\mathcal{J}}$ is the current density, ρ is the charge density, $\vec{\mathcal{E}}$ is the electric field, $\vec{\mathcal{H}}$ is the magnetic field, $\vec{\mathcal{D}}$ is the electric-flux density, and $\vec{\mathcal{B}}$ is the magnetic-flux density. The current and charge densities are sources of the electric field, and the flux densities arise within the SOA in response to the electric and magnetic fields. For non-magnetic media, such as the SOA, the flux and current densities can be written in terms of the fields using the following constitutive relations [53]:

$$\vec{\mathcal{D}} = \epsilon_0 \vec{\mathcal{E}} + \vec{\mathcal{P}}, \quad (2.5)$$

$$\vec{\mathcal{B}} = \mu_0 \vec{\mathcal{H}}, \quad (2.6)$$

$$\vec{\mathcal{J}} = \sigma \vec{\mathcal{E}}, \quad (2.7)$$

where ϵ_0 and μ_0 are the vacuum permittivity and permeability, respectively, σ is the conductivity, and $\vec{\mathcal{P}}$ is the induced electric polarization.

A wave equation governing the propagation of optical fields can be derived as

follows. Taking the curl of Eq. (2.1) and applying Eq. (2.6) yields

$$\vec{\nabla} \times \vec{\nabla} \times \vec{\mathcal{E}} = -\mu_0 \frac{\partial}{\partial t} (\vec{\nabla} \times \vec{\mathcal{H}}). \quad (2.8)$$

This can be written entirely in terms of the electric field $\vec{\mathcal{E}}$ and electric polarization $\vec{\mathcal{P}}$ using Eqs. (2.2), (2.5), and (2.7). Restricting our attention to source-free regions of space, thereby neglecting free charges ($\rho = 0$) and free currents ($\vec{\mathcal{J}} = 0$), and using a common vector identity [53], the wave equation becomes

$$-\vec{\nabla}^2 \vec{\mathcal{E}} + \vec{\nabla} (\vec{\nabla} \cdot \vec{\mathcal{E}}) = -\frac{1}{c^2} \frac{\partial^2 \vec{\mathcal{E}}}{\partial t^2} - \frac{1}{\epsilon_0 c^2} \frac{\partial^2 \vec{\mathcal{P}}}{\partial t^2}, \quad (2.9)$$

where c is the speed of light in vacuum and satisfies $c^2 = 1/(\epsilon_0 \mu_0)$. We further simplify the wave equation using Eqs. (2.3) and (2.5), and knowing that the resulting polarization source term $\vec{\nabla} \cdot \vec{\mathcal{P}}$ is negligible in most cases of practical interest [55]; the electric field $\vec{\mathcal{E}}$ thus satisfies the following standard wave equation, driven by the second time derivative of the induced electric polarization:

$$\vec{\nabla}^2 \vec{\mathcal{E}} - \frac{1}{c^2} \frac{\partial^2 \vec{\mathcal{E}}}{\partial t^2} = \frac{1}{\epsilon_0 c^2} \frac{\partial^2 \vec{\mathcal{P}}}{\partial t^2}. \quad (2.10)$$

We prefer to manipulate the wave equation in the frequency domain. Taking the Fourier transform of the wave equation (2.10), we obtain

$$\vec{\nabla}^2 \vec{E}(x, y, z, \omega) + \frac{\omega^2}{c^2} \vec{E}(x, y, z, \omega) = -\frac{\omega^2}{\epsilon_0 c^2} \vec{P}(x, y, z, \omega), \quad (2.11)$$

where

$$\vec{E}(x, y, z, \omega) = \int_{-\infty}^{\infty} \vec{\mathcal{E}}(x, y, z, t) e^{i\omega t} dt, \quad (2.12)$$

$$\vec{P}(x, y, z, \omega) = \int_{-\infty}^{\infty} \vec{\mathcal{P}}(x, y, z, t) e^{i\omega t} dt. \quad (2.13)$$

The response of the medium to the electric field is governed by

$$\vec{P}(\omega) = \epsilon_0 \chi(\omega) \vec{E}(\omega), \quad (2.14)$$

where we assume that the medium is isotropic so that the susceptibility χ is scalar [55].

Using the medium-response equation (2.14), the frequency-domain wave equation is given by

$$\vec{\nabla}^2 \vec{E}(\omega) + \frac{\omega^2}{c^2} \epsilon(\omega) \vec{E}(\omega) = 0, \quad (2.15)$$

where the complex dielectric function $\epsilon(\omega)$ is given by

$$\epsilon(\omega) = 1 + \chi(\omega). \quad (2.16)$$

Equation (2.15) is the Helmholtz equation, and is valid for nonlinear media and arbitrary electric fields.

For fields passing through a SOA, it is convenient to write the dielectric function as $\epsilon = \epsilon_b + \epsilon_a$, in terms of background ϵ_b and active-region ϵ_a contributions [55], each of which can be complex valued. In our *distributed feedback* SOA, a built-in grating

runs parallel to, but outside of, the gain region, where it intersects the transverse mode of the optical field. The grating is quantified by its period Λ , or similarly by its spatial frequency $\beta_B = \pi/\Lambda$, commonly called the Bragg wavenumber. We account for the grating in the Helmholtz equation by writing the background dielectric function ϵ_b as $\epsilon_b = \bar{\epsilon}_b + \Delta\epsilon_b$, where $\bar{\epsilon}_b$ is constant in along z , and the spatially varying portion $\Delta\epsilon_b$ is represented by the following Fourier series:

$$\Delta\epsilon_b(x, y, z) = \sum_{p \neq 0} c_p(x, y) \exp(ip \frac{2\pi z}{\Lambda}) = \sum_{p \neq 0} c_p(x, y) \exp(ip 2\beta_B z). \quad (2.17)$$

We consider a modulation in only the *real* part of the dielectric function, thus yielding a so-called “index-coupled” grating.

The optical field that interacts with the Bragg grating is represented by

$$\vec{\mathcal{E}}(x, y, z, t) = 2\text{Re}\{\vec{\mathcal{V}}(x, y, z, t)\} = \vec{\mathcal{V}} + \vec{\mathcal{V}}^*, \quad (2.18)$$

where $\text{Re}\{\}$ represents the real part and $\vec{\mathcal{V}}$ is the analytic-signal representation of the electric field [56]. The analytic signal is expressed as

$$\vec{\mathcal{V}}(x, y, z, t) = \hat{u} F(x, y) \mathcal{U}(z, t) \exp(-i\omega_0 t), \quad (2.19)$$

$$\mathcal{U}(z, t) = \mathcal{E}_f(z, t) \exp(i\beta z) + \mathcal{E}_b(z, t) \exp(-i\beta z), \quad (2.20)$$

where \hat{u} is the unit vector along the transverse-electric (TE) orientation of polarization, $F(x, y)$ is the transverse distribution of the fundamental mode supported by the waveguide, $\mathcal{U}(z, t)$ is the slowly varying longitudinal field distribution, $\beta = n\omega_0/c = n\beta_0$ is the modal wavenumber, n is the modal refractive index, and ω_0 is the central

angular frequency of the optical field. In the longitudinal direction, the field scatters off of the Bragg grating and is therefore conveniently decomposed into a forward \mathcal{E}_f and backward \mathcal{E}_b propagating field. The optical field is described in the frequency domain by applying a Fourier transform:

$$\vec{E}(x, y, z, \omega) = \int_{-\infty}^{\infty} dt \vec{\mathcal{E}}(x, y, z, t) e^{i\omega t}, \quad (2.21)$$

$$= \int_{-\infty}^{\infty} dt \hat{u} F(x, y) \mathcal{U}(z, t) \exp[i(\omega - \omega_0)t] + \text{c.c.}, \quad (2.22)$$

$$= \hat{u} F(x, y) U(z, \omega - \omega_0) + \hat{u} F^*(x, y) U^*(z, \omega + \omega_0), \quad (2.23)$$

where

$$U(z, \omega - \omega_0) = \int_{-\infty}^{\infty} dt \mathcal{U}(z, t) \exp[i(\omega - \omega_0)t]. \quad (2.24)$$

We drop the final term of Eq. (2.23) [57]; this term corresponds to $\vec{\mathcal{V}}^*$ whereas the analytic signal $\vec{\mathcal{V}}$ alone is sufficient to describe the optical field. From a physical standpoint, we neglect the final term by assuming that the medium does not respond at rates on the order of the optical frequency. The electric field in the frequency domain is then given by

$$\vec{E}(\omega) = \hat{u} F(x, y) [E_f(z, \omega - \omega_0) \exp(+i\beta z) + E_b(z, \omega - \omega_0) \exp(-i\beta z)]. \quad (2.25)$$

Inserting the optical-field expression (2.25) into the Helmholtz equation (2.15) yields equations for the transverse and longitudinal fields. The transverse field

$F(x, y)$ is governed by

$$\frac{\partial^2 F}{\partial x^2} + \frac{\partial^2 F}{\partial y^2} + [\bar{\epsilon}(x, y)\beta_0^2 - \beta^2]F = 0. \quad (2.26)$$

This equation provides the transverse-field profile F as well as the modal refractive index n [55], and it is assumed that F is not affected by the grating perturbation $\Delta\epsilon$.

The longitudinal field is governed by

$$\begin{aligned} \frac{dE_f}{dz} \exp(i\beta z) - \frac{dE_b}{dz} \exp(-i\beta z) &= \frac{i\beta_0^2}{2\beta V} \int \int dx dy \Delta\epsilon |F|^2 \\ &\times [E_f \exp(i\beta z) + E_b \exp(-i\beta z)], \end{aligned} \quad (2.27)$$

where the right-hand side is normalized by $V = \int \int dx dy |F|^2$, all integrations are performed over the grating region, and the second-order derivatives have been dropped since E_f and E_b are assumed to vary slowly. We replace $\Delta\epsilon$ by the Fourier series given by (2.17), and separate the result into two equations in the rotating frames $\exp(+i\beta z)$ and $\exp(-i\beta z)$:

$$\frac{dE_f}{dz} = i\kappa E_b \exp[-2i(\beta - \beta_B)z], \quad (2.28)$$

$$-\frac{dE_b}{dz} = i\kappa E_f \exp[2i(\beta - \beta_B)z], \quad (2.29)$$

where we have kept only the most closely phase-matched terms. The forward- and backward-propagating fields are coupled by

$$\kappa = \frac{\beta_0^2}{2\beta V} \int \int dx dy |c_1(x, y)| |F|^2, \quad (2.30)$$

where we have note that c_1 and c_{-1}^* are equal since the modulation $\Delta\epsilon_b$ is real valued,

and where we set the phase offset ϕ_1 of the coefficient $c_1 = |c_1| \exp(i\phi_1)$ to zero. In this thesis, we assume that the coupling coefficient κ is real-valued, neglecting the small imaginary part of β [55]. We refer the reader to Ref. [54] for a more general form of the coupling coefficient that includes the effects of a gain grating.

Having defined the coupling coefficient κ and the transverse-field equation (2.26), we prefer to re-write the coupled-mode equations (2.28) and (2.29) in terms of the slowly varying field envelopes A and B , defined in the time domain with

$$\mathcal{U}(z, t) = \mathcal{E}_f(z, t) \exp(i\beta z) + \mathcal{E}_b(z, t) \exp(-i\beta z), \quad (2.31)$$

$$= A(z, t) \exp(i\beta_B z) + B(z, t) \exp(-i\beta_B z). \quad (2.32)$$

The corresponding frequency-domain field envelopes are determined in the same manner as Eq. (2.24). The frequency-domain, coupled-mode equations in terms of the field envelopes \tilde{A} and \tilde{B} are

$$\frac{d\tilde{A}(\omega - \omega_0)}{dz} = i[\beta - \beta_B]\tilde{A} + i\kappa\tilde{B}, \quad (2.33)$$

$$-\frac{d\tilde{B}(\omega - \omega_0)}{dz} = i[\beta - \beta_B]\tilde{B} + i\kappa\tilde{A}. \quad (2.34)$$

The modal wavenumber $\beta = n\beta_0$ contains many contributions particular to active semiconductor media. In particular, the refractive index in SOAs is dependent on the carrier density N . To make this apparent, we expand the modal refractive index $n = n_b + n_a$ into a background part n_b and a contribution from the SOA active region n_a . Both the real n'_a and imaginary n''_a parts of $n_a = n'_a + in''_a$ depend on the carrier density. A very important parameter for active semiconductor media is the ratio of

the change in the real part of the refractive index $\Delta n'_a$ to the change in the imaginary part of the refractive index $\Delta n''_a$ [58]:

$$\alpha = \frac{\Delta n'_a}{\Delta n''_a} = -2\beta_0 \frac{\Delta n_a}{\Delta g}, \quad (2.35)$$

where we have introduced the power gain $g = -2\beta_0 n''_a$. Expanding the gain $g = (dg/dN)[N - N_0]$ and the refractive index $n = n_0 + (dn/dN)[N - N(0)]$ as linear functions of the carrier density N , evaluated at transparency $N = N_0$, the ratio α becomes

$$\alpha = -2\beta_0 \frac{dn/dN}{dg/dN}. \quad (2.36)$$

In our simulations, we assume that α does not depend on the carrier density; this common approximation greatly simplifies the theoretical analysis of bistability [34], but possibly hides actual behavior since the carrier density can take on a range of values between transparency and lasing threshold during bistable switching.

The quantity α is commonly known as the linewidth enhancement factor, and represents the change in the real part of the refractive index for a given change in the imaginary part. In any medium, the real and imaginary parts are coupled, and the strength of this coupling can be calculated using the Kramers-Kronig relations. In active semiconductors, this coupling is very strong — gain saturation is accompanied by significant changes in the refractive index, and this is a nuisance for applications such as semiconductor lasers. However, for our research, α is the nonlinearity that is the basis for nonlinear processing.

Changes in the refractive index with carrier density are most often attributed to a carrier-induced shift of the gain edge, [59], anomalous dispersion, and gain compression. A change in carrier density also affects the refractive index through free-carrier absorption [60], but this effect is usually dominated by the gain-edge contribution [59]. The refractive index also depends on temperature, but we operate at speeds (> 10 MHz) where sluggish temperature effects average out.

Using the linewidth enhancement factor α , the wavenumber β for DFB SOAs can be written as

$$\beta = \beta_b - i\frac{g}{2}(1 - i\alpha) + i\frac{\alpha_{\text{int}}}{2}, \quad (2.37)$$

where $\beta_b = \beta_0 n_b$ is the background modal wavenumber, and a loss term α_{int} has been phenomenologically added to account for loss mechanisms such as free-carrier absorption and scattering [55]. Before returning to the time domain, we expand the background wavenumber β_b in a Taylor series about ω_0 :

$$\beta_b(\omega) = \beta_b + \frac{d\beta_b}{d\omega}(\omega - \omega_0) + \frac{1}{2} \frac{d^2\beta_b}{d\omega^2}(\omega - \omega_0)^2 + \dots \quad (2.38)$$

$$\simeq \beta_b + \frac{1}{v_g}(\omega - \omega_0), \quad (2.39)$$

where each derivative of the Taylor expansion is evaluated at $\omega = \omega_0$, $v_g = d\omega/d\beta_b$ is the group velocity, and high-order terms are neglected since they produce little change for pulses passing through the small length ($\sim 300 \mu\text{m}$) of the SOA [7].

Using Eqs. (2.37) and (2.38), the couple-mode equations in the frequency domain

are given by

$$\frac{d\tilde{A}(\omega - \omega_0)}{dz} = i[\beta_b - \beta_B + \frac{1}{v_g}(\omega - \omega_0) - i\frac{g}{2}(1 - i\alpha) + i\frac{\alpha_{\text{int}}}{2}]\tilde{A} + i\kappa\tilde{B}, \quad (2.40)$$

$$-\frac{d\tilde{B}(\omega - \omega_0)}{dz} = i[\beta_b - \beta_B + \frac{1}{v_g}(\omega - \omega_0) - i\frac{g}{2}(1 - i\alpha) + i\frac{\alpha_{\text{int}}}{2}]\tilde{B} + i\kappa\tilde{A}. \quad (2.41)$$

Spontaneous emission into the counter-propagating modes is neglected since it is assumed to be much weaker than the optical signal [34].

Taking the inverse Fourier transform $\mathcal{F}^{-1}(f)$ defined by

$$\mathcal{F}^{-1}[f(\omega - \omega_0)] = \frac{1}{2\pi} \int_{-\infty}^{\infty} d(\omega - \omega_0) f(\omega - \omega_0) \exp[-i(\omega - \omega_0)t], \quad (2.42)$$

the couple-mode equations in the time domain are

$$\frac{\partial A}{\partial z} + \frac{1}{v_g} \frac{\partial A}{\partial t} = i\Delta A + i\kappa B, \quad (2.43)$$

$$-\frac{\partial B}{\partial z} + \frac{1}{v_g} \frac{\partial B}{\partial t} = i\Delta B + i\kappa A, \quad (2.44)$$

where

$$\Delta = \delta - i\frac{g}{2}(1 - i\alpha) + i\frac{\alpha_{\text{int}}}{2}. \quad (2.45)$$

The detuning parameter δ is given by

$$\delta = \beta_b - \beta_B = \frac{2\pi n_b}{\lambda} - \frac{\pi}{\Lambda} = \frac{2\pi n_b}{\lambda} - \frac{2\pi n}{\lambda_B}, \quad (2.46)$$

where $\lambda = 2\pi c/\omega_0$ is the free-space optical wavelength, and $\lambda_B = 2n\Lambda$ is the Bragg

wavelength of a first-order grating. In taking the inverse Fourier transform, we recognize that the gain spectrum is much broader than that of the optical signal; the latter acts like a Dirac δ function and allows the convolution integral involving the two quantities to be easily performed. The gain term g in the time domain is thus evaluated at the optical-signal frequency ω_0 .

The detuning δ is related to the free-space signal wavelength λ such that, for constant n_0 and Λ , smaller values of detuning correspond to longer signal wavelengths. We have defined the detuning parameter δ to be *independent* of gain. This allows us to easily isolate the dependence on the small-signal gain g_o — i.e., changing g_o , while keeping δ constant, does not change the wavelength. Many previous studies defined a detuning parameter that is *dependent* on the small-signal gain g_o (e.g., [10], [17], [22], [34]); using these formulations to calculate, for example, the bistable hysteresis curve for different values of g_o , while fixing the value of δ , results in a different signal wavelength λ for each hysteresis curve, and yields qualitatively misleading results.

The gain g experienced by the optical modes is related to the carrier density N by [55]

$$g(x, y, z, t) = \Gamma g_{\text{mat}} = \Gamma a [N(x, y, z, t) - N_0], \quad (2.47)$$

where Γ is the optical confinement factor and represents the fraction of the transverse intensity distribution $|F(x, y)|^2$ that falls within the gain-region area Wd , and W and d are the width and thickness of the gain region, respectively. The material gain $g_{\text{mat}} = a(N - N_0)$ is assumed to be linear function of the carrier density N , with its slope $a = dg/dN$ (the differential gain) evaluated at transparency N_0 . The precise

wavelength dependence of the gain is suppressed because the gain is assumed to be flat over the spectral range of interest (~ 1 nm); also, we do not expect the wavelength dependence to significantly alter the optical-processing techniques modeled in this thesis.

To complete our theoretical foundation, we need to know how the carrier density responds to an optical signal.

2.3 Carrier-Density Rate Equation

The carrier density N is the density of electron-hole pairs, and is based on the assumption of charge neutrality between the conduction-band electrons and valence-band holes [55]. For time scales longer than the intraband relaxation time (~ 0.05 ps), the dynamics of the carrier density in both SOAs and semiconductor lasers has been successfully modeled by a rate equation [55]

$$-D\nabla^2 N + \frac{\partial N}{\partial t} = \frac{J}{ed} - \frac{N}{\tau} - a(N - N_0) \frac{I}{\hbar\omega}, \quad (2.48)$$

where D is the diffusion coefficient, and the right-hand side consists of various mechanisms that create or eliminate electron-hole pairs. The first term represents electrical injection of carriers, where J is the injected current density and e is the electric charge. The second term accounts for spontaneous and nonradiative recombination mechanisms, where τ is the carrier recombination lifetime. Although this lifetime is dependent on the carrier density (through spontaneous emission and Auger recombination) we neglect this dependence to simplify our analysis [61]. The final term

accounts for stimulated recombination of electron-hole pairs by the optical signal, where \hbar is Planck's constant h divided by 2π , and $I = \langle \vec{\mathcal{E}} \cdot \vec{\mathcal{E}} \rangle_t$ is the optical intensity, where $\langle \bullet \rangle_t$ indicates temporal averaging over many optical periods $2\pi/\omega$.

The carrier rate equation can be simplified considerably since the diffusion length ($\approx 2\mu\text{m}$) is longer than the gain-region thickness $d \sim 0.15\mu\text{m}$ and of the same order as the width $W \sim 2\mu\text{m}$ (for an index-guided device). Here, the diffusion length represents the distance traversed by a conduction-band electron before it recombines with a hole from the valence band. An average value of carrier density is therefore used in the transverse dimensions; averaging the rate equation (2.48) over the active-region area Wd yields

$$\frac{dN}{dt} = \frac{J}{ed} - \frac{N}{\tau} - \frac{a}{\hbar\omega}(N - N_0)\frac{\Gamma\sigma}{Wd}(|A|^2 + |B|^2), \quad (2.49)$$

where N is now understood to be averaged over the transverse dimensions, and the optical confinement factor Γ and the mode cross section σ are given by

$$\Gamma = \int_0^W \int_0^d dx dy |F(x, y)|^2 / \sigma, \quad (2.50)$$

$$\sigma = \int_{-\infty}^{\infty} \int_{-\infty}^{\infty} dx dy |F(x, y)|^2. \quad (2.51)$$

Carrier diffusion, which has been dropped from Eq. (2.49), is also assumed to smooth out the spatial holes burned by counterpropagating fields (with typical period $\approx 0.2\mu\text{m}$), allowing the interference terms of the intensity to be neglected. The car-

rier density is assumed to otherwise vary slow enough that the product $D \times \partial^2 N / \partial z^2$ is negligible.

Since the carrier density enters the coupled-mode equations through the modal gain g , it is convenient to formulate a gain rate equation using Eq. (2.49) and (2.47):

$$\tau \frac{dg}{dt} = g_0 - [1 + \bar{P}] g. \quad (2.52)$$

The quantity $g_0 = \Gamma a N_0 (\bar{J} - 1)$ is the small-signal value of g , and $\bar{J} = J\tau / edN_0$ is the current density normalized to its value required to achieve transparency. The normalized optical power \bar{P} is given by

$$\bar{P} = \frac{[|A(z)|^2 + |B(z)|^2]\sigma}{P_{\text{sat}}} = \frac{P_A + P_B}{P_{\text{sat}}}, \quad (2.53)$$

where $P_A = |A|^2 \sigma$ and $P_B = |B|^2 \sigma$ are the optical powers of the individual field envelopes, and $P_{\text{sat}} = \hbar \omega W d / (\tau a \Gamma)$ is the saturation power. The gain rate equation (2.52) also provides information on phase change experienced by the signal, since the carrier-density-dependent portion of the wavenumber is given by $\beta_N = -\alpha g / 2$. The gain rate equation (2.52) along with the coupled-mode equations (2.43) and (2.44) govern the nonlinear response of DFB SOAs.

2.4 Small-Signal, Steady-State Solution

In this section, we solve the gain rate equation (2.52) and coupled-modes equations (2.43) and (2.44) for the simple case of small powers ($P \ll P_{\text{sat}}$) and for input signals that vary much slower than the inverse of the carrier lifetime τ , such that a steady state

is achieved. In the steady-state, the governing equations become

$$g = g_0/(1 + \bar{P}), \quad (2.54)$$

$$\frac{dA}{dz} = i\Delta A + i\kappa B, \quad (2.55)$$

$$-\frac{dB}{dz} = i\Delta B + i\kappa A. \quad (2.56)$$

Furthermore, for small signal powers, the gain equation is simply

$$g = g_0. \quad (2.57)$$

For uniform gratings (i.e., gratings where δ and κ do not vary along z), the coupled-mode equations (2.55) and (2.56) are ordinary differential equations with constant coefficients. The general solution is given by

$$A(z) = A_1 \exp(i\gamma z) + A_2 \exp(-i\gamma z), \quad (2.58)$$

$$B(z) = B_1 \exp(i\gamma z) + B_2 \exp(-i\gamma z), \quad (2.59)$$

where

$$\gamma_1 = \sqrt{\Delta^2 - \kappa^2} = \gamma, \quad \gamma_2 = -\sqrt{\Delta^2 - \kappa^2} = -\gamma \quad (2.60)$$

are the eigenvalues of the coefficient matrix of the coupled-mode equations, and A_1, A_2, B_1 , and B_2 are constant coefficients. The following relations between these coefficients are obtained by substituting the general solutions into the coupled-mode

equations:

$$A_2 = B_2 r, \quad (2.61)$$

$$B_1 = A_1 r, \quad (2.62)$$

$$r = (\gamma - \Delta)/\kappa, \quad (2.63)$$

where r can be interpreted as the effective reflectivity of the grating [55]. { Note that the effective reflectivity is the same for each expression (2.61) and (2.62) because the coupling coefficient is the same for each coupled-mode equation (2.55) and (2.56). The reflectivity is not the same for cases where different coupling coefficients arise, such as for complex-coupled DFB devices [54] }. Using the effective reflectivity, the counterpropagating fields are

$$A(z) = A_1 \exp(i\gamma z) + r B_2 \exp(-i\gamma z), \quad (2.64)$$

$$B(z) = r A_1 \exp(i\gamma z) + B_2 \exp(-i\gamma z), \quad (2.65)$$

where the remaining coefficients A_1 and B_2 are determined by the appropriate boundary conditions.

2.5 Transfer-Matrix Formulation

In this section, we use the small-signal, steady-state solutions (2.64) and (2.65) of the governing equations to construct a transfer matrix. This matrix transfers the forward- and backward-propagating fields (A and B) from the input facet (defined as $z =$

$-\ell/2$) to the output facet ($z = \ell/2$), i.e.,

$$\begin{bmatrix} A(\ell/2) \\ B(\ell/2) \end{bmatrix} = \begin{bmatrix} T_{11} & T_{12} \\ T_{21} & T_{22} \end{bmatrix} \begin{bmatrix} A(-\ell/2) \\ B(-\ell/2) \end{bmatrix}. \quad (2.66)$$

To solve for the T_{mn} matrix elements, we first evaluate the solutions (2.64) and (2.65) at the input facet to obtain the following expressions for the coefficients:

$$A_1 = \frac{A(-\ell/2) - rB(-\ell/2)}{(1 - r^2) \exp(-i\gamma\ell/2)}, \quad B_2 = \frac{B(-\ell/2) - rA(-\ell/2)}{(1 - r^2) \exp(+i\gamma\ell/2)}. \quad (2.67)$$

Substituting the expressions for A_1 and B_2 into Eqs. (2.64) and (2.65) evaluated at the output facet readily yields the following transfer-matrix elements:

$$T_{11} = \frac{1}{1 - r^2} [\exp(i\gamma\ell) - r^2 \exp(-i\gamma\ell)] \quad (2.68)$$

$$T_{12} = -\frac{r}{1 - r^2} [\exp(i\gamma\ell) - \exp(-i\gamma\ell)] \quad (2.69)$$

$$T_{21} = +\frac{r}{1 - r^2} [\exp(i\gamma\ell) - \exp(-i\gamma\ell)] \quad (2.70)$$

$$T_{22} = \frac{1}{1 - r^2} [\exp(-i\gamma\ell) - r^2 \exp(i\gamma\ell)]. \quad (2.71)$$

2.6 Bragg Resonances

Using a transfer matrix, we now study the output power of a low-power signal (such that $P \ll P_{\text{sat}}$) from a uniform-grating DFB SOA. Assuming a single input signal incident at the left-hand facet defined to be at $z = -\ell/2$, the boundary conditions are $A(-\ell/2) = h$ and $B(\ell/2) = 0$. Using these conditions with the transfer matrix Eq. (2.66), we obtain the following expressions for the transmittivity T_y and reflec-

Table 2.1: Parameter values used in simulations.

Physical Quantity	Symbol	Value
Device length	L	$300 \mu\text{m}$
Active-region width	W	$2 \mu\text{m}$
Active-region depth	d	$0.15 \mu\text{m}$
Differential gain	a	$6 \times 10^{-16} \text{ cm}^2$
Transparency carrier density	N_0	$0.4 \times 10^{18} \text{ cm}^{-3}$
Internal losses	α_{int}	0
Coupling coefficient	κ	100 cm^{-1}
Linewidth enhancement factor	α	5
Carrier lifetime	τ	0.2 ns
Saturation power	P_{sat}	10 mW
Confinement factor	Γ	0.32
Modal refractive index	n	3.4
Mode cross section	σ	$10 \mu\text{m}^2$
Signal wavelength	λ	$1.55 \mu\text{m}$

tivity R_y :

$$T_y = \left| \frac{A(\ell/2)}{h} \right|^2 = \left| \frac{1}{T_{22}} \right|^2, \quad R_y = \left| \frac{B(-\ell/2)}{h} \right|^2 = \left| -\frac{T_{21}}{T_{22}} \right|^2, \quad (2.72)$$

which are described solely in terms of the transfer-matrix elements

The transmittivity T_y as a function of normalized detuning δL for several values of gain is shown in Fig. 2.1. Other parameter values used in this calculation and throughout this thesis are given in Table 2.1; as a reference, a spectral width of $\delta L = 1$ corresponds to 0.37 nm (about 46 GHz) for a 300- μm -long DFB amplifier operating near 1.55 μm . This figure shows that Bragg resonances occur at either side of the photonic bandgap, a region of relatively low transmission in the center of the resonance spectrum. The photonic bandgap is centered at the Bragg wavelength $\lambda_B = 2\Lambda n$, where the corresponding Bragg detuning is given by $\delta_B L = gL\alpha/2$.

The Bragg wavelength, photonic bandgap, and Bragg resonances all shift to higher values of detuning (smaller values of wavelength) as the gain is increased because of the associated decrease in refractive index, represented by the linewidth enhancement factor α . The shift of these features for a change in gain Δg are given in terms of the changes in the Bragg wavelength $\Delta\lambda_B$ and Bragg detuning $\Delta\delta_B$ as

$$\Delta\lambda_B = -\frac{\Lambda\lambda_B}{\pi} \frac{\Delta g \alpha}{2}, \quad \Delta\delta_B L = \frac{\Delta g L \alpha}{2}. \quad (2.73)$$

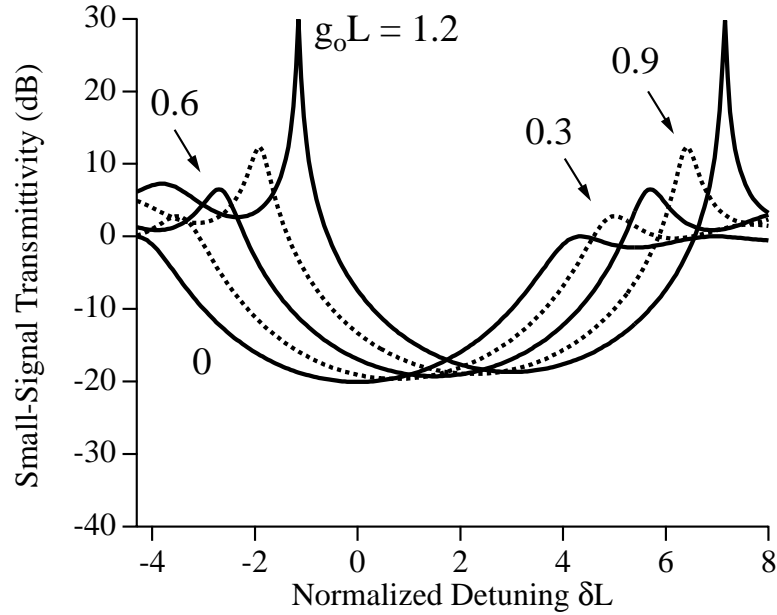


Figure 2.1: Evolution of the small-signal transmittivity spectrum with change in gain.

The resonance structure shifts as the small-signal gain g_0 is varied because we have defined the detuning parameter δ to be *independent* of the linewidth enhancement factor α and gain g , as per Eqs. (2.45) and (2.46). Other formulations (e.g., [52]) define a detuning parameter that *includes* the gain-dependence of the refractive; suppressing α in this way leads to a horizontal axis that is a function of the (physically uninteresting) wavelength within the material λ/n , and the Bragg resonances do not shift position [52]. The ability to shift the Bragg resonances relative to the

input-signal wavelength is a key concept for the signal processing considered in this thesis, and we therefore prefer to make this shifting explicitly apparent in the graphs we present.

In addition to the spectral shift, the Bragg resonances grow as the gain is increased. The peaks will continue to grow until infinity, where infinite transmittivity (finite output for zero input) is interpreted as lasing threshold [62]. Beyond the lasing-threshold value of gain, the peaks decrease; lasing action is not actually predicted to occur because we have neglected amplified spontaneous emission (ASE) in our model. Therefore, we must take care to remain below lasing threshold so that our simulations are physically valid. In our simulations, we typically drive the small-signal gain g_0 to provide a 30-dB peak transmittivity.

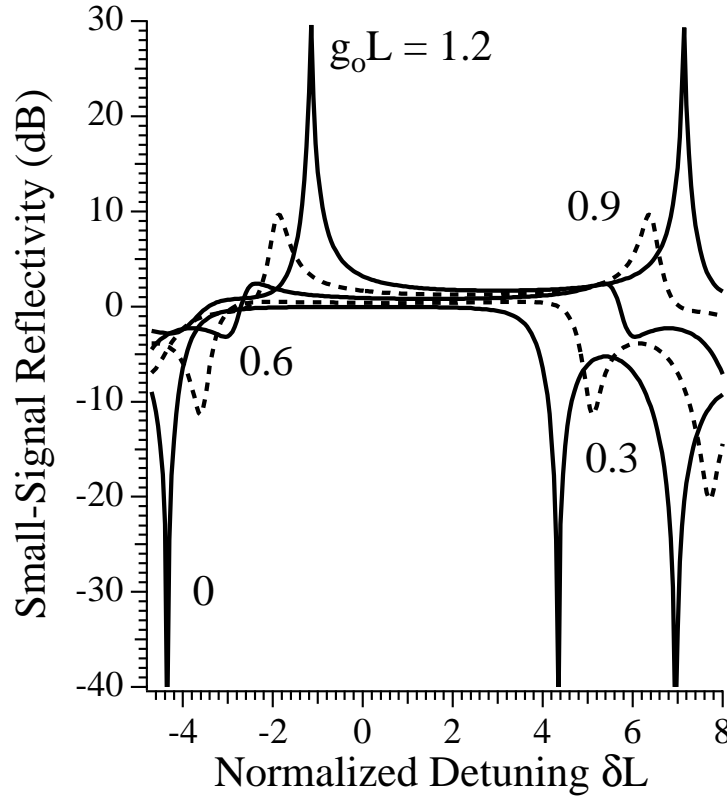


Figure 2.2: Evolution of the small-signal reflectivity spectrum with change in gain. Reflectivity resonances at the stop-band edges reshape from a peak to a dip, and shift to longer signal wavelengths, as gain is decreased.

Lasing threshold can also be determined by the reflectivity resonances, which also reach infinity. As the gain is decreased from lasing threshold, however, the reflectivity resonances behave quite differently than the transmittivity resonances, as shown in Fig. 2.2. For large amounts of gain (enough to approach lasing threshold), reflectivity resonances occur as peaks at both edges of the photonic bandgap, as seen in Fig. 2.2 for $g_o L \approx 1.2$. As the gain is decreased, the reflectivity peaks begin to diminish, and dips appear at wavelengths slightly farther away from the bandgap. This reshaping of the reflectivity resonances is apparent in Fig. 2.2 for $g_o L = 0.6$. With decreased gain, the peaks completely disappear and the dips push downward; for $g_o L = 0$ (the case of passive filters), the reflectivity resonances are deep dips.

2.7 Conclusion

In this chapter, we presented the theoretical foundation of our research. We derived a set of equations that govern the counterpropagating optical fields (2.43) and (2.44) and the SOA gain (2.52). We solved these equations for the steady-state, low-power regime where gain saturation can be ignored. Using this simple solution, we constructed a transfer matrix, which will be used in Chapter 3 to study optical bistability and in Chapter 4 to study the effects of nonuniform gratings. In the present chapter, we used the transfer matrix to study the small-signal gain dependence of the Bragg resonances. The small-signal behavior of the Bragg resonances will prove to be insightful to understand even the *nonlinear* response of DFB SOAs investigated in upcoming chapters.

The transmittivity and reflectivity spectrums clearly show two major effects of gain (or, likewise, the carrier density). First, as the gain is decreased, the refractive index increases and the photonic bandgap and Bragg resonances shift to longer wavelengths (i.e., smaller values of the detuning δ). This coupling between the gain and refractive index is represented by the linewidth enhancement factor α , and gives rise

to the dispersive optical bistability studied throughout this thesis. Second, the gain also changes the height of the Bragg resonances. On reflection, this has the significant effect of inverting the resonance from a peak to a dip at low gain. This inversion gives rise to a wide variety of shapes exhibited by the hysteresis curve on reflection, as will be shown in the following chapter.

Chapter 3

Optical Bistability: Steady-State Analysis

3.1 Introduction

Optical bistability can be used for all-optical processing applications such as logic [9], switching [11], optical limiting [17], memory [23], and signal regeneration [26]. A common place to begin the analysis of bistable systems is with the calculation of the steady-state response [63]. This response provides a benchmark for the time-dependent response, and its description introduces many concepts used throughout this thesis. We begin by developing a transfer-matrix method, to take into account variations in optical power within the DFB SOA and to calculate steady-state bistability. We discuss the physical process of bistability, as well as its spectral range, spectral uniformity, and shape of hysteresis curves on transmission and reflection.

3.2 Physical Process of Bistability

Optical bistability is characterized by an input-output transfer function that doubles back on itself, as shown in Fig. 3.1 for the average power within a DFB SOA. We describe this *steady-state* transfer function as a “hysteresis curve,” even though the term “hysteresis” implies dependence on the previous temporal state of the system.

This description will be justified in Chapter 5, where we show agreement between the steady-state and time-dependent solutions.

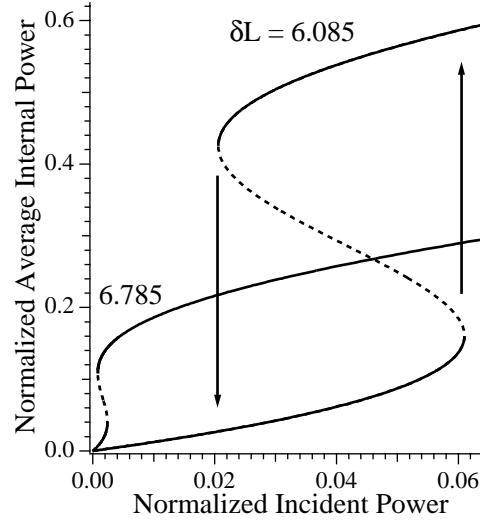


Figure 3.1: Average-internal-power hysteresees for two signal wavelengths. The longer signal wavelength [$\delta L = 6.085$ via Eq. (2.46)] exhibits higher switching thresholds. Dashed portions of curves are unstable.

Bistable switching in DFB SOAs occurs via a positive-feedback loop involving the gain-dependent refractive index, a Bragg resonance, and the internal optical power. An optical signal enters the amplifier with a wavelength longer than that of a Bragg resonance. The optical signal saturates the gain and shifts the photonic bandgap and the associated Bragg resonances to longer wavelengths. If a Bragg resonance shifts onto the signal wavelength, the internal optical power increases even more. As a result, the refractive index continues to increase, and the resonance shifts even farther. This positive feedback loop for the internal optical power moves the Bragg resonance fully through the signal wavelength. The resulting jump experienced by the internal power is indicated by the up-arrow in Fig. 3.1.

The reverse process occurs at the down-arrow. If the incident power is lowered so that the signal wavelength returns to the peak of the Bragg resonance, a subsequent decrease in incident power allows the gain to partially recover, thereby decreasing the refractive index. The Bragg resonance, in turn, shifts to shorter wavelengths and

away from the signal wavelength, decreasing the internal power further. This positive feedback loop shifts the resonance off of the signal wavelength and the internal power switches downward. These upward and downward switching processes give rise to the a S-shaped hysteresis curve, a common shape exhibited by many bistable systems.

3.3 Transfer-Matrix Analysis

Optical bistability occurs as the gain of the SOA is saturated by the optical power within the device. We calculate the steady-state power distribution along the DFB SOA via a transfer-matrix method [64]. For this method, an amplifier of length L is treated as a series of smaller sections of length ℓ , and each section is represented by transfer matrix \mathcal{T} of the kind constructed in Section 2.5.

The series of transfer matrices maps an input-field vector at $z = -L/2$ to the output-field vector at $z = +L/2$ in the following manner:

$$\begin{bmatrix} A(\frac{L}{2}) \\ B(\frac{L}{2}) \end{bmatrix} = \mathcal{T}(g_M) \mathcal{T}(g_{M-1}) \dots \mathcal{T}(g_3) \mathcal{T}(g_2) \mathcal{T}(g_1) \begin{bmatrix} A(-\frac{L}{2}) \\ B(-\frac{L}{2}) \end{bmatrix}, \quad (3.1)$$

where we have explicitly written the gain-dependence of each matrix of a series of M matrices. The first matrix $\mathcal{T}(g_1)$ transfers the input field vector and generates a new field vector at a length ℓ into the device. Subsequent application of the transfer matrices $\mathcal{T}(g_2)$ – $\mathcal{T}(g_M)$ yields an internal-field distribution with $M - 1$ samples spaced at a distance ℓ . Equation (2.53) can then be used to obtain the corresponding internal-power distribution.

The internal power along the device saturates the SOA gain. The gain, however, is used to calculate transfer-matrix elements, which are used to compute the optical-power distribution. To account for this nonlinear behavior, we solve for the gain and power profiles along the device using the following iterative approach:

1. A first-order approximation of the internal-power distribution is calculated assuming no gain saturation, i.e., $g = g_0$.
2. An approximate value of the power within each subsection is calculated by simply averaging the power values at each end of the subsection.
3. The gain for each section is recalculated using equation (2.54) and the power value from step 2.
4. New, power-modified transfer matrices are calculated for the amplifier by using the saturated gain from step 3 and Eqs. (2.45), (2.60), and (2.63).
5. The internal-power distribution is recalculated using the transfer matrices from step 4.
6. Steps 2-5 are repeated until the deviation from the previous power distribution is smaller than the desired error.

We find that 15 iterations (for 8 sections) are typically enough to obtain less than 0.1% deviation in the optical power from one iteration to another.

To calculate the bistable hysteresis curve, the initial field vector used to compute the internal-power distribution is not taken to be the field vector at the input facet, since this field leads to *two* stable solutions at the output facet. Instead, the power computation begins with an assumed *output* field vector and the inverse of each transfer matrix is applied as follows:

$$\begin{bmatrix} \sqrt{P_{in}} \exp(i\phi_{in}) \\ \sqrt{R_p} \exp(i\phi_R) \end{bmatrix} = \mathcal{T}^{-1}(g_1) \quad \mathcal{T}^{-1}(g_2) \quad \mathcal{T}^{-1}(g_3) \quad \dots \quad \mathcal{T}^{-1}(g_{M-1}) \quad \mathcal{T}^{-1}(g_M) \quad \begin{bmatrix} \sqrt{T_p} \\ 0 \end{bmatrix}, \quad (3.2)$$

where T_p is the (chosen) transmitted power, R_p is the (calculated) reflected power, P_{in} is the (calculated) input power, ϕ_{in} is the (calculated) input-field phase, and ϕ_R is the (calculated) reflected-field phase. To map out the hysteresis curve, the transmitted

power T_p is varied from zero to a sufficiently large value to move beyond the region of bistability. Such a transfer-matrix method had been never been used to study optical bistability in DFB SOAs, although a similar method was presented for Kerr-nonlinear devices [72], where an analytic expression for the internal power was used instead of an average-power approach as in step 2 above.

To determine the number of matrices M required for a sufficient sampling of the internal power, we monitored the hysteresis curve as a function of increasing M . Typically, only 8 matrices ($M = 8$) were required before convergence; for the hysteresis curves presented in this thesis, we use $M = 30$. For a 300- μm -long SOA, each section then has a length $\ell = 10\mu\text{m}$.

3.4 Spectral Range and Uniformity

Using the transfer-matrix method, we plot the transmitted power in Fig. 3.2(a) for $g_0L = 1.19815$ and $\delta L = 6.785$; upward switching occurs near 24 μW , and the signal experiences an on-state gain of about 15 dB. To examine the *entire* spectral range of switching, we plot the input powers required for upward and downward switching (i.e., the turning points of the hysteresis) as a function of δL in Fig. 3.2(b) [65]. The two spectral regions apparent in the figure, referred to simply as the long- and short-wavelength sides of the stopband, exhibit a spectral range of about 2 and 2.7 δL , respectively. This corresponds to a spectral range of 0.73 nm (91 GHz) and 0.98 nm (123 GHz), respectively, for a 300- μm -long device operating near 1.55 μm .

The low-power onset of switching for each of the two spectral regions shown in Fig. 3.2 occurs at a value of δL near a small-signal transmittivity peak shown in Fig. 2.1 (for the high value of g_0L). The switching powers increase for smaller values of δL , which correspond to larger initial separations between the Bragg resonance and the signal wavelength; larger powers are required to shift the Bragg resonance to a spectral location where the positive feedback loop is seeded.

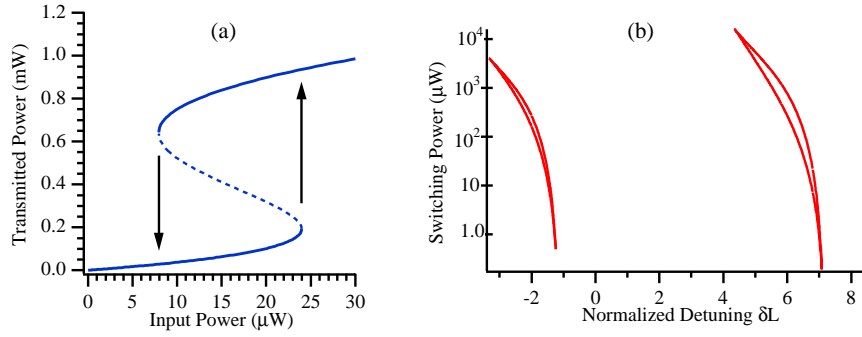


Figure 3.2: (a) Bistable transmission for $\delta L = 6.785$. (b) Upward- and downward- switching input powers plotted over the entire spectral range of bistability.

Switching powers in Fig. 3.2(b) range from 1 μ W to 10 mW. A more important spectral range is that for which the upward-switching power remains below a level that is practical for optical communication systems. We choose this power level to be 0.1 mW. The spectral range of switching below 0.1 mW is only $0.51 \delta L$, or about 0.19 nm (23 GHz), for switching at both sides of the photonic bandgap.

The switching powers in this low-power spectral range vary by about two orders of magnitude; the greatest change (or, the poorest degree of spectral uniformity) occurs near the onset of bistability. Accompanying these changes in the switching powers are changes in other features of the hysteresis curve such as the on-state powers and on-off switching ratios. To investigate the spectral uniformity of the bistable hysteresis, we consider a range of 12.5 GHz (0.1 nm), which corresponds to $0.275 \delta L$. The long-wavelength end of this spectral range is chosen so that its upward-switching power is equal to 0.1 mW.

Bistable output behavior over 12.5 GHz on both sides of the stop band is shown in Fig. 3.3 [66]. A 4.17-GHz separation is chosen between the signal wavelengths of each hysteresis curve. A greater spectral uniformity in terms of switching powers is evident for transmission on the short-wavelength side. Each hysteresis curve overlaps with its adjacent hysteresis curve (although not with the others). Moreover, a single power level separating on- and off-transmitted powers can be defined over the entire

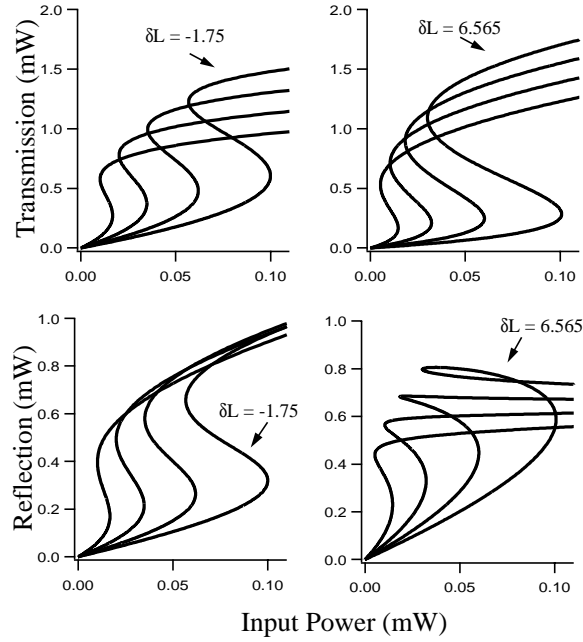


Figure 3.3: Bistable output spanning a spectral range of 12.5 GHz ($\delta L = 0.275$) for optical signals incident on the long- (left figures) and short- (right figures) wavelength side of the photonic bandgap. The wavelength spacing between each hysteresis is 4.17 GHz.)

spectral range. Transmission on the *long*-wavelength side is less uniform across the spectral range. The hysteretic turning points of two adjacent curves barely touch, and a common power level separating on- and off-transmitted powers cannot be defined.

The spectral evolution of the hysteresis curve on reflection is much more dramatic, and is included in Fig. 3.3, below the transmission curves for the same wavelengths. Although there is greater overlap between switching-threshold powers on the short-wavelength side, the reflective hysteresis shape does not remain uniform. For signal wavelengths tuned away from the onset of bistability, the shape of the hysteresis curve warps into a loop. As a result, the on–off switching ratio at 0.1 mW is less than 1.3. This warping behavior on reflection is discussed in detail in the following section.

3.5 Reflective Bistability

The hysteresis curve on reflection from DFB SOAs exhibits a variety of shapes [17], [67]. This variety is intriguing, in part, because each shape potentially supports a distinct signal-processing application [17]. The shapes are also important to understand because, whether or not the switching features are utilized in processing applications, they occur nonetheless and yield an unexpected nonlinear response.

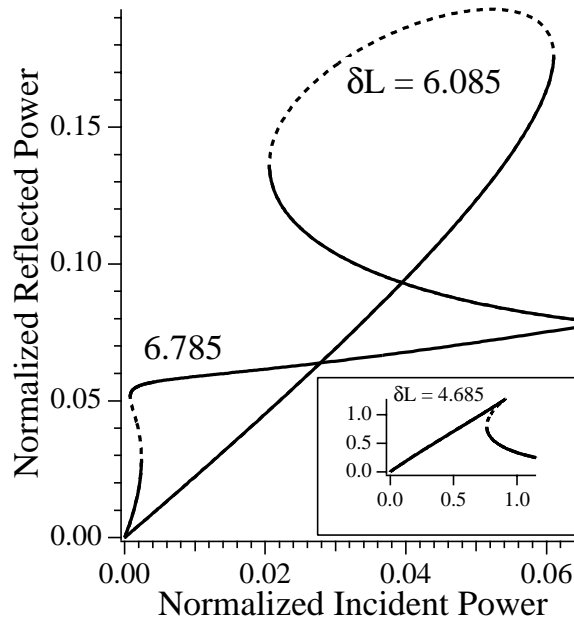


Figure 3.4: Reflected-power hysteresis shapes under conditions identical to those of Fig. 3.1. The inset shows a hysteresis for an even longer signal wavelength. All signal wavelengths are on the short-wavelength side of the stop band. Where the stable branches (solid lines) become unstable, the reflected power switches to the other stable branch at the same incident power.

The reflected hysteresis curves, corresponding to the same conditions as the average-internal power curves in Fig. 3.1, are shown in Fig. 3.4 [67]. Although the internal-power curves are both S-shaped, the reflected-power hystereses take on different shapes. While the hysteresis curve for the shorter wavelength ($\delta L = 6.785$) is S-shaped, the longer wavelength signal exhibits a loop-shaped hysteresis curve. A third qualitatively different hysteresis shape, for an even longer wavelength ($\delta L = 4.685$), is given in the inset.

Each reflective hysteresis shares the same switching threshold powers as its corresponding average-internal-power hysteresis. The unstable region, which connects these thresholds, can therefore be determined straightforwardly. The switching thresholds are the same because reflective bistability is supported by the *same* positive feedback loop as the internal hystereses (i.e., one involving the *internal* power).

The switching thresholds increase as the signal is initially tuned farther from the Bragg resonance because the Bragg resonance must be shifted farther to seed the positive feedback loop. Thus, by the time bistable switching occurs, more gain saturation has taken place. This gain saturation significantly affects the reflection resonances, as discussed in Section 2.6, and will likewise affect the shape of the hysteresis curve. This dependence on gain for resonant-type SOAs is a feature that does not (necessarily) exist for switching devices based on a passive $\chi^{(3)}$ nonlinearity.

For signal wavelengths initially tuned close to a cavity resonance, a low internal power is required to seed optical bistability. The relatively low internal power during the positive feedback loop allows the gain to remain relatively high under saturation. Thus, the reflectivity resonance is a peak during the positive feedback loop. Moreover, we find (using the saturated gain profile) that the reflectivity resonance spectrally overlaps the cavity resonance, which is also shaped like a high peak. Since the cavity and reflectivity resonances are similar, the reflected power switches in the same manner, as evident by the S-shaped hysteresis curve of Fig. 3.4. The on-state of this hysteresis after upward switching exhibits about 13-dB amplification.

In contrast, signal wavelengths initially tuned far from the cavity resonance require higher optical powers to seed the positive feedback loop. The correspondingly large internal powers sufficiently saturate the gain that the reflectivity resonance is a dip during the switching process. As the reflectivity resonance shifts to longer wavelengths, the reflected signal power drops accordingly. Thus, the reflected power switches downward even though the average internal power switches upward. This behavior gives rise to an inverted-S-shaped hysteresis curve, like the one in the inset

of Fig. 3.4. The on-state typically exhibits no amplification since the gain is strongly saturated. Notice that the high-incident-power tail of this hysteresis pushes down beyond the switching thresholds. The signal is simply experiencing the deepening reflectivity dip.

The remaining hysteresis curve of Fig. 3.4 is shaped like a loop. The top of the loop is unstable and switching occurs down from both sides [17] from on-states of a few dB in amplification. The loop-shaped hysteresis curve occurs in a spectral range between the hystereses shapes described above. For these signal wavelengths, the internal powers saturate the gain to levels where the cavity resonance is reshaping from a peak to a dip (see $g_0 L = 0.6$ in Fig. 2.2). The reflectivity peak and dip straddle the central wavelength of the cavity resonance, with the peak slightly closer to the stop band.

For reflection from the short-wavelength edge of the stop band, as in Fig. 3.4, the reflectivity resonance peak occurs at a longer wavelength than the cavity resonance. Since the bistable signal is initially tuned to the long-wavelength side of the internal-power Bragg resonance, the reflectivity peak may completely pass through the signal wavelength, resulting in an increase and then decrease in the reflected power. This kind of a mismatch between the internal and output resonances was shown to give rise to loop-shaped hystereses in other nonlinear media as well [68], [69]. For DFB SOAs, downward switching on the high-incident-power side of the hysteresis is facilitated by the reflectivity resonance dip. As the stop band shifts to longer wavelengths, this dip shifts into the optical signal. Moreover, gain saturation during the positive feedback loop will push the dip to lower values of reflectivity while quenching the resonance peak.

An interesting feature of the loop-shaped hysteresis curve is that its shape is qualitatively different for reflection at the two edges of the stop band. On the *long*-wavelength edge, the loop occurs predominantly *under* the stable-power branches. The bottom portion of the loop is unstable and upward switching occurs at both sides,

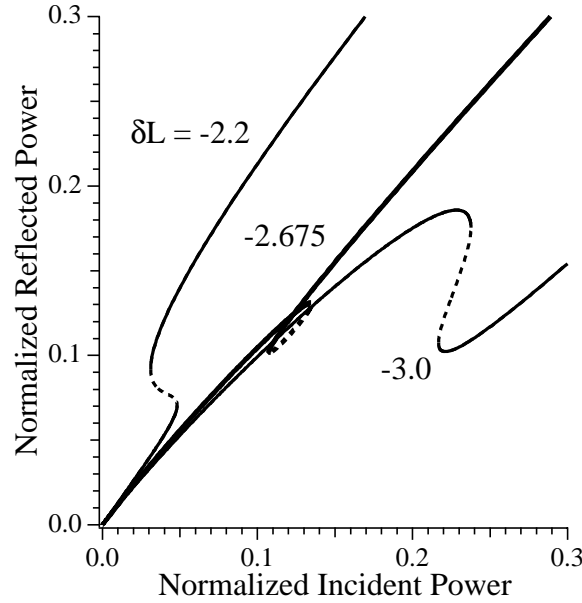


Figure 3.5: Bistable behavior of the reflected power for three signal wavelengths on the *long*-wavelength edge of the photonic bandgap. The middle curve is a new hysteresis shape — a loop that occurs below the stable branches.

as shown in Fig. 3.5; a loop shape of this kind on the long-wavelength side of the stop band was not found in previous studies. Here, we have left out the full spectral evolution of the hysteresis curve to focus on the loop at $\delta L = -2.675$. During the transition from one hysteresis shape to another, upward and downward switching may occur, in general, on either side of loop-shaped hystereses.

The origin of such a loop may be understood as follows. For reflection from the long-wavelength edge of the stop band, the reflectivity resonance peak and dip straddle the central wavelength of the cavity resonance with the *dip* at the longer wavelength. Therefore, as the photonic bandgap shifts to longer wavelengths, the bistable signal is affected first by the reflectivity dip and then the peak. Consequently, the reflected signal decreases and then increases, giving rise to the particular shape of the hysteresis loop. In our calculations for Fig. 3.4, we find that even though the bottom of the reflectivity dip is not reached, the reshaping of the reflectivity reso-

nance is sufficient to initially pull the reflected power down. The resulting on–off switching ratios are small. Moreover, since the summit of the reflectivity peak is not encountered, large amplification is not realized.

3.6 Conclusion

In this chapter, we discussed the steady-state, bistable response of DFB SOAs. A transfer-matrix method, which incorporates the optical power distributed along the amplifier, was presented to analyze such behavior. We began by calculating the entire spectral range of bistability for typical parameter values, and found that it spanned about 1 nm on either side of the photonic bandgap; the wavelength range of bistability was limited because this type of bistability is a resonant phenomenon. Over this range, the shape of the hysteresis curves, in terms of its switching threshold powers and output powers, varied significantly. The most dramatic change occurred on reflection, where the familiar S-shaped hysteresis curve was warped into a loop-shaped or inverted S-shaped curve for different wavelengths.

The wide variety of shapes exhibited by the reflected-power hysteresis curve occurred because the change in refractive index, which gives rise to bistable switching, was accompanied by gain saturation. The decrease in gain, in turn, transformed the reflectivity resonances from peaks to dips, thereby changing the reflected power. The shapes of the hysteresis curve were dependent on wavelength because signal wavelengths that were initially further detuned from the Bragg resonance required more power to seed bistability, and thus incurred greater gain saturation.

For applications to fiber-optical communications, we closely examined bistable switching for input powers below 0.1 mW. We found the spectral range of low-power switching to be only 23 GHz for switching at either side of the photonic bandgap. Moreover, this low-power region exhibits poor spectral uniformity. We studied the variation of the bistable hysteresis curve over a 12.5-GHz spectral range on reflec-

tion and transmission, for signal wavelengths on both sides of the photonic bandgap. Even in the case of greatest spectral uniformity (transmission on the short-wavelength side), the switching thresholds cease to overlap for two hystereses detuned by about 8 GHz. This wavelength sensitivity may limit the performance of optical memory, for example, where the bistable signal must be tuned between the switching thresholds. In Chapter 4, we seek to increase the spectral range and improve the spectral uniformity of the hysteresis by varying the grating period along the built-in grating.

Chapter 4

Nonuniform Gratings

4.1 Introduction

Bistability in DFB SOAs and other resonant-type SOAs exhibits a narrow wavelength range of operation [39]. In the previous section, we quantified this by examining the switching thresholds; switching below 0.1 mW was shown to occur over a 23-GHz spectral range at either side of the photonic bandgap. We also found that the bistable hysteresis changed significantly over a 12.5-GHz spectral range. In this chapter, we seek to increase the spectral range of low-power switching and to improve the spectral uniformity.

The narrow spectral range in DFB SOAs occurs because bistability is based on a Bragg resonance. We seek to broaden the spectral range by varying the Bragg wavelength along the length of the device, i.e., by continuously changing the grating period. This grating nonuniformity is commonly referred to as spatial chirp, since the spatial frequency of the grating $\beta_B = \pi/\Lambda$ varies along the device. The effect of spatial chirp has been studied previously in systems exhibiting dispersive bistability based on the Kerr nonlinearity [70]–[73]; however, these projects focused on such topics as the reduction of switching-threshold powers and the development of a new method of analysis, rather than the improvement in spectral range.

We begin this chapter by discussing a general formalism to incorporate spatial

chirp and other grating nonuniformities into the transfer-matrix method. To illustrate the flexibility of this method, we study the small-signal and bistable response of a phase-shifted DFB SOA, both with and without spatial chirp. We then examine the effect of spatial chirp on the wavelength range and spectral uniformity of bistability. This investigation leads us to uncover a host of notable effects, including dramatic changes in switching powers and in the shape of the hysteresis curve.

4.2 Transfer-Matrix Analysis

For Bragg-grating devices, one way to tailor the output response is to introduce nonuniformities into the periodic structure [50], [62], [72], [74]– [77]. Typical nonuniformities include variation in the grating period (spatial chirp), grating depth (taper), and abrupt phase shifts of the grating corrugation. To simulate the effects of these nonuniformities on the output spectra of DFB devices with moderate grating depth, it is common to use a transfer-matrix method based on a pair of coupled-mode equations [62], [72], [75]– [77]. In this section, we extend our transfer-matrix method, developed in Chapter 3 for the study of optical bistability, to incorporate grating nonuniformities.

4.2.1 Grating Nonuniformities

To incorporate grating-phase shifts, a matrix designed to shift the phase of the optical field is inserted between two transfer matrices corresponding to uniform subsections on each side of the phase shift [76]. The phase-shifting matrix Φ is given by

$$\Phi = \begin{pmatrix} \psi & 0 \\ 0 & \psi^* \end{pmatrix}, \quad (4.1)$$

where $\psi = \exp(i\phi)$ contains the phase shift ϕ experienced by the optical field, and $*$ represents the complex conjugate. As an example, we consider a $\lambda/4$ -shifted DFB

SOA. The matrix series of this device can be written as

$$\begin{bmatrix} A(\frac{L}{2}) \\ B(\frac{L}{2}) \end{bmatrix} = \mathcal{T} \Phi \mathcal{T} \begin{bmatrix} A(-\frac{L}{2}) \\ B(-\frac{L}{2}) \end{bmatrix}, \quad (4.2)$$

where \mathcal{T} is a transfer matrix representing an amplifier segment of length $\ell = L/2$, L is the total length of the DFB SOA, and $\phi = \pi/2$ is the phase shift experienced by the optical field.

The nonuniformity we focus on in the latter half of this chapter is spatial chirp; a DFB SOA with a linearly chirped grating is depicted in Fig. 4.1. The P-direction is defined to be the direction for which an incident optical field sees an *increase* in the grating's spatial frequency $\beta_B = \pi/\Lambda$ (i.e., the Bragg wavenumber). Likewise, an optical field incident in the N-direction sees, by definition, a decrease in the spatial frequency of the grating. ("P" and "N" indicate positive and negative chirp, respectively, in our notation.) The P- or N-direction is specified in computations by the sign of the chirp parameter C , introduced by using

$$\beta_B(z) = \bar{\beta}_B + C \frac{(z - L/2)}{L^2}, \quad (4.3)$$

where $\bar{\beta}_B$ is the average Bragg wavenumber. A positive (negative) value of C corresponds to the P-direction (N-direction), and the magnitude of C represents the total change in $\beta_B(z)L$ along the device. For example, a value of $|C| = 10$ corresponds to a total variation in β_B of about 0.24% for a 300- μm -long device.

For small variations in the period of the grating, the coupled-mode equations (2.55) and (2.56) remain unchanged except that the detuning parameter $\delta = \beta_b - \beta_B$ now becomes z dependent. (A similar argument can be made for tapering the coupling coefficient κ .) The linear spatial chirp considered above is written as

$$\delta(z) = \bar{\delta} - C \frac{(z - L/2)}{L^2}, \quad (4.4)$$

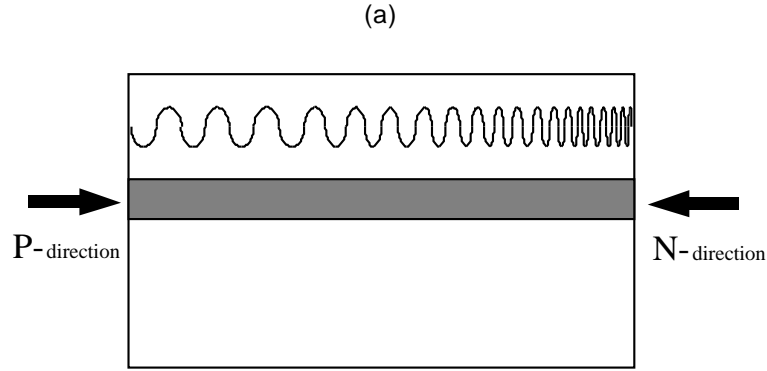


Figure 4.1: Schematic of a DFB SOA with a linearly chirped-grating, indicating the P-direction ($C > 0$) and N-direction ($C < 0$).

where $\bar{\delta}$ is the average detuning and the magnitude of C represents the total change in $\delta(z)L$ along the device.

To incorporate spatial chirp into the transfer-matrix method, the continuous change in the detuning parameter δ is approximated by a step-like distribution; δ is constant for each transfer matrix (as required!), but its value is incremented in a step-like manner from one matrix to the next. A series of M transfer matrices is written in the following manner [compare with Eq. (3.1)]:

$$\begin{bmatrix} A(\frac{L}{2}) \\ B(\frac{L}{2}) \end{bmatrix} = \mathcal{T}(\delta_M, g_M) \cdots \mathcal{T}(\delta_2, g_2) \mathcal{T}(\delta_1, g_1) \begin{bmatrix} A(-\frac{L}{2}) \\ B(-\frac{L}{2}) \end{bmatrix}. \quad (4.5)$$

Since we seek to model a continuously varying grating, we discard the phase mismatch between sections of constant length that occurs between for such a step-like distribution of δ .

The accuracy of this step-like approximation is improved by increasing the number of matrices M while decreasing the length of each subsection ℓ . We find that the output spectrum of a continuously chirped structure with $|C| < 20$ converges for as few as 8 subsections. Unless otherwise noted, we have used 30 sections in our calculations; considering a 300- μm -long device, each section represents 10 μm .

4.2.2 Small-Signal Amplification

Before considering a DFB SOA, it is instructive to discuss results for a non-semiconductor amplifier for which $\alpha = 0$. The transmission spectrum of a $\lambda/4$ -shifted DFB non-semiconductor amplifier is shown in Fig. 4.2(a). The transmission peak centered at $\delta = 0$, caused by the abrupt phase shift in the grating, benefits the most from the distributed feedback; as $g_0 L$ is increased (by increasing the pump current), the central transmission peak grows significantly more than any other spectral region. In the figure, we use values of $g_0 L$ that yield peak transmittivities of 0, 10, 20, and 30 dB ($g_0 L = 0, 0.4360, 0.5854$, and 0.6339 , respectively).

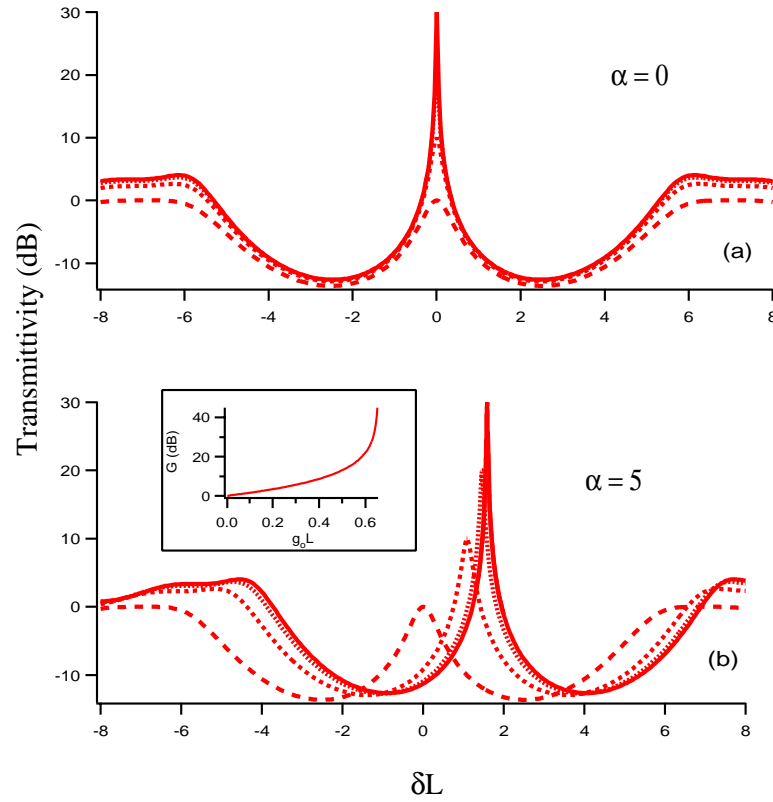


Figure 4.2: Small-signal transmittivity of a $\lambda/4$ -shifted DFB SOA, showing the effect of α . The small-signal gain g_0 is varied to give a peak transmittivity of 0, 10, 20, and 30 dB; the inset shows the change in this peak value as a function of $g_0 L$.

The effect of the linewidth enhancement factor α on the transmission spectrum is

to produce a shift proportional to the change in gain, and is given by Eq. (2.73). This shift is apparent in Fig. 4.2(b), where $\alpha = 5$. The shift between transmission peaks decreases for higher values of gain because less increase in g_0L is needed for a 10-dB increase in the transmittivity [see inset of Fig. 4.2(b)]. The capability of tuning the transmission peak via direct variation of g_0L (i.e., pump current) enriches the device applications of semiconductor amplifiers. For example, this tunability has been used as the basis of a tunable filter with resonant optical amplification [47].

As an example of the effect of linear spatial chirp on the transmission spectra of a DFB SOA, we add this nonuniformity to the $\lambda/4$ -shifted amplifier considered above. For the unchirped case, the wavelength corresponding to the Bragg wave number experiences the greatest feedback and exhibits the most amplifier gain. Feedback for this wavelength, though, is reduced when chirp is introduced because the Bragg wavelength is varied throughout the device. As a result of lower feedback, higher values of the small-signal gain g_0L are required to realize peak transmission values of 10, 20, and 30 dB. This effect can be seen in Fig. 4.3, where we show the wavelength dependence of the amplifier transmittivity for a linearly chirped, $\lambda/4$ -shifted DFB SOA with $C = 20$, where $g_0L = 1.4200, 2.1912$, and 2.4914 , respectively. Since higher gain is required, the transmission spectrum is consequently shifted to higher values of δ compared to the case $C = 0$ [see Fig. 4.2(b)]. The transmittivity peaks also widen, also resulting from the decrease in feedback to the center of the peak. When comparing Fig. 4.3 and Fig. 4.2(b), note that the *wavelengths* corresponding to the values of δ are determined by Eq. (2.46); the wavelength of any peak from Fig. 4.3 can be made to coincide with the wavelength of any peak from Fig. 4.2(b) by considering, for example, devices of two different grating periods Λ .

The example of a $\lambda/4$ -shifted DFB SOA with and without spatial chirp also illustrates that grating nonuniformities can alter the lasing threshold. In particular, the 30-dB transmittivity peak for the chirped-grating case occurred at $g_0L \simeq 2.5$; this value of the small-signal gain is over twice that needed to *lase* the unchirped device. From

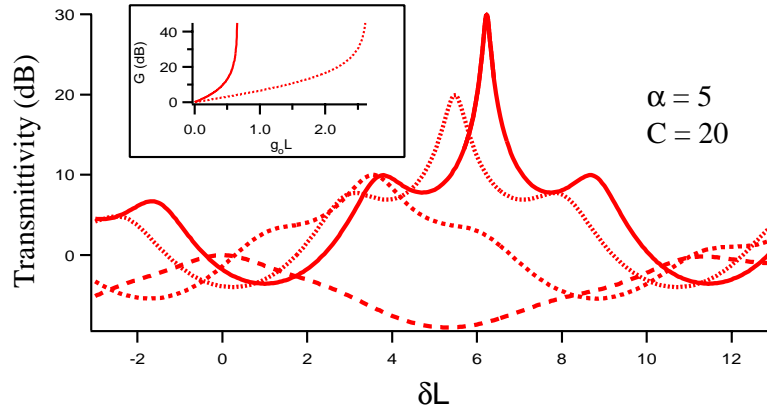


Figure 4.3: Small-signal transmittivity of a $\lambda/4$ -shifted DFB SOA with spatial chirp. The small-signal gain g_0 is varied to give a peak transmittivity of 0, 10, 20, and 30 dB; the inset shows the change in this peak value as a function of $g_0 L$ for the chirped and unchirped cases.

a computational perspective, *any* value of $g_0 L$ can be used in calculations, but only one that lies below lasing threshold is physically valid, since we have ignored ASE in our model. Thus, care must be taken during the study and design of nonuniform-grating DFB SOAs to keep track of the lasing threshold, an issue that does not exist for passive Kerr-nonlinear devices. When comparing the bistable characteristics of devices with different grating uniformity, we set the normalized small-signal gain $g_0 L$ to deliver a small-signal transmittivity of 30 dB, as a general rule.

4.2.3 Nonlinear Response

To study the nonlinear response of the DFB SOA, we calculate the internal-power distribution, as discussed in Section 3.3. As an example of how the internal power can vary throughout a nonuniform-grating device, we show the internal power for a $\lambda/4$ -shifted DFB SOA with and without spatial chirp in Fig. 4.4. In each case we, have plotted the distribution for three values of δ . The center value of the normalized detuning $\delta_c L$ is chosen to match the transmittivity peak ($\delta_c L = 1.58$ and 6.2 for the

uniform and chirped gratings, respectively); the quantity $\Delta\delta L = (\delta - \delta_c)L$ is the mismatch from the center value of the detuning.

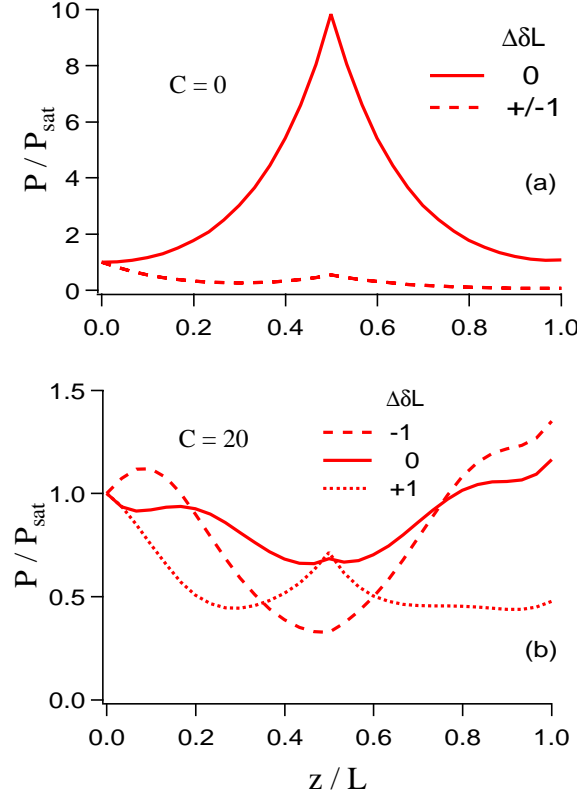


Figure 4.4: Internal power of a $\lambda/4$ -shifted DFB SOA for three values of δ , (a) without and (b) with spatial chirp.

For the uniform-grating case, the signal at $\Delta\delta L = 0$ is strongly localized within the device at the location of the phase shift. Detuning away from this wavelength results in the reduction of the power peak within the device, as shown in Fig. 4.4(a). The power within the amplifier is further distorted by the incorporation of linear spatial chirp. For $C = 20$, the phase-shift-induced peak at the center of the amplifier is almost completely flattened, and the power near each amplifier facet is higher than at the center. In addition, the power distribution is asymmetric about $\Delta\delta L = 0$. As seen in 4.4(b), the short-wavelength side recovers a prominent peak in the center, whereas

the long-wavelength side obtains its lowest value at the center of the amplifier and exhibits higher power near each amplifier facet.

We now turn to comparing the bistable response for chirped and unchirped $\lambda/4$ -shifted DFB SOAs. Starting at a value of δL near the onset of bistability ($\delta L = \delta L'$, decreasing δL will push the switching threshold to larger powers as discussed in Chapter 3. This is evident in Fig. 4.5(a), where the value of $g_0 L$ is chosen to yield an unsaturated peak transmission value of 30 dB, and δL is decreased from $\delta L' = 1.5$ until the switch-on input power reaches an upper limit of about 1% of the saturation power P_{sat} ; a detuning range of approximately $0.3 \delta L$ exists for this region of low-threshold bistable switching.

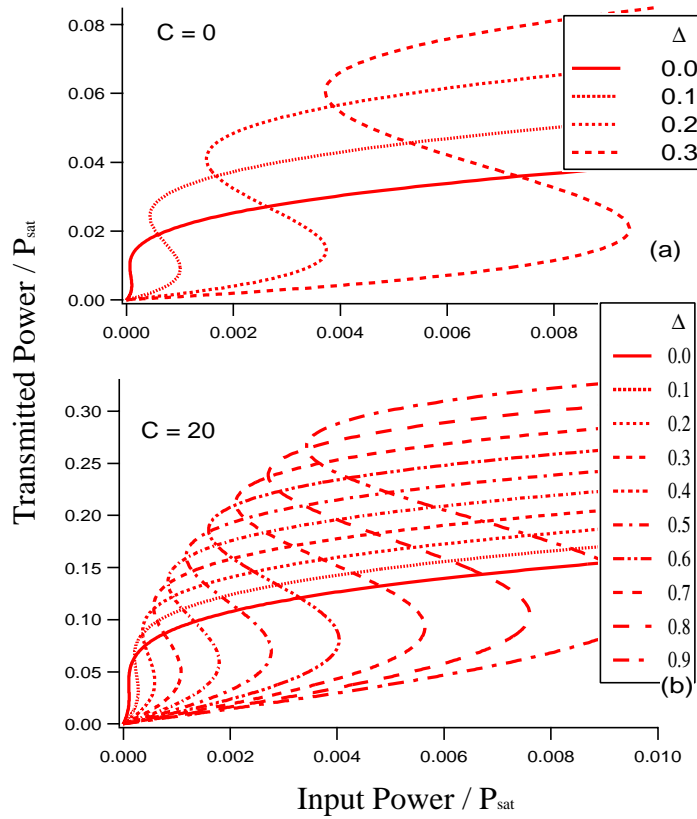


Figure 4.5: Spectral evolution of the bistable hysteresis curve for a $\lambda/4$ -shifted DFB SOA, (a) without and (b) with spatial chirp. $\Delta = \delta L' - \delta L$.

The addition of positive linear spatial chirp to the grating of a $\lambda/4$ phase-shifted

DFB SOA increases the range of wavelengths that support low-threshold bistable switching, for an amplifier driven to provide the same unsaturated peak amplifier gain of 30 dB. This is seen in Fig. 4.5(b), where we show the bistable hysteresis curve for $C = 20$. As in Fig. 4.5(a), the highest value of the δL ($\delta L' = 6.0$) is chosen to be near the onset of bistability and δL is decreased until the switch-on input power reaches 1% of the saturation power. The range of δL values is now 0.9, three times wider than that of the non-chirped case.

Since the transmittivity spectrum of a DFB SOA shifts with the direct variation of gain (see Fig. 4.2), it is possible to tune the bistable hysteresis curve for a fixed wavelength. To illustrate this, we first consider a $\lambda/4$ -shifted amplifier without spatial chirp, and choose the value of δL that is 0.3 δL less than the value for which bistability begins. Fig. 4.6(a) shows the hysteresis curve of this amplifier for four values of gain, beginning from the value of $g_0 L$ that yields an unsaturated transmission peak of 30 dB. As seen in the figure, gain tuning allows the switching powers to be selected.

Using the additional degree of freedom provided by gain-tuning, we can compare the bistability characteristics with and without spatial chirp by maintaining a fixed value of δL and varying $g_0 L$ (in contrast to Fig. 4.5, where the opposite was performed). Using the value of δL that is 0.3 less than the value for which bistability begins, the switch-on input power is much lower for the case $C = 20$ than for the non-chirped device, if each device is driven to provide a 30 dB unsaturated transmission peak (compare the solid lines of Fig. 4.5). The switch-on input powers of the two devices can be set equal by varying the gain of each amplifier. As shown in Fig. 4.6, approximately equal switch-on powers exist for the two devices at input powers just higher than 0.2% of the saturation power.

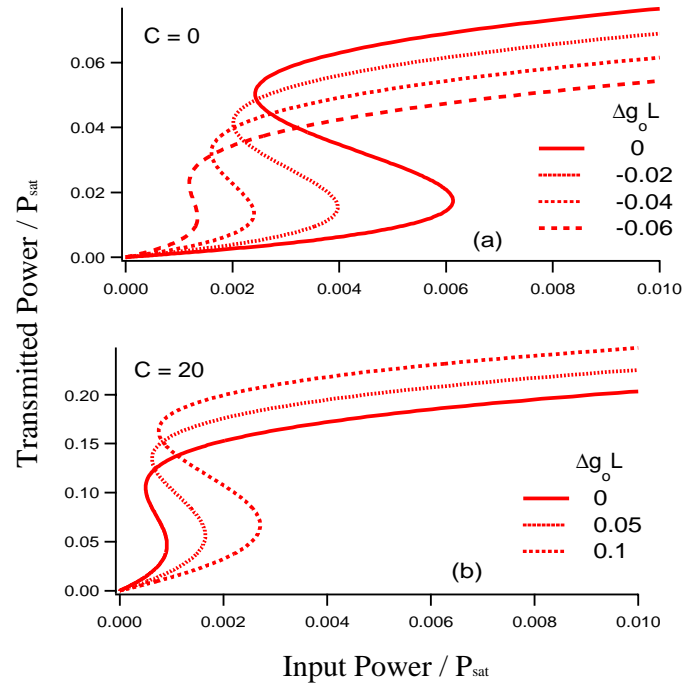


Figure 4.6: Gain tuning of the hysteresis curve for a $\lambda/4$ -shifted DFB SOA, (a) without and (b) with spatial chirp. $\Delta g_0 L = g_0 L - g_0 L_{30dB}$.

4.3 Chirped-Grating DFB SOAs

4.3.1 Spectral Range

The spectral range of bistable switching and the spectral uniformity of the hysteresis shape were found to be limited for the uniform grating studied in Section 3. As seen above for phase-shifted devices, spatial chirp can increase the spectral range of switching; we will investigate improvements to the spectral range and uniformity of a non-phase-shifted DFB SOA in this section.

Since the Bragg wavenumber varies along the length of a chirped-grating device, the feedback within the structure is significantly altered. An increase in the amount of linear chirp weakens the feedback such that the lasing threshold increases [75]. Likewise, the amount of gain required to maintain a transmittivity peak that provides

30 dB of small-signal amplification also increases. For $|C| = 0, 5, 10$, the required values of $g_0 L$ are 1.198, 1.508, and 2.206, respectively, and are used in Fig. 4.7 to plot the small-signal transmittivity spectra. The shift of the photonic bandgap to higher values of normalized detuning δL accompanying an increase in $g_0 L$ results from defining δL to be independent of the carrier density [see Eq. (2.46)], as explained in Section 2.6. While comparing the bistable response, all amplifiers are driven to provide 30-dB small-signal amplification.

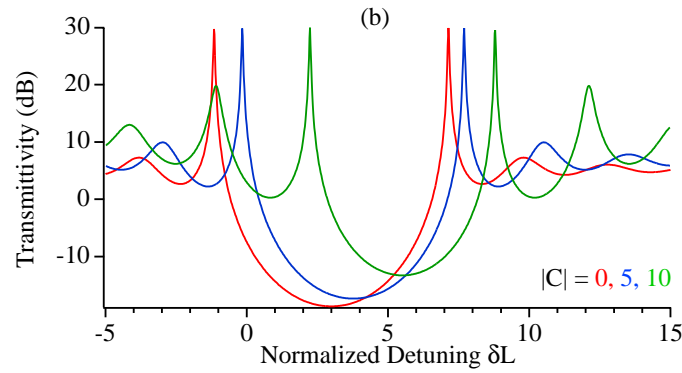


Figure 4.7: Small-signal transmittivity spectra for chirped-grating DFB SOAs, with $|C| = 0, 5, 10$.

The effect of spatial chirp on the entire spectral range for switching at either side of the photonic bandgap is shown in Fig. 4.8 [65]. The switching powers are given in terms of the normalized power \bar{P} (left axis) and for a specific value of $P_{sat} = 10$ mW (right axis). Linear spatial chirp tends to increase the spectral range of bistable switching for signals incident in either the P-direction or N-direction. The largest percent increase in the spectral range occurs at the long-wavelength side of the photonic bandgap for signals traveling in the N-direction. For $C = -10$, a 92% increase results in a spectral width of $\delta L = 3.97$. The broadest total spectral range in Fig. 4.8, however, is exhibited by switching at the short-wavelength side of the photonic bandgap for $C = -10$, and is $5.1 \delta L$, or 1.86 nm (232 GHz). The blue shift of the low-power onset of switching follows the shift of the photonic bandgap with increasing gain, as shown in Fig. 4.7.

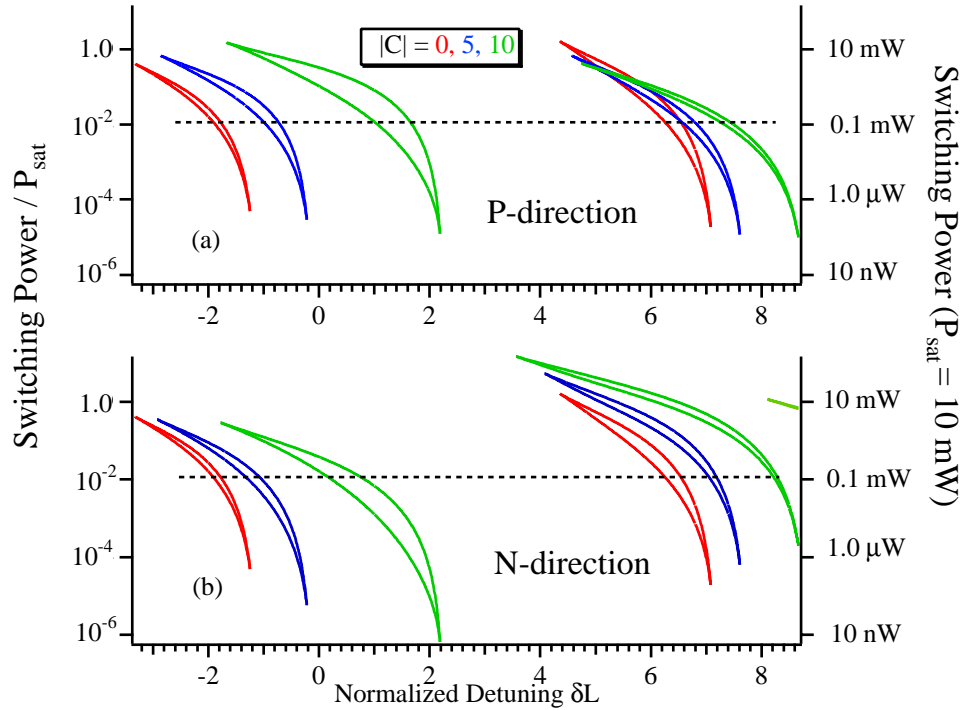


Figure 4.8: Spectral range of bistable switching for optical signals incident in the (a) P-direction and (b) N-direction of a chirped-grating DFB SOA. The long-wavelength side of (b) for $C = -10$ exhibits the lowest overall switching power and the broadest spectral range of low-power switching.

Although signals incident on the short-wavelength side of the photonic bandgap with $C = -10$ exhibit the broadest total spectral range, switching powers tend to *increase*, as compared to the unchirped case. This is consistent with the effect of spatial chirp in passive Kerr-nonlinear devices for switching at the center of the photonic bandgap [70]. Most notably, the low-power onset of bistability increases with spatial chirp. Considering switching powers less than 0.1 mW, the spectral range is only $0.36 \delta L$, or 0.13 nm (16 GHz). Using $P_{sat} = 10$ mW, the 0.1-mW power level corresponds to $0.1 \bar{P}$ and is indicated by the dotted lines in Fig. 4.8.

For optical signals on the short-wavelength side of the photonic bandgap and traveling in the P -direction, switching powers tend to *decrease* with spatial chirp. This is also consistent with studies in passive Kerr-nonlinear devices for switching at the center of the photonic bandgap. In particular, the onset of switching gradually

decreases with increasing spatial chirp and is about $0.1 \mu\text{W}$ for $C = 10$. Since the onset of bistability has dropped, the spectral range of low-power switching has increased; the low-power spectral range is twice as wide as for the unchirped grating.

For switching at the *long*-wavelength side of the photonic bandgap, optical signals incident in both directions see a decrease in the onset of switching with an increase in spatial chirp. Most notably, for $C = -10$, the switching power at the onset of bistability drops below the very low level of 10 nW — two orders of magnitude lower than its value for $C = 0$. Consequently, this case exhibits the widest spectral range of low-power switching; the spectral range is $1.37 \delta L$ (0.5 nm , or 62 GHz), an increase of 2.7 times from the unchirped case.

4.3.2 Spectral Uniformity

We can infer the spectral uniformity of the bistable hysteresis curve from the switching-threshold curves in Fig. 4.8. For low-power switching near 0.1 mW , the horizontal separation between curves is greatest on the long-wavelength side of the photonic bandgap for the case $|C| = 10$. A wide horizontal separation corresponds to a greater overlap of bistable hysteresis at different values of δL . Moreover, this side also exhibits large vertical separation between the switching-power curves; the correspondingly wide hystereses are useful for optical memory because it accommodates a flexible power level of the holding beam. Because of these advantages, we will focus on the long-wavelength side of the photonic bandgap.

For optical signals traveling in the N-direction, bistability exhibits high uniformity over a spectral range of 12.5 GHz [66]. As seen in Fig. 4.9, there is a region of input powers that is common to all hysteresis curves. Thus, a signal with an input power falling within this region can have a wavelength anywhere within this spectral range and still function as a holding beam for optical memory. In particular, the switch-off powers exhibit only a small spectral dependence.

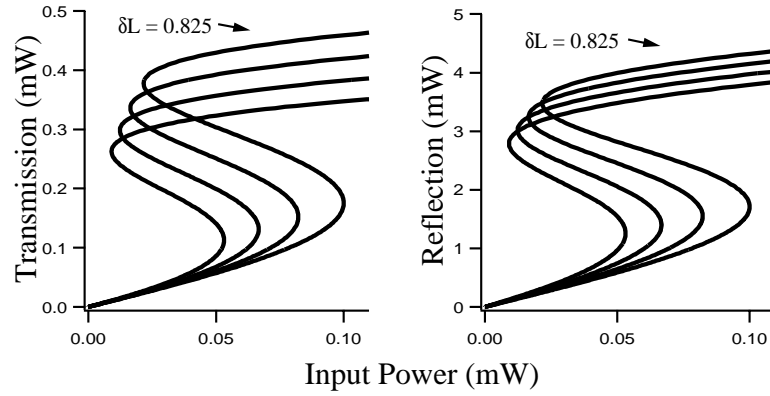


Figure 4.9: Bistable output over a 12.5-GHz ($\delta L = 0.275$) spectral range for $C = -10$ (N-direction). Spectral uniformity is improved over the unchirped case shown in Fig. 3.3.

For the N-direction, we are also able to define a common power level separating on- and off-output powers for both transmission and reflection. Moreover, reflective bistability exhibits a large degree of uniformity in the output power of the on-state. We expect that this is beneficial for switching, since all spectral components of a pulse would experience similar output powers.

This improvement in the spectral uniformity of the hysteresis curve is partially a result of the decreased switching power at the onset of bistability. Since the onset of bistability is pushed below 10 nW, the operating powers near 0.1 mW are far from the region where the hysteresis curve changes dramatically. For comparison, bistable hysteresis curves near the onset of bistability are shown in Fig. 4.10. Here, the sub-microwatt switching powers and greater-than-30-dB on-state gains are intriguing, but the spectral uniformity is so poor that the curves (separated by only 4.17 GHz) barely touch.

For optical signals traveling in the P-direction, the hysteresis curves overlap, but only over a small input-power region, as seen in Fig. 4.11. An interesting feature of optical bistability in this direction is that reflection exhibits loop-shaped behavior over the entire 12.5-GHz spectral range. The prevalence of the loop-shaped hystere-

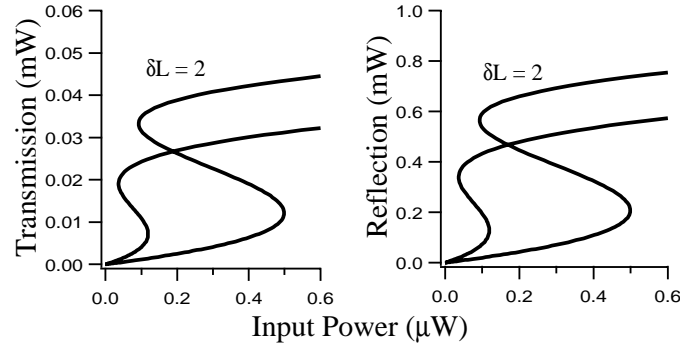


Figure 4.10: Bistable hysteresis curves near the onset of bistability for $C = -10$, exhibiting sub- μW switching thresholds, high gain (> 30 dB), but poor spectral uniformity.

ses is common for signals traveling in the P-direction on the long-wavelength side of the photonic bandgap, and will be discussed in detail in the following section.

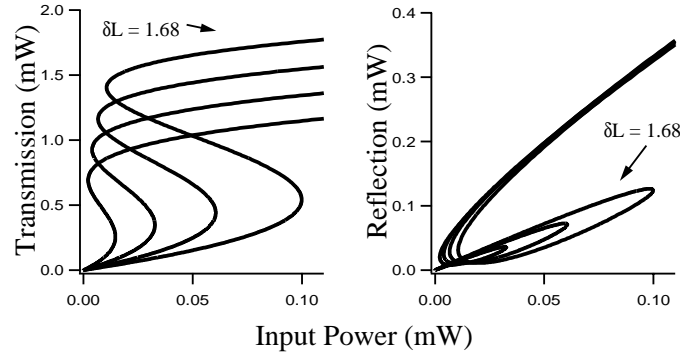


Figure 4.11: Bistable output over a 12.5-GHz spectral range for the P-direction ($C = 10$).

4.3.3 Reflective Bistability

Spatial chirp has a major effect on reflective bistability in DFB SOAs because it changes the saturation behavior of the reflectivity resonances [67]. To illustrate this change, it is instructive to examine the small-signal regime. For optical signals incident in either the P-direction or the N-direction, reflections from the two edges of the photonic bandgap exhibit remarkably different behavior, as seen by the reflectivity spectra shown in Fig. 4.12.

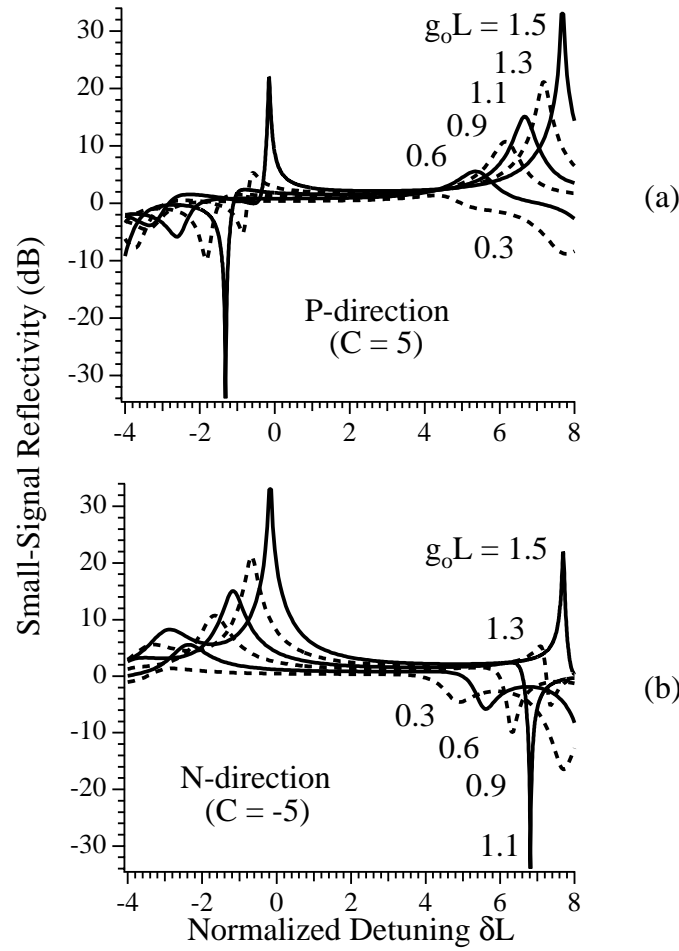


Figure 4.12: Small-signal reflectivity spectra for several values of the small-signal gain $g_0 L$ for the (a) P-direction and (b) N-direction of a linearly chirped DFB SOA with $|C| = 5$. Note how a deep reflectivity dip can be realized near one edge of the photonic bandgap for a relatively high value of gain ($gL = 1.1$).

Reflectivity resonances exhibit peaks in spite of a reduction in gain for short-wavelength signals incident in the P-direction [Fig. 4.12(a)] and for long-wavelength signals incident in the N-direction [Fig. 4.12(b)]. According to Yamada [75], each of these signals has a wavelength that matches the Bragg wavelength away from the input facet, and therefore travels deep into the amplifier before being reflected; the increased gain-length product results in the persistent reflectivity peak.

For these two enhanced-reflection cases, we find that the reflectivity resonances

remain spectrally overlapped with the resonances formed by the average internal power. As a result, the reflected-power behavior mimics that of the internal power, and only S-shaped hystereses occur [67]. Fig. 4.13 shows the spectral evolution of reflective bistability at the long-wavelength edge of the photonic bandgap for optical signals incident in the N-direction. The inverted-S- and loop-shaped hystereses do not appear.

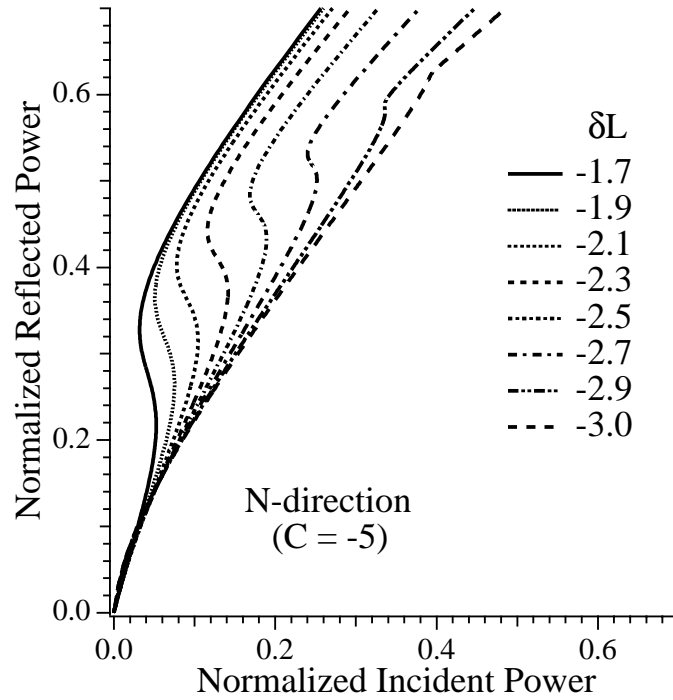


Figure 4.13: Spectral evolution of the reflected-power hysteresis for optical signals incident in the N-direction near the long-wavelength-edge of the photonic bandgap. Parameters are the same as in Fig. 4.12, except that $g_0 L = 1.5081$. The inverted-S- and loop-shaped hystereses do not occur (compare with Fig. 3.5).

In contrast, an *increase* in spectral range for inverted-S- and loop-shaped hystereses occurs for an optical signal with a wavelength that matches the Bragg wavelength near the *input* facet of the DFB SOA. This condition is satisfied for long-wavelength signals incident in the P-direction [Fig. 4.12(a)] and for short-wavelength signals incident in the N-direction [Fig. 4.12(b)]. Here, the reflectivity resonance peak readily diminishes with gain saturation. Moreover, we find that the reflectivity resonance dip

is the most prominent for a *non-zero* value of gain. In Fig. 4.12, large reflectivity dips occur for $g_o L = 1.1$. Increasing the amount of spatial chirp tends to increase the value of gain for which the dip is most prominent. Gain saturation via the optical signal now has an even larger effect on the reflected-power hystereses.

A consequence of the readily inverted resonance peak is that loop-shaped hysteresis curves occur at smaller incident powers. Fig. 4.14(a) shows a loop-shaped hysteresis for an optical signal on the short-wavelength edge of the photonic bandgap, incident in the N-direction of a chirped-grating DFB SOA. The hysteresis is similar in shape to that of Fig. 3.4, but the switching powers are one order of magnitude smaller, at $20\text{-}\mu\text{W}$ for $P_{sat} = 10\text{ mW}$. The loop-shaped hysteresis curves not only occur for smaller incident powers, but also exist over a wider spectral range than for the unchirped case.

As discussed in Section 3.5, the high-incident-power tail of the reflected-power hysteresis pushes down for signal wavelengths on the short-wavelength side of the photonic bandgap. For the chirped-grating case, a deep reflectivity dip can affect the optical signal during the bistable switching process, allowing the bottom of the hysteresis tail to approach zero reflected power. An example is given in Fig. 4.14(b), for a longer optical wavelength than in Fig. 4.14(a). Downward switching occurs from an on-state of about 4-dB amplification with an on-off switching ratio of about 30.

For the *long*-wavelength side of the photonic bandgap, a deep reflectivity dip also affects the optical signal during bistable switching. This causes the hysteresis loop to push down toward zero for the loop- and inverted-S-shaped hysteresis curves, as shown in Fig. 4.15 for signals incident in the P-direction. The on-off switching ratios at the low-incident-power side are greater than 30 for the outer hysteresis curves, which span a spectral range of $\delta L = 0.6$. This corresponds to a spectral width of about 27 GHz for a $300\text{-}\mu\text{m}$ -long device operating near $1.55\text{ }\mu\text{m}$. Within this spectral region, the reflective hysteresis obtains an on-off switching ratio in excess of 10^5 , as

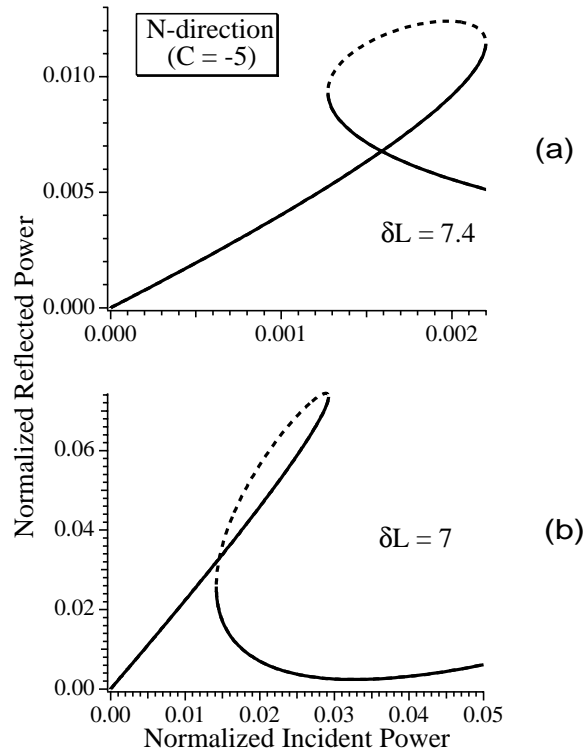


Figure 4.14: Reflected-power hysteresis curve for optical signals incident in the N-direction with wavelengths on the short-wavelength side of the photonic bandgap. The switching thresholds for the loop-shaped hysteresis in (a) are an order of magnitude smaller than those of Fig. 3.4(b). The on-off switching ratio exceeds 30 for the high-incident-power side of the hysteresis curve in (b).

exhibited by the middle hysteresis of Fig. 4.15. In spite of these excellent switching ratios, amplification has been lost since the peaked-reflectivity resonance is not encountered by the optical signal.

4.3.4 Large Amounts of Chirp

For large amounts of spatial chirp, resonances away from the photonic bandgap tend to become stronger. This is apparent in Fig. 4.7; for $|C| = 10$, the outer resonances provide about 20-dB amplification. One consequence is that strong outer resonances can give rise to bistable switching in the *same* spectral region as a neighboring resonance [65]. This behavior is seen in Fig. 4.8 for the case $C = -10$ in the spectral

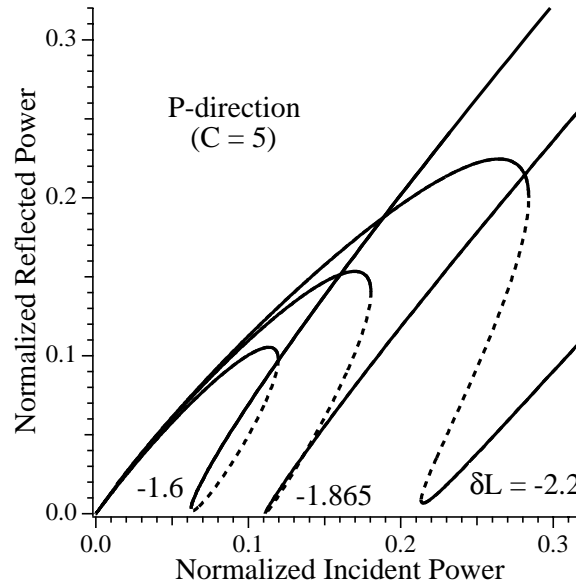


Figure 4.15: Reflected-power hysteresis curves for signals incident in the P-direction with wavelengths on the long-wavelength edge of the photonic bandgap. The on-off switching ratio exceeds 10^5 for the low-incident-power side of the middle hysteresis.

region from 8.1 to $8.67 \delta L$. Here, optical signals experience two hystereses in their transmitted power, as shown in Fig. 4.16 for $\delta L = 8.4$. This behavior has interesting applications as a three-level optical memory, or optical switch. We expect that a prudent choice of device parameters (e.g., spatial chirp C , coupling coefficient κ) will bring the switching powers of both bistable regions closer, for practical device operation.

For large amounts of linear spatial chirp, resonances away from the photonic bandgap can become strong enough that they exhibit the lowest lasing threshold [75]. This behavior is shown in Fig. 4.17 for $|C| = 15$ for a value of $g_0 L = 2.74$, equivalent to 98% of the lasing threshold. Under such conditions, the inner resonances are unable to provide 30-dB amplification. Hence, the outer resonances should be used for high-gain optical switching. As stated above, from a computational perspective, *any* value of $g_0 L$ can be used in calculations, but only one that lies below lasing

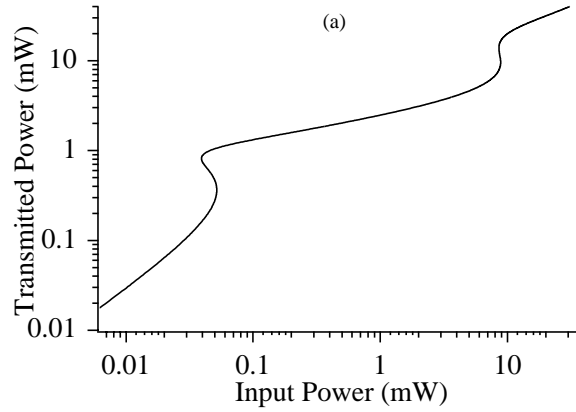


Figure 4.16: Double bistability occurring for a large chirp value of $C = -10$.

threshold is physically valid for our model. Thus, care must be taken during the study and design of chirped-grating DFB SOAs to track the lasing threshold.

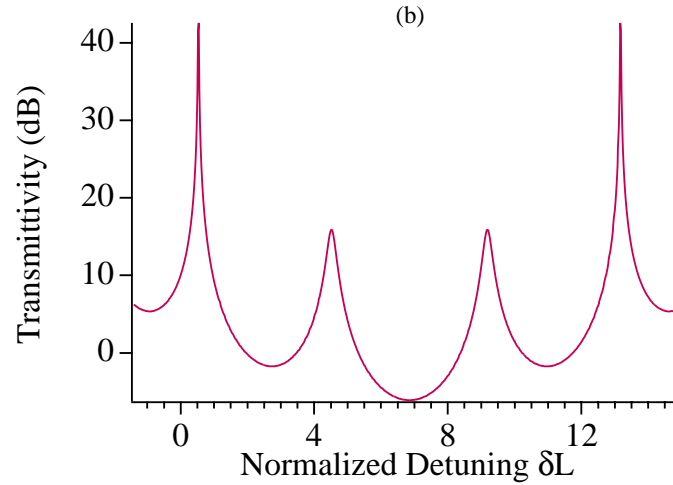


Figure 4.17: Transmission through a DFB SOA with $|C| = 15$ driven at 98% of its lasing threshold, exhibiting strong secondary resonances.

4.4 Conclusion

In this chapter, we investigated the effects of grating nonuniformities on the bistable performance of DFB SOAs. Our analysis extended the transfer-matrix method dis-

cussed in Chapter 3 to account for grating nonuniformities such as phase shifts, spatial chirp, and amplitude taper. In particular, we found that spatial chirp can increase both the spectral range of low-power switching and the spectral uniformity. To find this improvement, we considered switching on both sides of the photonic bandgap, and in both directions along the linearly chirped device; we predicted that the largest improvement occurs for reflected signals incident along the N-direction (the direction of increasing grating period), on the long-wavelength side of the photonic bandgap. This conclusion is based on reasonable values of the device parameters, and on considering switching powers below 0.1 mW.

A total linear variation of about 0.24% ($|C| = 10$) increased the spectral range of switching by 2.7 times to a range of $1.37 \delta L$. For a 300- μm -long device operating near 1.55 μm , this spectral range is 0.5 nm (62 GHz), as opposed to 0.19 nm (23 GHz) for an unchirped device. Furthermore, over a spectral range of 12.5 GHz, the bistable hysteresis exhibited a small variation in the output powers of the upper branch of the hysteresis curve, a clear separation of upper and lower output-power branches, and a region of common input powers. Taking the application of optical memory as an example, the common input-power region allows flexible alignment of the holding beam, which must fall between the switching thresholds of the hysteresis curve. Moreover, the clear separation of upper and lower output-power branches of the hysteresis curve allows the on-state and off-state to be well defined over the 12.5-GHz spectral range.

Spatial chirp also had a dramatic effect on the shape of the hysteresis curve on reflection. The inverted-S and loop shapes discussed in Chapter 3 can either be eliminated *or* enhanced, depending on the direction of incidence of the signal and depending on which side of the photonic bandgap the signal falls. In particular, for signals travelling in the P-direction on the long-wavelength side of the photonic bandgap, the reflectivity resonance pushed toward zero reflectivity during the bistable switching process. For a chirp parameter of $|C| = 5$, this resulted in an on-off switching

ratio of at least 30 over a range of 27 GHz, with the maximum switching ratio exceeding $10^5:1$.

Chapter 5

Optical Bistability: Time-Dependent Analysis

5.1 Introduction

The steady-state model for bistability in DFB SOAs developed in Chapters 3 and 4 is useful for studying many aspects of bistability, such as the spectral range, spectral uniformity, shape of hysteresis curves, and dependence on grating nonuniformities. We now shift our focus to the temporal behavior of optical bistability. In this chapter, we develop a simple model of the bistable system that serves as the basis for simulating all-optical processing in Chapter 6. We also compare results with the steady-state model, and discuss the change in the shape of the hysteresis curve resulting from fast input-power modulation.

5.2 Time-Dependent Model

The time-dependent behavior of dispersive bistability in DFB SOAs can be studied with the coupled-mode equations (2.43) and (2.44) for the bistable signal and the gain rate equation (2.52) that embodies the SOA carrier dynamics. This system of nonlinear, coupled, partial differential equations can be greatly simplified, while retaining insightful solutions, by applying some approximations common to the study

of optical bistability; namely, the mean-field approximation [10], [78], the uniform-gain approximation [43], and the adiabatic elimination of the optical signal [36], [43]. A model using these approximations has been previously presented for DFB SOAs [43], and used to study pulses that undergo bistable switching. In this section, we apply these approximations to our form of the governing equations given in Chapter 2.

The gain rate equation (2.52) can be simplified by assuming that the *average* value of the optical power is sufficient to calculate the saturated gain [12], [43]. This is a sensible approximation for a uniform-grating DFB SOA because the summed intensity of the coupled modes can result in a nearly uniform saturated-gain distribution [43]. (Such an approximation was avoided in the steady-state model since it was used to study nonuniform gratings.) Using the mean power, and assuming a uniform steady-state gain g_0 , the gain g itself no longer varies along the amplifier. An equation for the uniform gain can be derived by averaging the rate equation (2.52) over the length of the amplifier L :

$$\tau \frac{d\langle g \rangle}{dt} = g_0 - \left[1 + \frac{\langle P_A \rangle + \langle P_B \rangle}{P_{\text{sat}}} \right] \langle g \rangle, \quad (5.1)$$

where the angled brackets indicate longitudinal averaging. For the final term, we have factored the average of the gain–power products into the average of their arguments; such a factoring scheme (of the field and medium response) has been referred to as the mean-field approximation [78].

The powers P_A and P_B [defined in Eq. (2.53)] found in Eq. (5.1) are obtained from the coupled-mode equations (2.43) and (2.44); analytic solutions to these equations are possible if we apply some common assumptions. Under the approximation that the average power is sufficient to calculate the gain (as discussed above), the gain becomes uniform along the amplifier, and thus we may use its average value $\langle g \rangle$ in the coupled mode equations [12], [43].

To further simplify the coupled-mode equations, we assume that the field envelopes A and B adjust instantaneously to changes in the SOA gain [36], [43]. The optical fields therefore attain their steady state quickly, allowing the time derivatives to drop in Eqs. (2.43) and (2.44). The bistable system dynamics are hence determined solely by the gain rate equation (5.1). This adiabatic approximation is valid when the unobstructed signal-transit time ($L/v_g \approx 0.003$ ns) through the amplifier is much shorter than the carrier lifetime ($\tau \approx 0.2 - 1$ ns), and shorter than the rise and fall of the input-field envelope $h(t)$.

Under the adiabatic and uniform-gain approximations, the coupled-mode equations (2.43) and (2.44) become ordinary differential equations (of independent variable z) with constant coefficients. The general solutions for the counterpropagating fields, as given by Eqs. (2.64) and (2.65), are

$$A(z) = A_1 \exp(i\gamma z) + r B_2 \exp(-i\gamma z), \quad (5.2)$$

$$B(z) = r A_1 \exp(i\gamma z) + B_2 \exp(-i\gamma z), \quad (5.3)$$

where

$$r = (\gamma - \Delta)/\kappa, \quad (5.4)$$

$$\gamma = \sqrt{\Delta^2 - \kappa^2}, \quad (5.5)$$

$$\Delta = \delta - i \frac{\langle g \rangle}{2} (1 - i\alpha) + i \frac{\alpha_{int}}{2}. \quad (5.6)$$

Applying the boundary conditions of an input-field envelope $h(t)$ at one facet, i.e., $A(z = -L/2, t) = h(t)$ and $B(z = L/2, t) = 0$, and assuming that anti-reflection

(AR) coatings nullify the facet reflections, the counterpropagating field envelopes are

$$A = h \frac{\gamma \cos(\gamma \xi) + i \Delta \sin(\gamma \xi)}{\gamma \cos(\gamma L) - i \Delta \sin(\gamma L)}, \quad (5.7)$$

$$B = h \frac{i \kappa \sin(\gamma \xi)}{\gamma \cos(\gamma L) - i \Delta \sin(\gamma L)}, \quad (5.8)$$

where $\xi = z - L/2$.

Using the field envelopes (5.7) and (5.8), the optical powers P_A and P_B are

$$P_A = P_0 \zeta [\cosh(2\gamma_i \xi) \theta_1 - \sinh(2\gamma_i \xi) \theta_2 + \cos(2\gamma_r \xi) \theta_3 - \sin(2\gamma_r \xi) \theta_4], \quad (5.9)$$

$$P_B = P_0 \zeta |\kappa|^2 [\cosh(2\gamma_i \xi) - \cos(2\gamma_r \xi)], \quad (5.10)$$

where $P_0(t) = |h(t)|^2 \sigma$ is the input power, $\gamma = \gamma_r + i\gamma_i$, and

$$\theta_1 = \gamma \gamma^* + \Delta \Delta^*, \quad (5.11)$$

$$\theta_2 = \gamma \Delta^* + \gamma^* \Delta, \quad (5.12)$$

$$\theta_3 = \gamma \gamma^* - \Delta \Delta^*, \quad (5.13)$$

$$\theta_4 = i(\gamma \Delta^* - \gamma^* \Delta), \quad (5.14)$$

$$\zeta = [\cosh(2\gamma_i L) \theta_1 + \sinh(2\gamma_i L) \theta_2 + \cos(2\gamma_r L) \theta_3 + \sin(2\gamma_r L) \theta_4]^{-1} \quad (5.15)$$

To obtain the average power within the SOA, the solutions (5.9) and (5.10) are integrated over the device length L to yield:

$$\begin{aligned} \langle P_A \rangle &= P_0 \zeta \left\{ \frac{\sinh(2\gamma_i L) \theta_1 + [\cosh(2\gamma_i L) - 1] \theta_2}{2\gamma_i L} + \frac{\sin(2\gamma_r L) \theta_3 + [1 - \cos(2\gamma_r L)] \theta_4}{2\gamma_r L} \right\}, \\ \langle P_B \rangle &= P_0 \zeta |\kappa|^2 \left[\frac{\sinh(2\gamma_i L)}{2\gamma_i L} - \frac{\sin(2\gamma_r L)}{2\gamma_r L} \right]. \end{aligned}$$

Substituting these expressions for the average powers into the gain rate equation (5.1) adiabatically eliminates the internal optical powers; the resulting ordinary differential

equation has only a single dependent variable, $\langle g \rangle$, and is relatively simple to solve numerically. For the simulations shown here, we solve the equation using a variable-order technique and limit the estimated numerical error to 0.1% for each integration step. Once the average gain $\langle g \rangle$ is calculated for all time, the solution vector can be used to obtain the bistable output power.

Analytic expressions for the bistable transmitted power $T(t) = P_A(z = L/2, t)$ and reflected power $R(t) = P_B(z = -L/2, t)$ can be found using Eqs. (5.9) and (5.10), respectively:

$$T = P_0 \zeta 2(\gamma_r^2 + \gamma_i^2), \quad (5.16)$$

$$R = P_0 \zeta |\kappa|^2 [\cosh(2\gamma_i L) - \cos(2\gamma_r L)]. \quad (5.17)$$

An example using the transmitted-power expression (5.16) is shown in Fig. 5.1. To trace out the hysteresis, we used a sinusoidal input power $P_0(t) = p[1 - \cos(2\pi t/T_m)]$, where $p = 0.6$ mW is the input amplitude and $T_m = 10^6 \tau$ is the modulation period. A slow period was chosen to simulate steady-state behavior; the correspondingly large integration step size $\Delta t = 100\tau$ skips over transient behavior at the switching thresholds, which is addressed in the following section.

By plotting the input–output transfer function (i.e., P_0 vs. T), as shown in Fig. 5.1(a), explicit time dependence naturally drops. The dynamic hysteresis, unlike the steady-state case, can be decomposed into its time-dependent components, as shown in Fig. 5.1(b). Hysteresis is apparent in the decomposed input and output pulses — the switch off power is different from the switch on power because the system is affected by its past state. When we use the term “hysteresis” for the steady-state solutions calculated in Chapters 3 and 4, we have in mind the behavior produced by the time-dependent model.

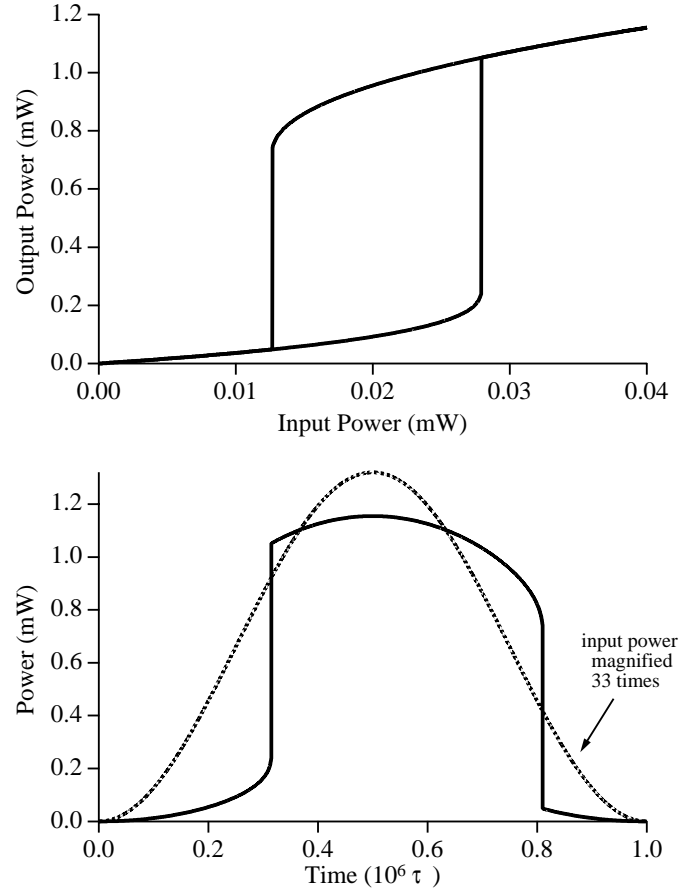


Figure 5.1: (a) Bistable hysteresis curve on transmission using the time-dependent model. (b) Input and transmitted powers plotted as a function of time.

5.3 Hysteresis

Using a long modulation period of $T_m = 10^6 \tau$, we compare solutions from the time-dependent and steady-state models for reflective bistability on the short-wavelength side of the photonic bandgap in Fig. 5.2. The switching powers for the time-dependent case are higher — the whole hysteresis curve is shifted toward higher powers. The upward-switching thresholds are about 16% greater for the two smallest values of the normalized detuning δL , whereas the downward-switching thresholds are nearly 50% greater. This increase may be an error resulting from using the

average-power distribution to calculate the saturated gain. Such an approximation was found to result in larger switching-threshold powers (by 15 %) in bistable Fabry-Perot SOAs [13].

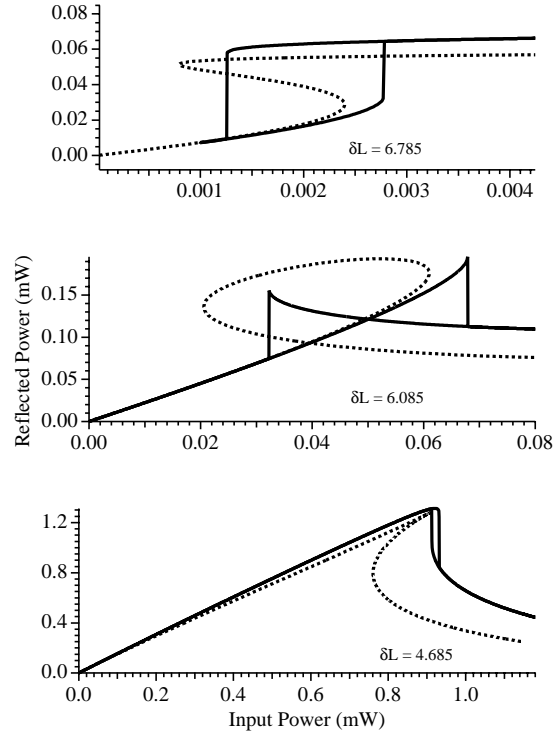


Figure 5.2: Comparison of reflective hystereses from steady-state (dashed lines) and time-dependent models.

Although the switching thresholds generated by each model are different, the switching behavior of each hysteresis curve is qualitatively the same; the time-dependent model faithfully produces even the loop-shaped and inverted-S-shaped hysteresis curves. We therefore expect the simple dynamic model to provide qualitatively accurate solutions in general.

To create a hysteresis curve using the time-dependent model, an input-power, time-dependent waveform is first used as an initial condition to calculate an output-power waveform. The output solution represents *actual* power levels achieved by the

signal. Thus, upon creating the input–output transfer function, the unstable branch, which is apparent in the steady-state solution, does not occur.

The switching thresholds of the hysteresis curve begin to vary as the modulation period T_m is decreased, as shown in Fig. 5.3 for $T_m/\tau = 10^6, 10^4, 10^2, 10^0$, and 10^{-2} . As the modulation period is decreased, the power required for upward switching increases. Even at $T_m/\tau = 10^4$, the switching threshold is 5% greater than for $T_m/\tau = 10^6$; for $T_m/\tau = 10^0$, the upward switching power has increased by over 2000%. As the modulation period is decreased, the downward-switching threshold shifts to lower powers and the hard switching edge smooths off to a gradual slope. Eventually (at $T_m/\tau \simeq 10^{-1}$) the downward-switching transition is so smooth that threshold powers are difficult to define.

For modulation periods of $T_m/\tau = 10^4, 10^2$, and 10^0 , spiking occurs during upward switching. For these cases, the time step Δt used in numerical calculations (defined as $\Delta t/T_m = 10^{-4}$) is equal or less than τ . Spiking behavior of this sort is common in simulations of dispersive bistability in resonant-type SOAs [23], [36], [43], and occurs as the optical signal passes through the peak of the Bragg resonance [43], [45]. The peak of the spike is enhanced in simulations as an artifact from the adiabatic elimination of the bistable signal from the system dynamics [23].

For short modulation periods beginning at 0.4τ , spiking does not occur, and the hysteresis curve is shaped like an oblong loop. As the period is decreased further, the loop closes down, and eventually becomes a line, as seen for $T_m/\tau = 10^{-2}$ in Fig. 5.3. This closing down behavior at short modulation periods was first noted by Westlake et al. [37] for bistability in Fabry–Perot SOAs, where the hysteresis closed down at $T_m \simeq 2\tau$.

The closing down of the bistable curve suggests that the hysteretic response of the DFB SOA cannot be used for optical memory at repetition rates faster than the inverse of the carrier lifetime τ [37], [36]. However, the slow repetition rate of memory does

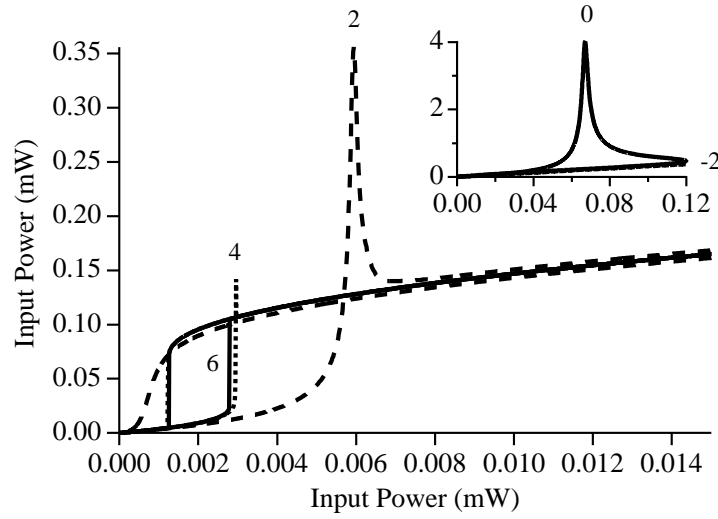


Figure 5.3: Dependence of the hysteresis curve on the modulation period $T_m = 10^x$, where the integers near the peaks are the values of x .

not prevent such devices from finding applications in high-speed communications, as shown in the following chapter.

5.4 Conclusion

In this chapter, we developed a time-dependent model of the bistable DFB SOA system. We arrived at a simple model by adiabatic elimination the optical signal in the governing equations, and by assuming that the average power in the SOA is sufficient to determine the saturated gain. We found that this model yields higher switching-threshold powers than those obtained from the steady-state model (which did not use an average power), but that the shapes of the hysteresis curves qualitatively agree for long signal-modulation periods. For modulation periods approaching the carrier lifetime τ , the hysteresis shape changed dramatically, and new features such as spiking and closing down of the hysteresis curve became prominent. Despite these features, the hysteretic nature of optical bistability in DFB SOAs is useful for high-speed memory applications, as shown in the following chapter.

Chapter 6

All-Optical Flip–Flop

6.1 Introduction

All-optical techniques for processing lightwave-communication signals have advanced considerably in recent years. Intensive research has produced practical all-optical devices for tasks such as data-wavelength conversion [6], regeneration [79], and demultiplexing [80]. In an analogy to electronics, these devices exhibit *combinational* logic [81] — i.e., the output is determined by the existing state of the input signals. Using the example of data-wavelength conversion, the output power at the converted wavelength changes in response to the input data of the original wavelength; as the input signal subsides, the converted power returns to its initial state, thus replicating the data.

Digital signal processing in electronic systems makes use of combinational and *sequential* logic [81]. The output signal from devices exhibiting sequential logic is determined by the existing state of input signals *and* the state of past input signals — it exhibits memory. The basic building block of sequential processing in electrical systems is called a flip–flop [81], which exhibits bistability and is controlled by auxiliary signals.

In an attempt to bring the advantages of sequential processing to the optical layer (i.e., for optical signals, without electronic conversion), optical bistability has been

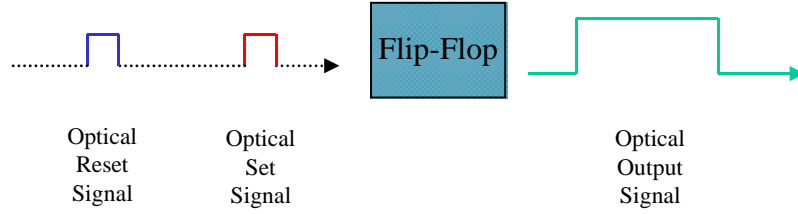


Figure 6.1: All-optical flip–flop. Optical output is controlled by optical input signals.

investigated as a means of realizing an all-optical flip–flop [23], [30], [82], [83]. The basic idea of an all-optical flip–flop is represented in Fig. 6.1; a bistable, latchable output power is controlled by optical signals. Early work on optical bistability was motivated, in part, by the possibility of optical computing, in which arrays of optical flip–flops would be used for processing. However, recall that the number density of SOA devices is limited by heat dissipation (as discussed in Section 1.2), thereby making SOA-based large-scale processing inferior to electronic processing. Here, we bypass this limitation for optical processing by investigating applications to fiber-optic communications in which even a single flip–flop is useful.

All-optical flip–flop operation has been demonstrated using Fabry–Perot SOAs by Ogasawara et al. [23] and by Inoue [30]. Set and reset were performed in their experiments by either by varying the holding-beam input power (set: [23], [30]; reset: using a ‘negative’ optical pulse [23]), or by modulating the holding beam via a closely tuned (0.008 nm) auxiliary signal (reset: [30]). Thus, these control techniques have a very limited wavelength range.

In this chapter, we present new optical-control techniques to set and reset a resonant-type SOA-based optical flip–flop using control signals that exhibit a very wide wavelength range of operation. We begin by discussing a commonly referenced control technique based on varying the holding-beam input power [23]. Then, we dis-

cuss the physical mechanism of our control technique (that does *not* rely on changing the holding-beam input power) and simulate its operation. All-optical flip–flop operation is achieved using the experimental system described in the following section. We then investigate different aspects of flip–flop performance, such as polarization and power requirements, to gauge the practicality for lightwave systems. We close the chapter by considering an application of such a device — data-format conversion from high-speed RZ signals to low-speed NRZ signals.

6.2 Principle of Operation

6.2.1 Control using Holding Beam

The two output states of an optical flip–flop based on optical bistability in a resonant-type SOA are simply where the signal’s input power P_0 intersects the two branches of the hysteresis curve, as shown in Fig. 6.2 at $P_0 = P_H$. The output power of the signal can be set and reset between P_{on} and P_{off} by varying P_0 through the upward and downward switching thresholds, respectively [23]; we discuss and simulate this process to introduce key concepts and to facilitate comparison with our new control techniques.

The input power P_0 is initially located between the switching thresholds, like P_H in Fig. 6.2. Optical set can be performed by increasing the input power beyond the upward switching threshold [23], [30], and can be understood as follows. An increase in optical power within the SOA stimulates recombination of electron-hole pairs (i.e. gain saturation), which increases the refractive index; the signal thereby increases its own wavenumber and optical phase. This self-phase modulation (SPM) shifts the photonic bandgap and Bragg resonances to longer wavelengths. As a Bragg resonance moves onto the signal wavelength, the internal optical power increases even more. Bistable upward switching occurs when a positive feedback loop (between the

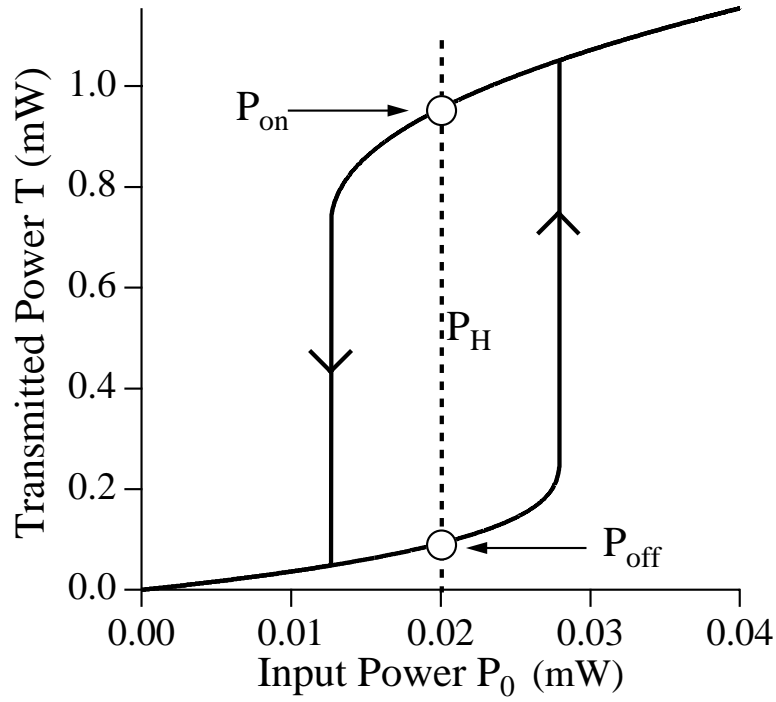


Figure 6.2: Flip-flop output states. Two stable transmission states, P_{on} and P_{off} , occur for a single input power P_H .

internal optical power, nonlinear refractive index, and Bragg resonance) causes the Bragg resonance to shift through the signal wavelength, providing resonant amplification for the signal. Set operation is shown in Fig. 6.3, where we have used the time-dependent model developed in Chapter 5. This input power is given by

$$P_0 = P_H[1 + 0.5f(t - t_1) - 0.5f(t - t_2)], \quad (6.1)$$

where the perturbation $f(t - t_x)$ to the average input power P_H is given by

$$f(t - t_x) = \exp\{ -[(t - t_x)/W_f]^{2M} \}, \quad (6.2)$$

and the parameter values are given in Table 6.1.

The signal's output power remains at a high level P_{on} (corresponding to the upper

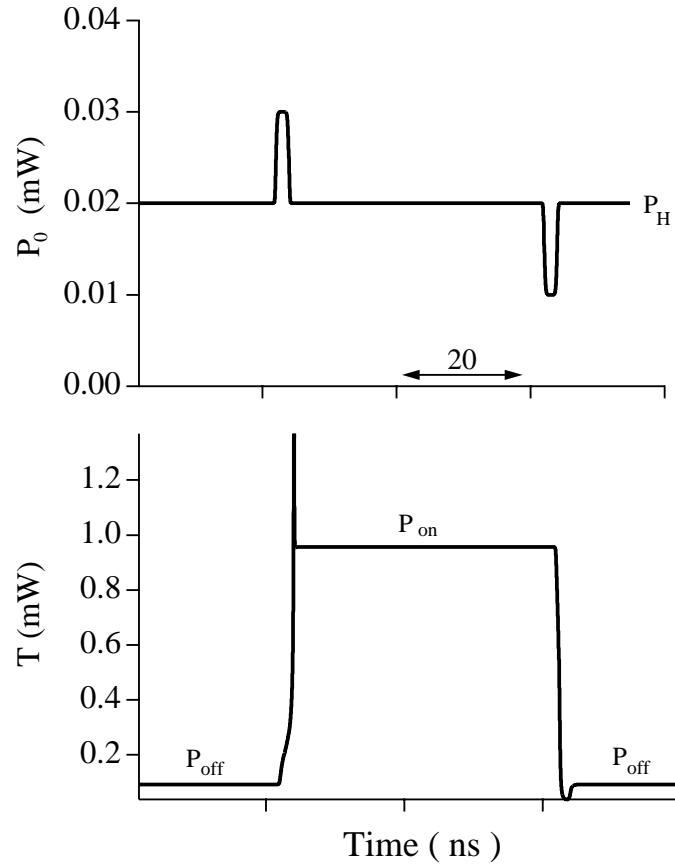


Figure 6.3: Flip–flop operation based on the holding beam. (a) The holding-beam input power P_0 is varied beyond the switching thresholds to (b) set and reset the bistable transmission T .

hysteresis branch) even after its input power returns to the initial state P_H , as shown in Fig. 6.3. Although the bistable signal provides the same input power, the larger output is achieved because the new Bragg-resonance location provides resonant amplification. The relatively larger optical power within the SOA, in turn, maintains the amount of carrier-density depletion required to hold the Bragg resonance in place. The latching occurs on the short-wavelength slope of the Bragg resonance, which (unlike the long-wavelength slope) is stable if perturbed; for example, a momentary increase in the input power will increase the refractive index and shift the resonance

Table 6.1: Parameter values for flip–flop control via holding beam.

Quantity	Symbol	Value
Mean input power	P_H	0.02 mW
Carrier lifetime	τ	0.2 ns
Set pulse center	t_1	23 ns
Reset pulse center	t_2	63 ns
Integration step size	Δt	2 ps

away from the holding-beam wavelength, resulting in a reduction of power and moving the resonance back to its original location.

The flip–flop is reset by decreasing the input power of the holding beam beyond the downward switching threshold of the hysteresis curve. The resulting decrease in the internal optical power allows the carrier density to recover, thereby *decreasing* the refractive index. SPM shifts the Bragg resonance to shorter wavelengths and back toward the holding-beam wavelength. As the resonance peak passes the signal wavelength, a positive feedback loop (acting in the opposite manner as for upward switching) shifts the Bragg resonance to even shorter wavelengths and lowers the output power to P_{off} . In terms of the input power P_0 , reset is achieved by the application of a ‘negative’ optical pulse [23], as shown in Fig. 6.3.

Using the input and output powers of Fig. 6.3 to assemble a nonlinear transfer function, we find the interesting hysteresis-curve shape shown in Fig. 6.4 (solid lines). The largest features of Fig. 6.4 correspond to the relatively narrow spikes of Fig. 6.3. Likewise, the long time interval of the ‘on’ state in Fig. 6.3 is condensed to a point on the hysteresis curve of Fig. 6.4; the time aspect of the input and output fields is lost in the bistable hysteresis curve.

Moreover, the new hysteresis curve does not closely resemble the ‘ordinary’ hysteresis curve of Fig. 6.2, calculated using a slowly varying sinusoidal signal, and shown with dotted lines in Fig. 6.4. Although the actual shape of the hysteresis curve

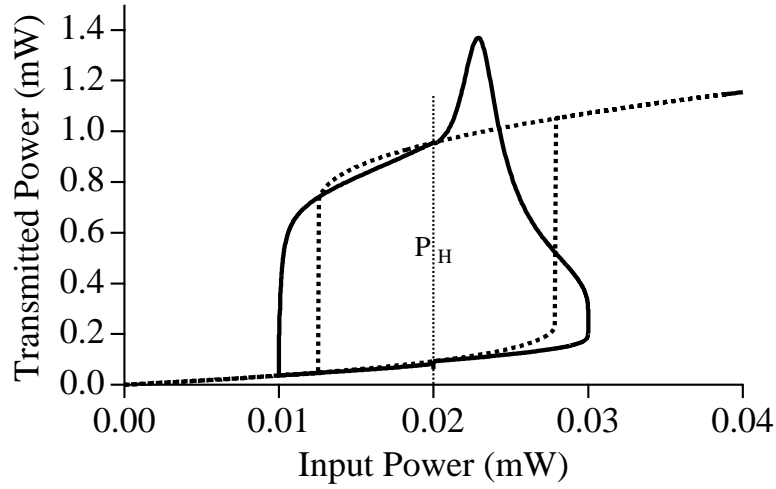


Figure 6.4: Transfer functions for the flip-flop operation shown in Fig. 6.3 (solid lines) and the slowly modulated hysteresis curve of Fig. 6.2 (dotted lines).

depends on the modulation rate and peak power of input signal, the locations corresponding to ‘on’ and ‘off’ states are the same for both curves shown in Fig. 6.4. Thus, the initial figure 6.2 is justified, since its purpose was to show the existence of two stable states corresponding to a single input power P_H ; long modulation period T_m was selected to produce a familiar-looking shape.

6.2.2 Control using Auxiliary Signals

For the flip-flop operation described in the previous section, the holding beam provides the power used to latch the flip-flop *and* initiates set and reset via SPM. We seek to relegate the control functionality to auxiliary optical signals. Separating holding and control functionality is advantageous because the holding-beam source can then be optimized solely for wavelength and power stability. Furthermore, set and reset can then be performed directly by signals from an optical network. Such a system is depicted in Fig. 6.1, where the box labelled “Flip-Flop” contains the bistable system comprised of the holding beam and DFB SOA. Ideally, set and reset can be performed over a wide wavelength range; hence, control signals can come from a va-

riety of wavelength channels in modern-day wavelength division multiplexed (WDM) systems, where the channel spacing is ~ 0.8 nm.

The general principle we use to relegate control to auxiliary signals is to replace the holding-beam self-phase modulation (SPM) discussed in Section 6.2.2 with auxiliary-signal *cross*-phase modulation (XPM). The set signal, like the holding beam, falls within the SOA gain spectrum and hence stimulates recombination of electron-hole pairs. Recombination causes gain saturation and an increase in the refractive index even *at the holding-beam wavelength*. Thus, the set signal modulates the wavenumber and phase of the holding beam; this kind of XPM has been used in other geometries and applications, including data-wavelength conversion in SOA-integrated Mach-Zehnder interferometers [89], as well as clock recovery and clock division in nonlinear optical loop mirrors [61].

For our application, the increase in refractive index pushes the photonic bandgap and Bragg resonances to longer wavelengths. Upward switching occurs when the Bragg resonance has been shifted at least enough to seed the positive feedback loop for upward bistable switching. In terms of the hysteresis curve, using XPM to shift the Bragg resonance toward the holding-beam wavelength corresponds to pushing the switching thresholds to lower powers. Switching occurs once the upward-switching threshold has been brought to the holding-beam input power P_H , as depicted in Fig. 6.5.

After the set pulse passes through the SOA, the hysteresis curve returns to its initial shape, but now the output power falls on the higher branch at P_{on} , as depicted in Fig. 6.5. The post-switching location of the Bragg resonance provides resonant amplification of the holding beam, resulting in a larger output power and sufficient internal power to lock the resonance in place, as described in Section 6.2.1.

The flip-flop is reset by pushing the hysteresis curve to higher powers, allowing the downward-switching threshold to reach the holding-beam input power, as depicted in Fig. 6.6. The hysteresis curve can be shifted in this way by signals that are

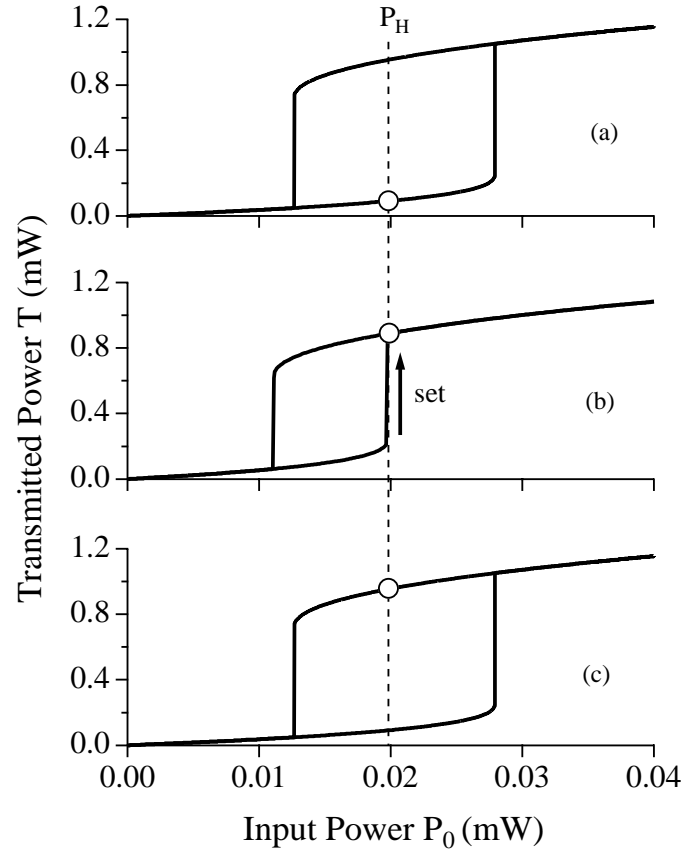


Figure 6.5: XPM-based set. (a) The transmitted power (indicated by the circle) is initially low for a fixed input power P_H . (b) XPM ($+\Delta\phi$) caused by a set signal pushes the hysteresis curve to smaller powers, thereby switching the transmission to a higher power. (c) After the set signal passes, the hysteresis curve relaxes to its initial shape, with the transmitted-power state on the higher hysteresis branch.

absorbed by the SOA, giving their energy to electrons that are then excited into the semiconductor conduction band. This gain pumping is accompanied by a *decrease* in the refractive index and optical phase at the holding-beam wavelength. As the refractive index decreases, the Bragg resonance shifts to shorter wavelengths; reset occurs when the Bragg resonance shifts enough to cause the positive feedback loop that results in downward bistable switching.

XPM-based reset is qualitatively different from the SPM-based reset in that the former increases the carrier density directly by the application of optical power (i.e.,

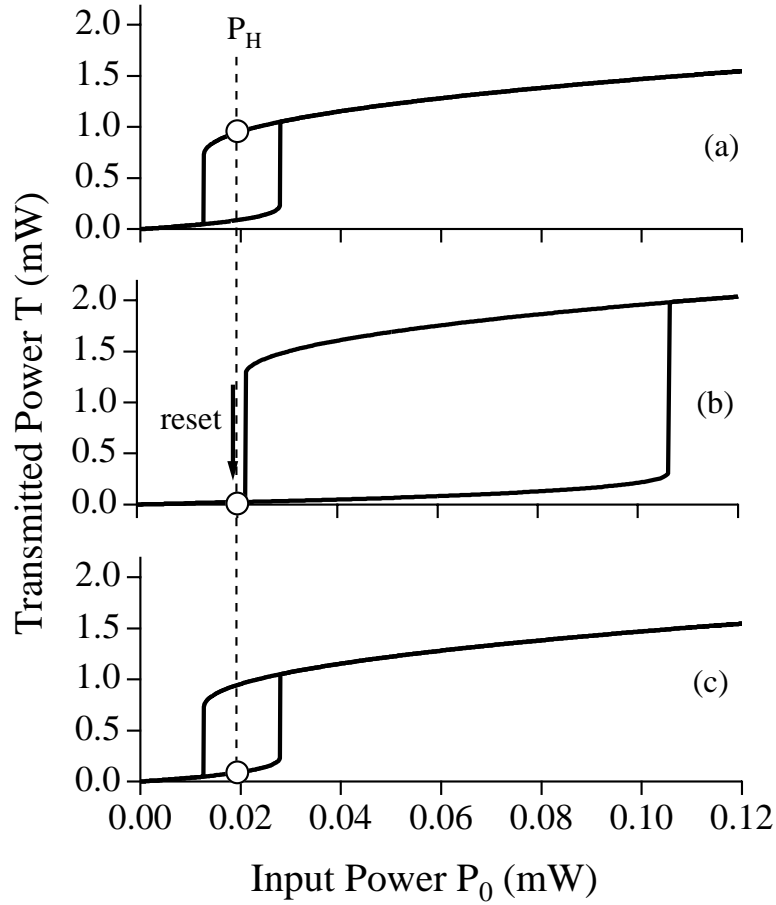


Figure 6.6: XPM-based reset. (a) High initial transmitted power (indicated by the circle). (b) XPM ($-\Delta\phi$) caused by a reset signal pushes the hysteresis curve to larger powers, and the transmitted power drops to the lower hysteresis branch. (c) After the reset pulse passes, the hysteresis curve relaxes to initial shape, and transmission remains at the lower power.

a ‘positive’ optical pulse). For SPM-based reset, on the other hand, the carrier density increases through the natural recovery of the SOA gain as the internal power of the holding beam is reduced. This internal power can be reduced either by using a negative optical pulse (as shown in Fig. 6.3) [23], or by interfering the holding beam with a closely tuned auxiliary signal [30]. The interfering-signal technique shifts the bistable switching thresholds to higher powers while the holding-beam input power is constant and can be achieved at relatively low reset-beam powers, but requires a close matching between the holding and reset wavelengths of about 0.008 nm. The

XPM-based reset technique, on the other hand, can be achieved over a wide wavelength range (> 160 nm), but requires higher powers (> 0.7 mW) [85], as will be described in Section 6.4.

Our goal in modeling the XPM set–reset techniques is to show hysteresis-curve shifting and ultimately flip–flop operation by incorporating the control signals in a simple, phenomenological manner. The set \vec{E}_S and reset \vec{E}_R fields pass through the DFB SOA without interacting with the index grating, and can be expressed as

$$\vec{E}_S(x, y, z, t) = \text{Re}\{\hat{e}F(x, y)S(z, t)\exp(i\beta_S z)\exp(-i\omega_S t)\}, \quad (6.3)$$

$$\vec{E}_R(x, y, z, t) = \text{Re}\{\hat{e}F(x, y)R(z, t)\exp(i\beta_R z)\exp(-i\omega_R t)\}. \quad (6.4)$$

The polarization vector \hat{e} and the transverse field $F(x, y)$ are assumed to be the same as those of the holding beam, S and R are the slowly varying field envelopes, and β_S and β_R are the wavenumbers. The set-signal optical frequency ω_S falls within the SOA gain curve, and the reset-signal frequency ω_R falls outside of the gain curve, on the higher-frequency side.

The control signals affect the bistable output power of the holding beam by changing the SOA carrier density; we account for these signals by expanding the rate equation (2.48) as follows

$$-D\nabla^2 N + \frac{\partial N}{\partial t} = \frac{J}{ed} - \frac{N}{\tau} - a(N - N_0)\frac{I}{\hbar\omega} - a(N - N_0)\frac{I_S}{\hbar\omega_S} + \eta\frac{I_R}{\hbar\omega_R}. \quad (6.5)$$

The first three terms on the right hand side are found in the rate equation (2.48) of Section 2.3. The penultimate term accounts for stimulated recombination of electron-hole pairs by the set signal having an intensity I_S . The final term accounts for the reset signal, having an intensity I_R , and η characterizes its absorption by the valence-band electrons.

The set-signal term within the rate equation (6.5) is functionally similar to the

holding-beam term, both of which deplete the carrier density. In general, the amount of gain experienced by these signals will depend on their detuning from the SOA gain peak, the spectral location of which shifts with changes in the carrier density. We ignore these gain-curve dependent effects because we do not expect them to significantly alter the flip–flop behavior.

Interference terms produced by the set signal were also dropped. Nonlinear frequency mixing is not appreciable from the sub-milliwatt input powers used in experiments. In addition, we have avoided a close detuning (0.008 nm) between the set signal and holding beam in our experiments which can reset the flip–flop (as discussed in Section 6.2.1). Spatial interference was neglected because carrier diffusion is assumed to smooth out the longitudinal spatial holes.

To account for carrier generation by the reset signal, we consider the SOA to be an ideal four-level system. The reset-signal photons are absorbed by electrons occupying the 1st level (bottom of the valence band). These electrons jump to the fourth level (top of the conduction band), where they quickly relax (< 1 ps) to the 3rd level (bottom of conduction band) and become part of the carrier density N . Thus, the absorbed photon flux $\eta I / (\hbar\omega_R)$ in Eq. (6.5) represents a transfer of energy from the reset signal to the carrier density. To simplify our study, we assume that this energy-transfer process has perfect efficiency, and we ignore the depletion of the ground-state electrons (i.e., η is constant). The increase in gain due to the reset-signal term in the gain rate equation resembles J/ed , which accounts for the electrical injection of carriers.

We simplify the carrier-density rate equation (6.5) in the same manner as discussed in Chapter 5 for Eq. (2.48). Averaging over the transverse dimensions of the active region introduces the optical confinement factor Γ and the mode cross section σ ; since the transverse-mode profile $F(x, y)$ is assumed to be the same for the holding beam and the control fields, the confinement factor Γ and mode cross section σ are also identical. We also assume that the average optical power is sufficient to cal-

culate the carrier density, and invoke the mean-field approximation. Using the gain expression (2.47), the resulting gain rate equation is

$$\tau \frac{d\langle g \rangle}{dt} = g_0 + \eta \frac{\langle P_R \rangle}{P_{\text{Rsat}}} - \left[1 + \frac{\langle P_A \rangle + \langle P_B \rangle}{P_{\text{sat}}} + \frac{\langle P_S \rangle}{P_{\text{Ssat}}} \right] \langle g \rangle, \quad (6.6)$$

where $P_S = |S|^2 \sigma$, $P_R = |R|^2 \sigma$, $\eta = \Gamma \eta_m$, $P_{\text{Ssat}} = \hbar \omega_S W d / (\tau a \Gamma)$, and $P_{\text{Rsat}} = \hbar \omega_R W d / (\tau a \Gamma)$.

The control-signal powers P_S and P_R can be obtained from the following propagation equations

$$\frac{\partial P_S}{\partial z} + \frac{1}{v_S} \frac{\partial P_S}{\partial t} = g P_S, \quad (6.7)$$

$$\frac{\partial P_R}{\partial z} + \frac{1}{v_R} \frac{\partial P_R}{\partial t} = -\eta P_R, \quad (6.8)$$

where v_S and v_R are the group velocities for the set and reset signals, respectively. As in Chapter 5, we assume that the SOA responds to the average of the signal powers, which allows the modal gain g to be replaced by its average value $\langle g \rangle$. This is a more severe approximation for the control signals than for the holding beam because the former do not scatter off of the grating and therefore have an exponential variation in z . Nonetheless, eliminating the z dependence of such travelling-wave signals is a common simplification for the study of nonlinear phenomena in SOAs [61], and is especially suitable for a qualitative analysis and for a small gain-length product.

The propagation equations (6.7) and (6.8) can be further simplified by assuming that the control signals respond instantaneously to changes in the carrier density. As discussed for the holding signal, this adiabatic approximation is valid when the transit time ($L/v_x \approx 0.003$ ns) through the amplifier is much shorter than the carrier lifetime ($\tau \approx 0.2$ – 1 ns), and shorter than the rise and fall of the input-field envelopes. Under

these approximations, the control-signal equations become

$$\frac{dP_S}{dz} = \langle g \rangle P_S, \quad (6.9)$$

$$\frac{dP_R}{dz} = -\eta P_R. \quad (6.10)$$

Applying the boundary conditions $P_S(z = -L/2, t) = P_{S0}(t)$ and $P_R(z = -L/2, t) = P_{R0}(t)$, the solutions to Eqs. (6.9) and (6.10) give the control-signal distributions along the amplifier:

$$P_S = P_{S0} \exp \left[g \left(z + \frac{L}{2} \right) \right], \quad (6.11)$$

$$P_R = P_{R0} \exp \left[-\eta \left(z + \frac{L}{2} \right) \right]. \quad (6.12)$$

Integrating Eqs. (6.11) and (6.12) over the length of the amplifier, we obtain

$$\langle P_S \rangle = P_{S0} \frac{\exp(gL) - 1}{gL}, \quad (6.13)$$

$$\langle P_R \rangle = P_{R0} \frac{1 - \exp(-\eta L)}{\eta L}. \quad (6.14)$$

A short control pulse (e.g., ~ 8 ps) can abruptly change the carrier density on a scale much smaller than τ (e.g., a few ps [61]), thus invalidating the adiabatic elimination of the optical signals over this time interval. After such an abrupt change, however, the carrier density recovers at a rate governed by the carrier lifetime τ , the time scale used for the adiabatic approximation, and our model is valid. The validity of the adiabatic approximation can also be threatened by a *slowly* varying set signal as well as the continuous-wave (CW) holding beam itself. By operating these signals at high powers, the carrier density responds to an effective carrier lifetime $\tau_{eff} = \tau / (1 + P_I/P_{sat})$ [61], which can approach the signal transit time (≈ 3 ps).

The internal power P_I in our simulations, however, does not exceed the saturation power, so our model remains valid for the cases considered here.

The control signals interact with the carrier-density energy spectrum at *well-localized* energies, namely $\hbar\omega_S$ and $\hbar\omega_R$. However, localized changes in carrier density at these energies are quickly distributed throughout the energy spectrum by intraband scattering in less than 1 ps. For longer time scales, the change in the SOA gain-curve spectrum, for a given change in the carrier density ΔN , is therefore independent of the control signal's optical frequency; i.e., the gain spectrum $g(\omega)$ is homogeneously broadened. The accompanying change in the refractive index $\Delta n(\omega_0)$ at the holding-beam frequency ω_0 is given by a Kramers-Kronig relation:

$$\Delta n(\omega_0) = -\frac{2c}{\pi} \int_{z=0}^{\infty} d\Omega \frac{\Delta g(\Omega)}{\Omega^2 - \omega_0^2}, \quad (6.15)$$

where Ω is the running-frequency variable, the integral is performed in accordance with the its principle value, and Δg is negative for a change due to gain saturation. Since the change in the SOA gain-curve spectrum Δg , is independent of the control signal's optical frequency (for a given change in the carrier density ΔN), the change in the refractive index $\Delta n(\omega_0)$ is also independent of the control signal's frequency. Since the linewidth enhancement factor α is proportional to the ratio of these changes, it is also independent of the control-signal frequency. Thus, a *common* value of α is used in the coupled-mode equations to transfer changes in gain (due to *any* signal) to changes in the refractive index at the holding-beam frequency.

Our model is now complete. The control-signal powers (5.16) and (5.16) are used within the modified gain rate equation (6.6). Once the gain is calculated for all time, the solution vector is used to find the holding-beam output powers using Eqs. (5.16) and (5.17) derived in Section 5.2.

We used this model to show how the hysteresis curve shifts in Fig. 6.5 and 6.6 under the application of CW set and reset signals, respectively [84]. The initial and final

Table 6.2: Parameter values for flip–flop control via control signals.

Set saturation power	$P_{S\text{sat}}$	10 mW
Reset saturation power	$P_{R\text{sat}}$	11.8 mW
Reset absorption	ηL	2.3
Set-pulse gaussian order	N	4
Reset-pulse gaussian order	M	4
Set Peak Power	S_i	0.1 mW
Reset peak power	R_i	1.02 mW
Set time center	t_S	23 ns
Reset time center	t_R	63 ns
Set Width	W_S	1 ns
Reset Width	W_R	1 ns

hystereses [parts (a) and (c)] are identical to the hysteresis curve of Fig. 6.2, and do not include control signals. The same parameter values are used in Fig. 6.5(b), except for a CW set signal with $P_{S0} = 84\mu\text{W}$. For Fig. 6.6(b), this set signal was replaced by a reset signal having a peak power of $P_{R0} = 1.2\text{ mW}$; other parameter values are given in Tables 6.1 and 6.2. We used a large integration step size $\Delta t = 100\tau$ which skips over the transient behavior at the switching thresholds. Such behavior is not central to our discussions regarding the stable output states [Fig. 6.2, 6.5, 6.6, 6.16(b)], but is included in the context of flip–flop operation (Fig. 6.3, 6.7, 6.17).

The model correctly simulates all-optical flip–flop operation; namely, the set signal switches the holding beam to a higher output-power state, which is maintained for a duration longer than the set-pulse width, and the holding beam power returns to its lower state upon the application of the reset pulse. As an example, we use input control pulses of the form

$$P_{S0}(t) = S_i \exp \left\{ -[(t - t_S)/W_S]^{2M} \right\}, \quad (6.16)$$

$$P_{R0}(t) = R_i \exp \left\{ -[(t - t_R)/W_R]^{2N} \right\}, \quad (6.17)$$

where S_i and R_i are the input amplitudes, t_S and t_R define the center of the pulses, W_S and W_R are proportional to the pulse widths, and M and N are the orders of the super-gaussian pulses. All-optical flip-flop operation is shown in Fig. 6.7, where the control signals are defined by parameter values given in Tables 6.1 and 6.2. In addition, $P_0 = 0.02$ mW; the holding-beam input is constant for flip-flop simulations and therefore the adiabatic-approximation condition that $h(t)$ vary slowly is always satisfied.

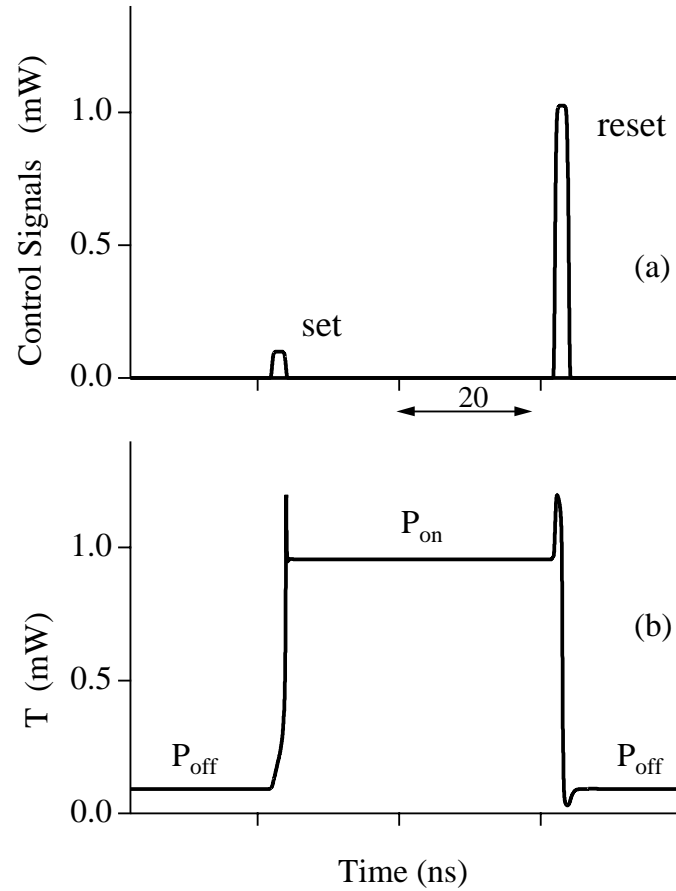


Figure 6.7: Flip-flop operation via auxiliary optical signals. (a) Set and reset signals control the (b) bistable transmission T by varying the hysteresis curve according to Fig. 6.5 and Fig. 6.6.

6.3 Experimental Demonstration

6.3.1 Experimental System

All-optical flip-flop operation was investigated using the experimental system shown in Fig. 6.8 [85]. The system is conceptually divided into three sections; control-signal generation, optical flip-flop, and detection.

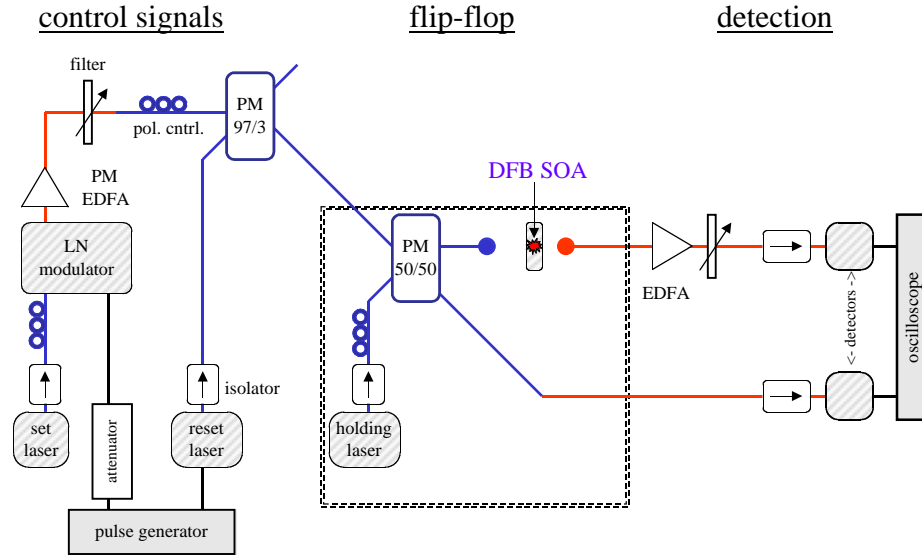


Figure 6.8: Experimental system for all-optical flip-flop demonstration.

Optical Flip-Flop

The optical flip-flop is enclosed by the hashed box in Fig. 6.8; its main ingredients are a DFB SOA, tapered fibers for optical coupling, a holding laser, and a fiber coupler. As a DFB SOA, we used a commercial DFB laser driven below lasing threshold; the device used for all experiments whose results are reported in this thesis is characterized in Appendix A. To control its temperature, the SOA chip was mounted to an aluminum heat sink using the process described in Appendix B. The heat sink was fastened to a brass block, which was itself connected to a thermo-electric cooler. The

heat sink also provided the electrical contact for the N-side of the SOA; the P-side received current through a contact probe placed on top of the SOA. The DFB SOA was mounted to allow access to both input and transmission facets by tapered fibers.

The CW holding beam originated from an external-cavity tunable-diode laser, having a wavelength range of 1499 nm to 1581 nm, a 0.001-nm fine adjustment, and a maximum output power of ≈ 6 mW. Since the holding-beam wavelength must be located at the long-wavelength side of the dominant DFB Bragg resonance, this tunable laser was ideal for accommodating the Bragg resonance of any DFB laser used in the course of experiments. In front of the holding laser, a 55-dB isolator prevented back reflections. The polarization controller was used to align the holding-beam polarization to the transverse-electric (TE) mode of the SOA gain region, and gave us the flexibility to explore the polarization dependence of flip–flop operation. The holding beam was sent into the DFB SOA through one branch of a 3-dB PM fiber coupler. The other branch accepted the optical control signals.

Control Signals

Set signal originated from an external-cavity tunable-diode laser having a nominal wavelength range of 1520 to 1570 nm, a fine adjustment of 0.01 nm, and a maximum power of ≈ 0.5 mW. We used this laser to provide the set signals, as opposed to the holding beam, because of its inferior fine adjustment of 0.01 nm. The laser was protected by an isolator, and its polarization was controlled for optimum coupling into a 5-GHz LiNbO₃ modulator. The 8-dB insertion loss from the modulator resulted in a transmitted power of less than 100 μ W. An erbium-doped fiber amplifier (EDFA) was used to boost and compensate for the loss from the modulator and the 3% port of a fiber coupler which combined the set and reset pulse trains. In front of this coupler, a filter removed much of the ASE noise from the EDFA, and a polarization controller was used for flexible alignment.

The reset wavelength in our experiments fell outside the SOA gain spectrum, to

the short-wavelength side. We found that lasers with a central wavelength near 1310 nm (for data generation in 1310-nm fiber-optic communication systems) or near 1480 nm (for EDFA pumping) were both capable of performing reset. The spectra from these lasers with respect to the SOA gain curve are shown in Fig. 6.9.

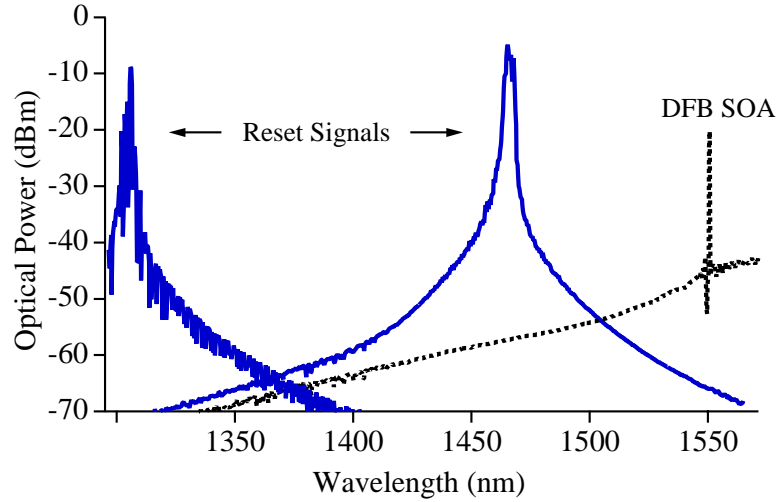


Figure 6.9: Spectra of two separate reset lasers compared to SOA gain curve.

Reset data was generated by direct modulation. We did not use the LiNbO_3 modulator because we did not have an optical amplifier to counteract its 8-dB insertion loss. To obtain modulated data with high-contrast ratios, the laser was biased near lasing threshold. To maintain as much reset-signal power as possible, the signals were passed through the dominant port of the 97/3 PM fiber coupler.

Control data was generated by a 3.5-GHz pulse-pattern generator. To clearly observe latching of the holding beam during the interval between the set and reset pulses, it was important to make this interval long relative to the set- and reset-pulse widths. Hence, a simple square-pulse train (with a 50% duty cycle) could not be used to clearly observe memory. The 32-bit programmable pattern capability of the pulse-pattern generator was very helpful for generating a signal train with a low duty cycle; for example, a '1' bit followed by 31 zeros provided a 1.6% duty cycle in return-to-zero (RZ) format.

We generated both the set and reset pulse trains simultaneously from the *same* pulse-pattern generator. One option for generating two electrical pulse trains was to simply use a junction to separate the output along two different cables; this technique, however reduced the output voltage to each laser and was sensitive to electrical feedback, promoting the generation of extraneous pulses. A separate source of pulses was available from the inverted output port $\overline{\text{OUTPUT}}$. However, if the output port (OUTPUT) is set for a 1.6% duty cycle (as in the example above), the inverted output port ($\overline{\text{OUTPUT}}$) has an unfortunate 98.4% duty cycle! We overcame this problem by feeding the inverted electrical signal from the $\overline{\text{OUTPUT}}$ port into a LiNbO₃ modulator *biased on the negative slope* of its transfer function. In this configuration, the modulator transferred the inverse of the electric signal onto the optical signal — an electrical signal having a 98.4% duty cycle created an optical signal having a 1.6% duty cycle. In this way, we created two low-duty-cycle pulse trains using a single pulse generator. During experiments, using two separate output ports (OUTPUT and $\overline{\text{OUTPUT}}$) was also useful since each could be turned on and off independently of the other, allowing each signal to be individually tested in the optical system.

The set and reset pulses, although created by the same data generator, separated in time by traversing different path lengths before being combined by the 97/3 fiber coupler. Since the set and reset pulse trains travelled different paths before the fiber coupler, their relative mismatch could be tuned by changing the repetition rate of the pulse generator. This technique allowed us, for example, to adjust the interval between the set and reset pulses and observe unambiguous latching of the bistable signal.

While the maximum output voltage from the pulse-pattern generator (3.3 V) beneficially created strong pulses from the directly modulated reset laser, it surpassed the voltage limit of the LiNbO₃ modulator. An electronic limiter was used to reduce the input voltage into the modulator voltage to below 2 V.

Detection

The control signals passed through the 3-dB fiber coupler within the hashed box of Fig. 6.8 on route to the DFB SOA. This coupler served the dual purpose of bringing both the control and holding signals into the DFB SOA, and of creating a reference input-pulse train for monitoring during experiments. Reference set and reset signals, as well as the flip-flop output signals, were measured with detectors having bandwidths exceeding 20 GHz, and either a digital-sampling oscilloscope, or a 500-MHz real-time oscilloscope. An isolator was used before each detector to protect the system from back reflections.

The real-time and digital-sampling oscilloscopes had minimum grid spacings of 1 and 2 mV, respectively. This difference seems innocuous, but was significant for some of the signals in our experiments. For a detector conversion gain of 10 mV / mW, a single oscilloscope grid requires 100 and 200 μ W of signal power, respectively. In our experiments, we used set signals as low as 22 μ W, which were therefore difficult to observe using the digital-sampling oscilloscope.

To clearly observe the flip-flop output, which was $\sim 100\mu$ W, we used an amplifier. Electronic amplifiers, however, were not appropriate because their low-frequency cut-off frequency warped the flat holding-beam signal that we tried to observe. Hence, we used an EDFA, as shown in Fig. 6.8. A tunable filter was placed after the to remove the wideband EDFA amplified spontaneous emission (ASE) and to block the amplified set pulses. The measured holding-beam powers given below were scaled to give the powers within the fiber before the EDFA. Input powers were measured in the reference arm and scaled to give the powers within the fiber before the DFB SOA.

6.3.2 Set–Reset Operation

Control signals for a typical experiment are shown in Fig. 6.10(a). The 1567-nm set signals had a peak power of $22\ \mu\text{W}$, and a pulse energy of 330 fJ. Reset was performed using 1306-nm signals with a peak power of 2.4 mW and a pulse energy of 36 pJ. The DFB SOA was biased at 97% of lasing threshold.

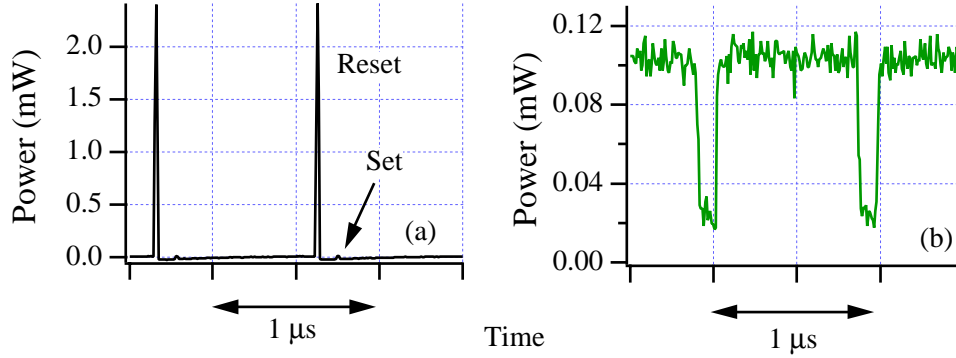


Figure 6.10: All-optical flip–flop operation. (a) 1567-nm set and 1306-nm reset signals controlling (b) the output power of the 1547-nm holding beam.

Control signals toggle the holding beam shown in Fig. 6.10(b) with a 6.2-dB contrast between 25- and $105\text{-}\mu\text{W}$ output states. Since its input power was $65\ \mu\text{W}$, the holding beam experiences a small fiber-to-fiber on-state gain. Note that the memory occurs at the holding-beam wavelength of 1547 nm, which is different than the set wavelength of 1567 nm.

The on state shown in Fig. 6.10(b) is maintained for $0.824\ \mu\text{s}$. This demonstration of a long, static set is important because it shows unambiguous latching of the flip–flop. A longer duration can be selected by using a pulse-pattern generator with a larger bit-pattern memory, or a slower pulse-repetition rate. The experimental data agrees qualitatively with simulations — gain-saturating and gain-pumping pulses set and reset the bistable output state of the DFB SOA, respectively. This agreement validates our understanding of the physical processes.

6.4 Performance

In this section, we investigate the performance of the flip–flop under a variety of operating conditions. In particular, we are interested in learning if the flip–flop is suitable for WDM fiber-optical communications systems.

6.4.1 Wavelength Range and Power

For use in WDM systems, the flip–flop should be able to be controlled by a wide range of signal wavelengths. Although this was not possible with previous techniques, the XPM optical-control techniques allow flip–flop operation over a wide range of wavelengths. Using the external-cavity tunable diode-laser, we achieved set operation from 1533 to 1568 nm, as depicted in Fig. 6.11. The short-wavelength bound of this range is where the set signal loses its ability to saturate the gain. The upper bound was imposed by the poor amplification of the EDFA (in control-signal portion of Fig. 6.8) at long wavelengths. Since 1568 nm is near the peak of the SOA gain spectrum, we expect the set range to extend at least 20 nm to longer wavelengths [86]. This large (> 50 nm) wavelength range is ideal for WDM lightwave systems; signals from a wide range of communication channels can serve to set the optical flip–flop.

The set-signal wavelength range extends on both sides of the Bragg resonance; flip–flop operation for 1537-nm set signals having a pulse power of 0.9 mW (and energy of 18 pJ) is shown in Fig. 6.12(a) [reset pulses are the same as for Fig. 6.10]. Thus, the XPM-setting technique works for signals that interact with the carrier-density distribution at lower *or* higher energies than the holding beam. Although 1567-nm set signals could be as low as 22 μ W (probably resulting from the high amplification at that wavelength), the minimum allowable optical power at 1537 nm was 85 μ W. These powers are low enough to expect that optical signals directly from the communication system can set the flip–flop without pre-amplification.

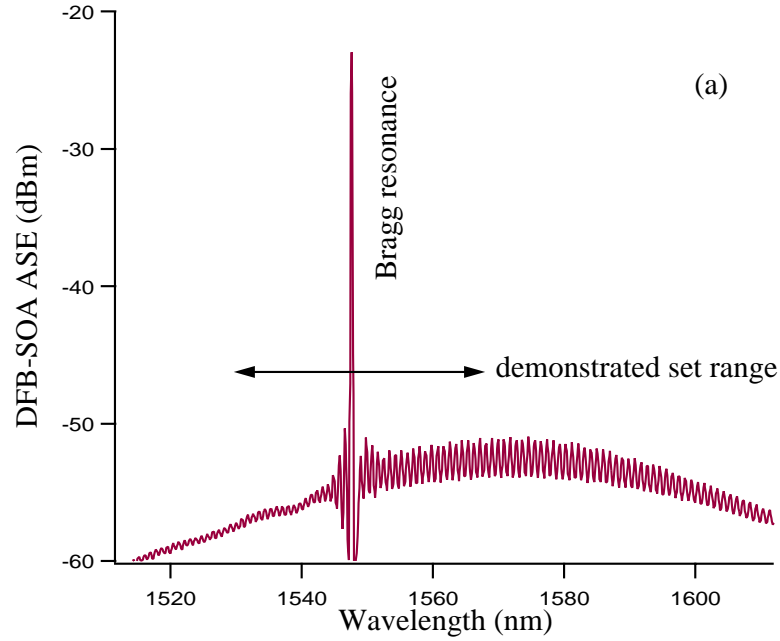


Figure 6.11: Broad spectral range of set signals. Demonstrated spectral range of set pulses compared to the ASE spectrum of the DFB SOA.

The broad wavelength range demonstrated for the set signal was eclipsed by that of the reset signal. We reset the holding-beam power shown in Fig. 6.12(b) using an EDFA-pump laser at 1466 nm (with pulse widths of 15-ns, and energies of 1.98 and 0.77 pJ for the reset and set signals, respectively). We expect that reset occurs over the intermediate 160-nm spectral range between 1306 and 1466 nm, and extends down to much shorter wavelengths; any optical frequency that excites electrons to the conduction band can potentially reset the flip-flop. Most importantly, we expect that all signals within the 1310-nm communication band can perform the reset function. This allows communication between the two well-developed systems centered near 1550 and 1310 nm. 1306-nm reset-signal powers were typically required to be above 0.7 mW.

Flip-flop operation occurred over a holding-signal wavelength range of only 0.004 nm in our experiments (for constant signal powers). Physically, this limited

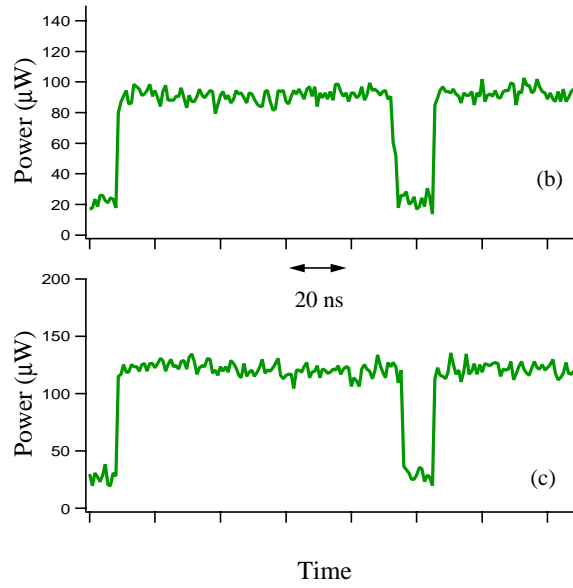


Figure 6.12: Flip-flop operation using (b) 1537-nm set and 1306-nm reset signals, and (c) 1567-nm set and 1466-nm reset signals.

wavelength range is a trade off for using a resonant-based device, which beneficially provides a high change in output power (6 dB) for small input powers ($< 100 \mu\text{W}$). However, by using XPM-control techniques, we have sheltered this limitation from the global optical system, and confined it to within the box labeled “Flip-Flop” in Fig. 6.1. Thus, from a systems point of view, the flip-flop has a very wide wavelength range of operation.

6.4.2 Direction and Polarization

Since the role of the control signals is to change the carrier density, they are not required to enter the SOA in a co-propagating direction with the holding beam; XPM was observed for control pulses entering either SOA facet. We expect that control signals can even enter from an off-axis direction [83]. Transparency regarding the incident direction allows flexibility in designing the control-signal input system, as well as in specifying the exiting direction of the amplified set signals.

We also investigated dependence on the polarization. In modern-day fiber-optic systems, the polarization of signals is not preserved during propagation. Thus, the flip-flop should be transparent to the control-signals' polarization. Optical reset was found to be transparent to the polarization of the 1306- and 1466-nm signals. However, flip-flop operation was dependent on the polarization of the set pulses. The polarization dependence for gain-saturating pulses is well known, and can be significantly reduced by using techniques such as growing the gain-region depth to the same scale as its width [88], or by using strained growth of the quantum wells. The polarization of the holding beam was also crucial for flip-flop operation; this is not a disadvantage since the holding laser can be located near the DFB SOA.

6.4.3 Set-Pulse Power

Since small powers (< 0.1 mW) are sufficient to set the flip-flop, data signals from an optical network can easily exceed the minimum required set power. In this section, we explore how the shape of the holding-beam output power is affected by a varied set-pulse power.

Although flip-flop operation still occurs between two flat output states P_{on} and P_{off} , an intermediate state P_x can appear during the duration of the set signal. Using rectangular set pulses (width ≈ 4 ns), this intermediate state takes the form of a flat ledge, as seen in Fig. 6.13(a) for a set power of 0.28 mW, and a holding-beam input power of 0.04 mW. We analyze the set-pulse ledge by first noting that the flat level of the ledge indicates that the system has achieved a steady state during the application of the set pulse. Thus, we can study this ledge behavior by simulating the bistable hysteresis curve under the influence of a CW set signal, as was used in Fig. 6.5 and 6.6 during the discussion on set and reset operation.

Using simulations, we find that a relatively large set-signal power ($P_{S0} = 0.28$ mW) pushes the upward-switching threshold well beyond the holding-beam input

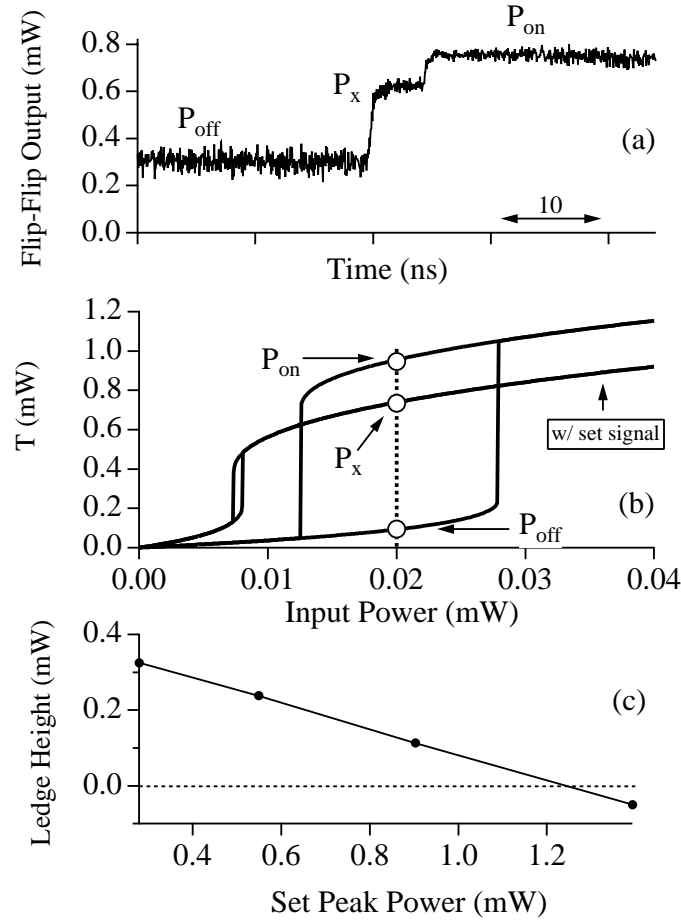


Figure 6.13: Set-pulse ledge. (a) Ledge feature P_x can occur during application of set pulse. (b) Severe hysteresis-curve shift is origin of ledge. (c) Ledge height $P_x - P_{\text{off}}$ decreases with set power.

power P_H , as seen in Fig. 6.13(b), where we have overlapped the bistable hysteresis with and without the set signal. (All other parameter values are listed in Tables 6.1 and 6.2.) The higher branch of the hysteresis curve drops accordingly, and therefore the output power switches from P_{off} to P_x . The intermediate state P_x is significantly lower than the final state P_{on} , which is obtained after the set pulse passes through the device.

The large difference between the upper branches of each hysteresis curve arises from both dispersive and gain-related effects; greater XPM pushes the Bragg reso-

nance away from the holding-beam wavelength, and larger gain saturation diminishes the strength of the Bragg resonance. These effects grow as the set-pulse power is increased. Therefore, the height of the ledge above the lower state $P_x - P_{\text{off}}$ diminishes as the set power is increases, as measured and shown in Fig. 6.13(c).

For a small range of set-pulse powers, the ledge height $P_x \approx P_{\text{off}}$, and the ledge is not visible. The ledge also goes unnoticed for low set powers, where $P_x \approx P_{\text{on}}$ since the flip–flop is set without too much variation in the hysteresis-branch height. Otherwise, set-pulse ledges will occur. Such ledges significantly warp the flip–flop output if their temporal widths are on the same order as the interval between set and reset signals. Relatively short set signals, however, do not significantly distort the holding-beam output shape.

6.4.4 Relative Strength of Control Signals

In experiments and simulations, we found that the required set-signal power was much smaller than that of the reset signal. The theoretical model presented here provides insight into the relative strength of these processes. The phase change $\Delta\phi$ experienced by the holding beam as the gain changes by an amount Δg , is given by the change in wavenumber, $\Delta\phi = -\Delta g L \alpha / 2$. Using the steady-state solution to the gain rate equation (6.6), and isolating the effects of the optical signals, the phase change is given by

$$\Delta\phi = \frac{\alpha}{D_\phi} \left[\frac{g_0 L}{2} \frac{\langle P_A \rangle + \langle P_B \rangle}{P_{\text{sat}}} + \frac{g_0 L}{2} \frac{\langle P_S \rangle}{P_{\text{Ssat}}} - \frac{\eta L}{2} \frac{\langle P_R \rangle}{P_{\text{Rsat}}} \right], \quad (6.18)$$

$$D_\phi = 1 + \frac{\langle P_A \rangle + \langle P_B \rangle}{P_{\text{sat}}} + \frac{\langle P_S \rangle}{P_{\text{Ssat}}}. \quad (6.19)$$

The three terms in the bracketed expression of Eq. (6.18) represent (from left to right) holding-beam SPM, set-signal XPM $\Delta\phi_{\text{SXPM}}$, and reset-signal XPM $\Delta\phi_{\text{RXPM}}$. For the parameter values used throughout this thesis ($\alpha = 5$, $g_0 L \approx 1.2$, and $\eta L = 2.3$),

the prefactors $\alpha g_0 L/2 \approx \pi$ and $\alpha \eta L/2 \approx 2\pi$. Thus, the strength of each signal power (within the SOA) relative to its saturation power determines the number of π phase shifts experienced by the holding beam.

For the case of small optical powers (relative to the saturation powers), the quantity $D_\phi \approx 1$. The expression for set-signal XPM can be estimated by using the average-power equation (6.13) with the small-signal limit $g = g_0$ and $P_{\text{Ssat}} = 10$ mW:

$$\Delta\phi_{\text{SXPM}} \approx 0.18\pi P_{S0}, \quad (6.20)$$

$$\Delta\phi_{\text{RXPM}} \approx -0.06\pi P_{R0}, \quad (6.21)$$

where the input powers are given in mW. The phase change for the reset signal $\Delta\phi_{\text{RXPM}}$ was obtained using (6.13) for the average power and $P_{\text{Rsat}} = 11.8$ mW.

To obtain the same amount of phase shift, Eqs. (6.20) and (6.21) reveal that the reset signal must provide more power than the set signal. In addition to a smaller saturation power, the set signals are amplified by the medium, as opposed to the absorbed reset signal. Moreover, the effect of the holding-beam power on the XPM phase changes (i.e. $D_\phi > 1$) makes it even more difficult for the reset XPM; whereas the set signal sees a relatively small internal holding-beam power, the reset signal sees a resonant-amplified holding beam, further reducing $\Delta\phi_{\text{RXPM}}$.

6.4.5 Speed

The set and reset times of the flip–flop signal shown in Fig. 6.10 are 16 ns and 24 ns, respectively, where we used 15-ns control signals and a real-time oscilloscope with a 8-ns resolution. Using a digital-sampling oscilloscope, the fastest rise and fall times were measured to be 300 ps and 700 ps, respectively, using 360 ps and 800 ps set and reset pulses, respectively.

Our experimental investigation into the maximum repetition rate of the all-optical

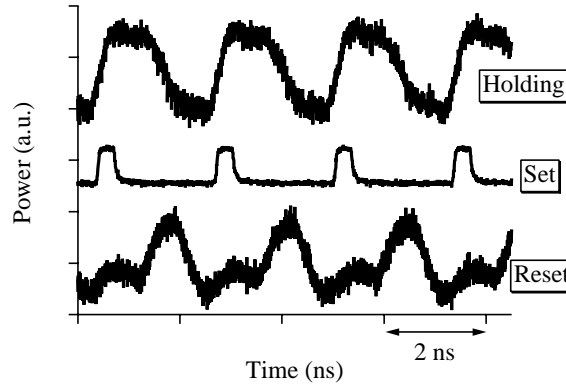


Figure 6.14: Flip-flop operation at 416 MHz, the high-speed limit is determined by the low modulation bandwidth of the reset laser.

flip-flop was limited by the low modulation bandwidth of the directly modulated reset laser (about 1 GHz). For a pulse-generator rate of 3.44 GHz, we achieved flip-flop operation using pulse widths of 360 ps and 800 ps for the set and reset signals, respectively, as shown in Fig. 6.14. Because of the wide reset pulses, clear flip-flop operation required a ‘10000000’ data pattern, which resulted in a set-to-set period of only 2.4 ns.

The physical limit to the repeatability rate of SOA devices is the inverse of the carrier recombination lifetime τ . We were hopeful that our optical-control techniques allow repetition rates faster than this limit because neither control process relies on the natural recovery of the SOA; set and reset signals effect a decrease and increase in the carrier density, respectively. We have investigated high-speed flip-flop operation with our numerical model, but have only achieved a set-to-set period of 90% τ . At high speeds, the reset signal’s effect on the carrier density must exactly balance the set signal’s effect — this balance is difficult to achieve. Such high-speed operation is therefore probably impractical for actual fiber-optic networks because it would require an input-power control scheme for each signal.

Although the repeatability rate seems to be ultimately limited by the carrier life-

time, the all-optical flip-flop *can be controlled by pulses shorter than this characteristic time*. As reported above, we performed set in our experiments using a 300-ps pulse. Using simulations, flip-flop operation was achieved with pulses a fraction of the carrier lifetime. For example, using a set signal having a $0.1\text{-}\tau$ rising edge and a $0.22\text{-}\tau$ width, we predicted that the flip-flop turns on within $0.5\text{ }\tau$, as shown in Fig. 6.15. Also shown, using a reset signal having a $0.6\text{-}\tau$ rising edge and a $2\text{-}\tau$ width, we predicted that the flip-flop turns off within $0.9\text{ }\tau$. As shown in Chapter 5, the hysteresis curve closes down for input signals modulated sinusoidally at rates approaching the carrier lifetime. This does not mean, as we have shown in Fig. 6.15, that bistable memory does not work for signals with pulse widths less than τ . We discuss the utility of using short pulses in Section 6.5.

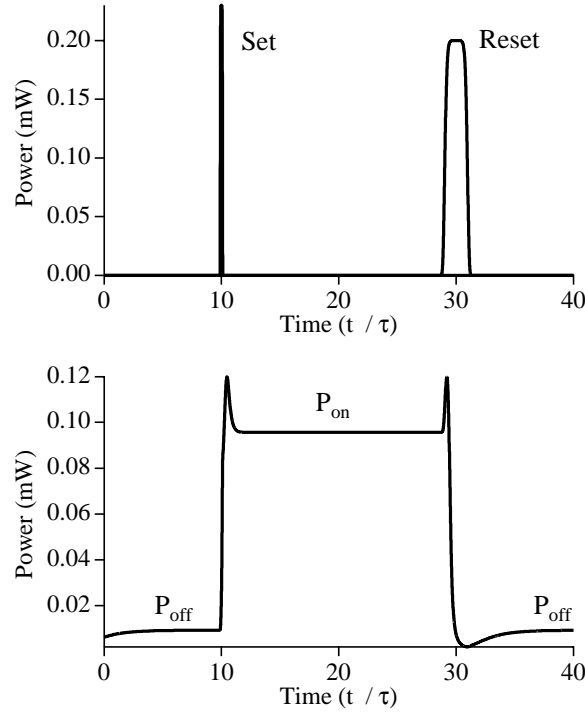


Figure 6.15: Flip-flop operation using a set pulse width of $0.22\text{ }\tau$.

6.4.6 Back-to-Back ‘Set’ Signals

Since set signals are envisioned to be taken directly from the optical system, there may be situations where multiple set signals enter the flip-flop before reset occurs. (All such ‘set’ signals are referred to here as set signals, although only the first one sees the flip-flop in its off state.) The stability and response of the flip-flop output power to back-to-back signals is therefore important to consider.

A pulse sequence of two set signals followed by a reset signal was used in experiments, as shown in Fig. 6.16(a), where the holding-beam power was $P_H = 0.068$ mW; the response of the flip-flop is shown in Fig. 6.16(b). The first and last pulses of this sequence perform set and reset, as expected. A ledge was produced for a set power of 0.59 mW, as described above.

While the holding beam is in the high-output state P_{on} , the second set signal enters the SOA. The flip-flop output power is reduced for the duration of the set signal, but returns to P_{on} after the signal dissipates. The notch in the output power can also be understood from the hystereses in Fig. 6.13(b) used to describe the set-pulse ledges. Unlike for the case of the ledges, however, the holding-beam output power begins in the high state P_{on} . The second set signal pushes the hysteresis curve to smaller switching powers, and the output power drops accordingly to P_x . However, since the switching thresholds do not cross the holding-beam input power, the final output state does not change; after the set pulse dissipates, the hysteresis curve returns to the original shape and the holding-beam returns to an output power of P_{on} .

Using our numerical model, we simulate the flip-flop response to back-to-back set pulses. Both set-pulse ledges and notches are obtained, as shown in Fig. 6.17, where the parameter values are the same as for Fig. 6.7, except $S_i = 0.6$ mW, $R_i = 2.2$ mW, $W_S = 0.8$ ns, $W_R = 0.6$ ns, and $t_R = 66$ ns. The second set signal is defined by $S_i = 0.6$ mW, $W_S = 0.8$ ns, and $t_s = 42$ ns. Set and reset switching exhibit spikes, as seen for numerical data shown in Fig. 6.7. The enhancement of the switching

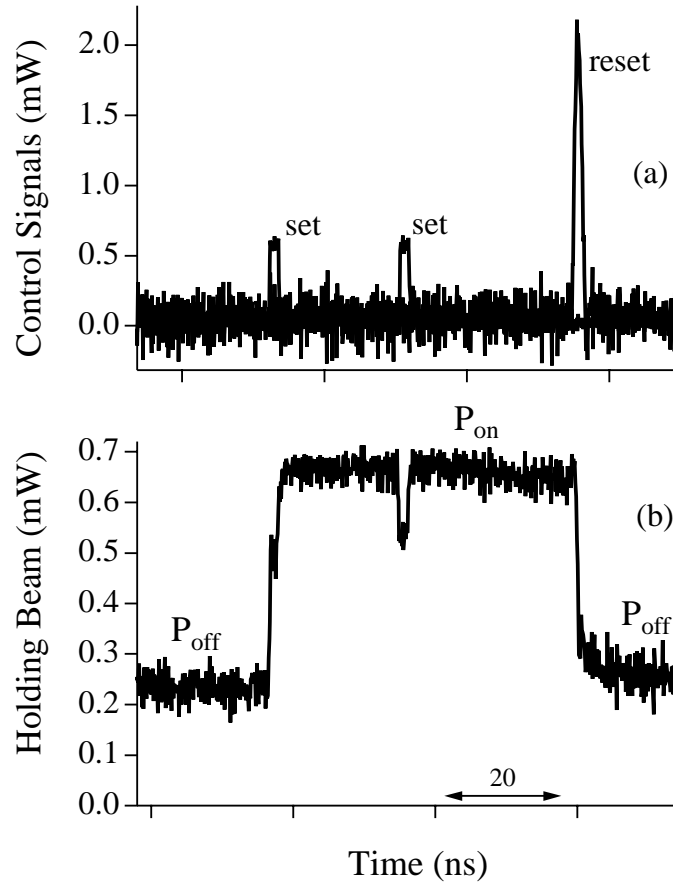


Figure 6.16: Back-to-back set signals. (a) Control signals — an additional set pulse enters the DFB SOA between set and reset signals. (b) In response, the holding beam transmission remains stable and only experiences a transient dip.

spikes in numerical simulations occurs as an artifact from the adiabatic elimination of the bistable signal from the system dynamics [23]. In addition, suppression of spikes in experimental measurements can result from the slow response of the detection scheme [36]; our 500 MHz oscilloscope may have diminished the measured spikes.

If the output power from the flip-flop is coupled into an optical network, fiber dispersion is expected to fill in the notches caused by set pulses that are short compared to the on-state duration. In this case, the notches will not persist.

These experiments on the response to multiple ‘set’ pulses also give information on the stability of the flip-flop. The second ‘set’ pulse, with peak power ~ 0.6 mW

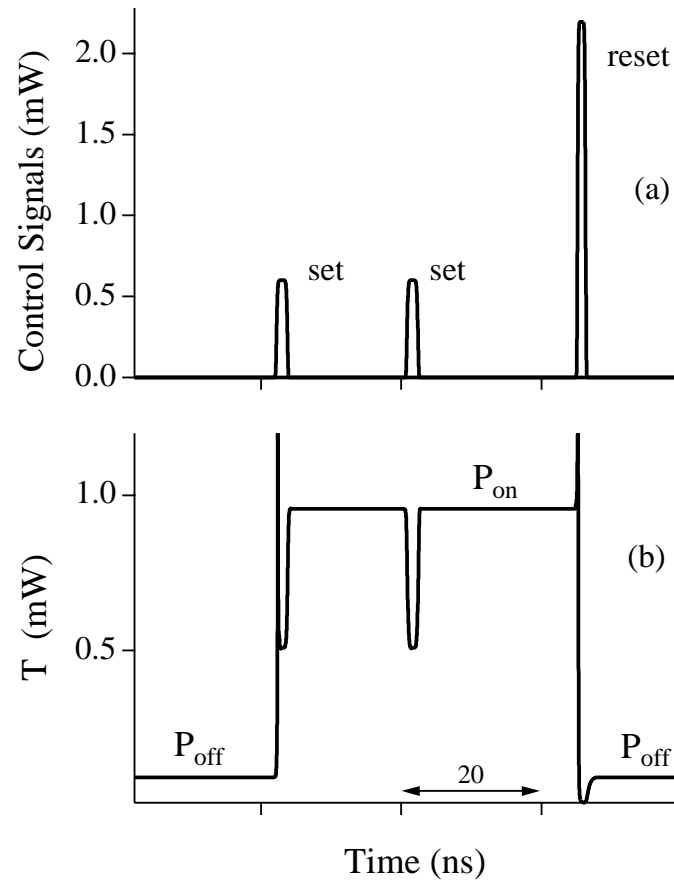


Figure 6.17: Simulated response of flip-flop to back-to-back set signals, showing a ledge and notch.

and pulse width ~ 4 ns, did not cause the holding-beam output power to become unstable and return to the lower level P_{off} .

6.5 Applications

The all-optical flip-flop has many features that make it suitable for WDM fiber-optic networks, including a wide wavelength range of control signals, reasonable optical powers, polarization independence of reset and set (expected) signals, and transparency to signal phase. These features *allow* the flip-flop to be used in a fiber-optic network, but do we *want* to use it? That is, is there an application for it? Applications

would have to accommodate a set-to-set repeatability rate below 10 GHz and a low number density of flip-flops.

The memory capability of the flip-flop allows a short signal to be stretched in time, thereby increasing its energy. For example, the 15-ns set pulses shown in Fig 6.10 activate the memory, which is held for 824 ns; i.e., the 330 fJ input pulse was converted to a 84 pJ pulse. This new pulse has steep sides and a flat top. Moreover, simulations show that a short pulse having a width of 0.22τ can trigger the flip-flop (Fig. 6.15). This capability may be useful for converting short pulses from a high-speed trunk line to long, higher-energy pulses for a low-speed, local-access systems comprised of low-cost, low-speed detectors.

Another application may be found in futuristic fiber-optic communication systems that use return-to-zero (RZ) format to transfer data over high-capacity fiber systems. Such a format would allow, for example, time-division multiplexing of signals, and the use of solitons. While trunk lines may require such high capacities, local networks might still retain the non-return-to-zero (NRZ) format and a lower data rate. Thus, a means converting high-speed RZ signals to low-speed NRZ signals would be desired.

To achieve RZ-to-NRZ conversion with our flip-flop, the RZ signals from the optical network are sent directly into the flip-flop and have wavelengths that set the device. The reset signals are generated locally (like a local optical clock), and enter the SOA as a steady stream of pulses. Set and reset pulse trains are timed to overlap each other, as shown in Fig. 6.18(a); the set-signal data pattern is ‘11001110,’ and the reset-signal pattern is simply ‘1111111.’

The key to operation lies in the relative strength of the set and reset signals. As observed in experiments (Section 6.4.1) and discussed in Section 6.4.4, set occurs at smaller powers than reset. Therefore, if both signals enter the SOA at the same time and are of the same order of magnitude, the set signals will override the reset signals. This reset-signal override produces an effective reset pulse train of ‘00110001.’ The

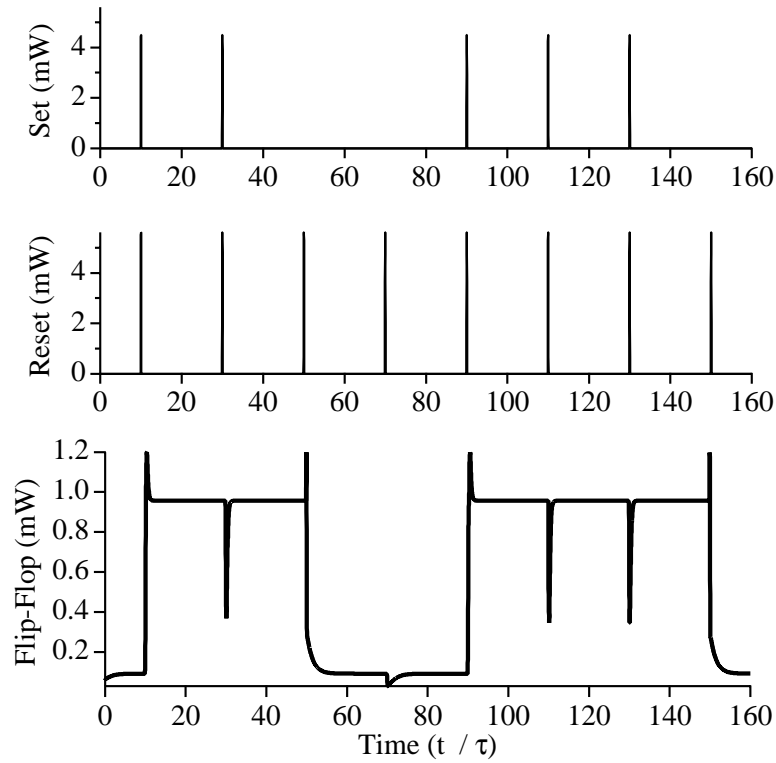


Figure 6.18: High-speed RZ to low-speed NRZ conversion. (a) High-speed, RZ signals from an optical network act as set pulses, and a local optical clock provides reset pulses. (b) The flip-flop output is of a low-speed NRZ format for a local-access system.

flip-flop output takes the form of NRZ data, as shown in Fig. 6.18(b). The notches caused by consecutive set pulses are discussed in Section 6.4.6, and do not significantly affect the output since the RZ pulses are much narrower than the NRZ bit length. The long bit length of local access systems accommodates the slow repeatability rate of the DFB SOA. Applications like these make this all-optical flip-flop appealing to fiber-optical communication systems.

6.6 Conclusion

We have demonstrated how to control the bistable output power from a resonant-type SOA via auxiliary optical signals. Instead of varying the holding-beam input

power, we vary the bistable hysteresis curve itself using auxiliary control signals that shift the photonic bandgap and Bragg resonances. Separating holding and control functionality is advantageous because the holding-beam laser can then be optimized solely for wavelength and power stability. Furthermore, set and reset can then be performed by signals directly from an optical network.

Control signals were found to operate at submilliwatt powers over wide wavelength ranges (> 35 -nm set range and > 160 -nm reset range) that intersect important communication bands centered near 1550 and 1310 nm. Hence, control signals can come from a variety of wavelength channels in modern-day wavelength division multiplexed (WDM) systems, where the channel spacing is ~ 0.8 nm. Control is transparent to the direction and phase of the optical signals, as well as to the polarization of the reset signal. We expect that the set-signal polarization dependence can be eliminated. Experiments were performed using a commercially available, telecommunications diode laser driven below lasing threshold. Thus, the flip–flop’s technology is already available.

The flip–flop is a building block for all-optical sequential processing, and we gave two examples of possible applications to high-speed fiber-optic communications. The flip–flop can convert high-speed RZ data to low-speed NRZ data. This application overcomes all of the limitations of optical bistability in resonant-type SOAs summarized in Section 1.2.2. Not only is the wavelength range of control signals long, but the application of conversion permits slow repetition rates. Moreover, only a small number of components are required — only the DFB SOA and holding laser are used. Another application is to use the digital-memory capability of the flip–flop to stretch a data pulse in time, thereby transforming it into a long pulse with more energy.

We also presented a simple time-dependent model which incorporates the bistable system and control signals, and gives qualitatively accurate results, which even predict such features as notches caused by back-to-back set signals and ledges caused by strong set-pulse powers. To arrive at a simple mathematical model, we invoked

approximations that are common to studies of optical bistability and nonlinear SOA dynamics. We expect the present model to be useful for further investigations into the response of the flip–flop, as well as for applications to optical systems.

Chapter 7

Data-Wavelength Conversion

7.1 Introduction

The capacity of fiber-optic communication systems can be increased by using wavelength-division multiplexing (WDM), in which signals of different wavelengths are transmitted simultaneously over a single fiber. WDM systems have already been commercially deployed in point-to-point transport links and are beginning to be used in multi-point networks [4]. Such systems also have the flexibility of routing signals based on their wavelength. This allows even a single channel to be dropped from a background of signals *without* electronic conversion [4].

In dealing with multi-wavelength optical networks, the capability of transferring data from one wavelength to another (called “wavelength conversion” in the literature) is important for many reasons. For example, a signal entering a fiber having many wavelength channels can be converted to a pre-specified wavelength to avoid channel contentions [4]. Moreover, a signal exiting from a high-capacity fiber having many wavelength channels and entering a low-capacity subsystem can be converted to a pre-specified wavelength for the subsystem; this would allow the mass production of many subsystems with the same wavelength specifications [90]. Data-wavelength conversion can also be used with wavelength routers to control the flow of signals through a network.

Currently, the most successful wavelength-conversion technique is based on electronic processing [4]; an optical signal is detected, and the resulting electrical signal drives an external modulator for a laser at a different wavelength. This technique beneficially regenerates the signal with a good extinction ratio and low noise, and the converted wavelength can be one of the wide variety of wavelengths produced by semiconductor lasers. However, the conversion speed is currently limited by the detector and modulator to ~ 10 Gb/s, and achieving substantially faster speeds is expected to be expensive.

In anticipation of the speed limitations of opto-electronic wavelength conversion, there has been intensive research into all-optical techniques [86], [89]–[94]. In this chapter, we demonstrate wavelength conversion using a DFB SOA. We focus on 1310-to-1550 nm wavelength conversion, which would bring flexibility to a high-bandwidth fiber-optic network using *both* low-loss spectral windows located near 1310 and 1550 nm. We discuss our experimental system, demonstrate 1306-to-1547 nm and 1466-to-1547 nm wavelength conversion, and explore the conversion dependence on such aspects as wavelength, polarization, and data rate. Then, we demonstrate wavelength conversion between signals within the 1550-nm spectral window, and compare our research with other all-optical techniques.

7.2 Experimental System

We achieved wavelength conversion using the experimental system is depicted in Fig. 7.1. The 1310-nm data was generated using a directly modulated Fabry–Perot laser biased slightly above threshold. A polarization-maintaining 3-dB coupler, designed for 1550-nm light, passed about 80% of the 1310-nm data signal toward the DFB SOA. We used a tunable laser to provide the continuous-wave (CW) probe, which interacted with the Bragg resonance located at the long-wavelength edge of the DFB stop band. Optical signals were coupled in and out of the DFB SOA via ta-

pered fibers; coupling was assisted by an anti-reflection (AR) coating (optimized for 1550-nm light) applied to the input facet of the SOA. An erbium-doped fiber amplifier (EDFA) boosted the converted signal, and a tunable filter reduced the amplified spontaneous emission (ASE). Converted signals were measured using a 25-GHz detector and a digital-sampling oscilloscope with a 20-GHz sampling head. Input powers were measured at the input fiber before the DFB SOA. Converted-signal powers were scaled by the output-branch gain to give power values within the fiber, before the EDFA.

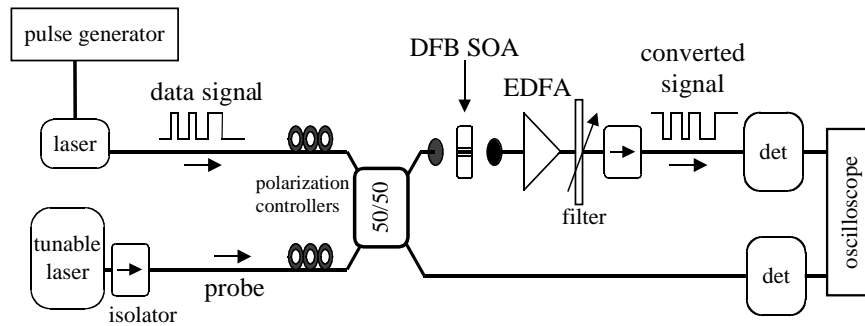


Figure 7.1: Experimental system. Transmission of a CW, 1.5- μm probe beam through a DFB SOA is modulated by a data signal at a different wavelength.

7.3 1306-to-1547 nm Conversion

We achieved 1306-to-1547 nm data-wavelength conversion in a DFB SOA by tuning a CW probe signal near the Bragg resonance at 1547 nm [95]. The 1306-nm data signals are absorbed by the SOA, thereby creating charge carriers within the device's active region. As a result, the gain and refractive index experienced by the probe signal are increased and decreased, respectively. Most notably, the strength and location of the Bragg resonance with respect to the probe signal is changed, and this process maps the data from the input signal to the transmitted probe signal.

7.3.1 Polarity Selection

Two types of wavelength-converted signals are shown in Fig. 7.2, where the DFB SOA was biased at 96% of the lasing threshold. Polarity-preserved data transfer occurs for most probe wavelengths tuned on the short-wavelength side of the Bragg resonance [e.g., at 1547.707 nm as shown in Fig. 7.2]. The probe experiences a transient increase in its transmission because the pump-induced decrease in refractive index shifts the Bragg resonance into the probe wavelength. Transmission is also increased by the accompanying increase in gain which strengthens the Bragg resonance. We have avoided, though, pump levels that strengthen the Bragg resonance so much that a measurable signal is generated even without a probe beam [94].

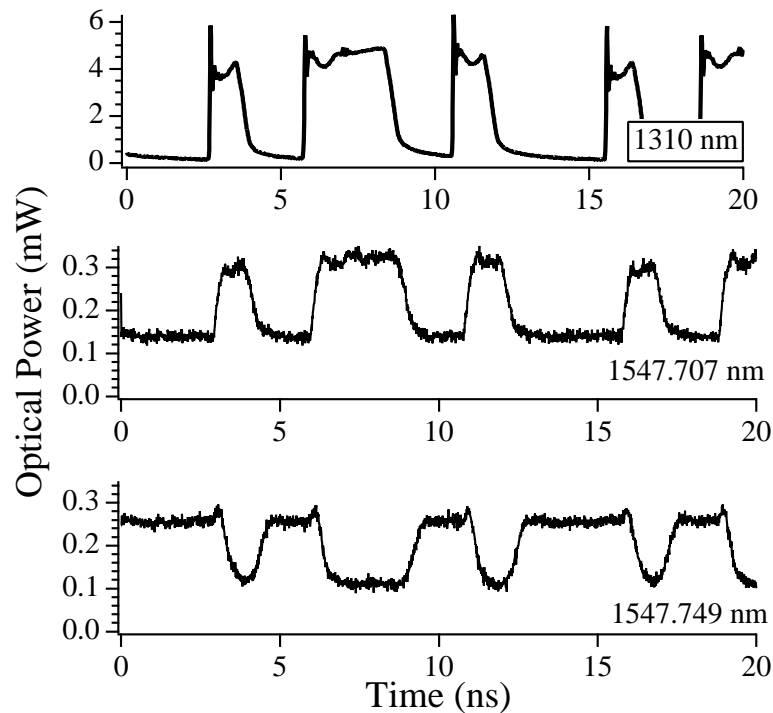


Figure 7.2: Wavelength conversion from a 1306-nm, 622 Mb/s, ‘10110100’ NRZ input signal. Polarity of converted signal depends on probe wavelength.

The converted-data polarity can be changed by tuning the probe-wavelength on the long-wavelength side of the the Bragg resonance; as shown in Fig. 7.2 at 1547.749

nm, polarity-inverted conversion occurs. In this case, the pump-induced decrease in refractive index moves the Bragg resonance *away* from the probe wavelength, decreasing the output power. The transition between polarity-preserved and polarity-inverted wavelength conversion is shown in Fig. 7.3, where the contrast ratio is the ratio of the 1547-nm output power with the application of a 1466-nm signal relative to the output power without it.

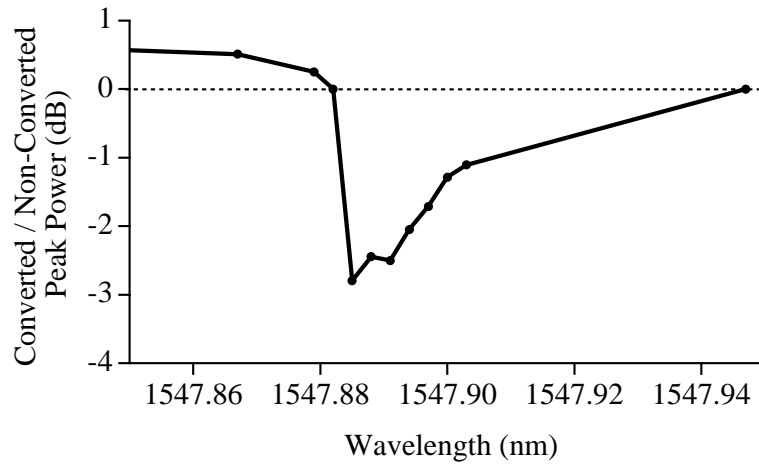


Figure 7.3: Polarity inversion of converted data. A negative contrast ratio (in dB) indicates polarity-inverted conversion.

7.3.2 Wavelength Range of Data Signals

Wavelength conversion will occur, in principle, for any wavelength that increases the carrier density. In addition to the 1306-nm signals shown above, we expect that the same device can convert data from all wavelengths in the 1310-nm communication window. We have also demonstrated wavelength conversion using a EDFA-pump laser at 1466 nm, establishing a 160-nm range of input-data wavelengths. The long-wavelength limit of this spectral range is determined by the SOA gain curve, and can be adjusted by the semiconductor composition.

Conversion is shown in Fig. 7.4 for 1466-nm input data and for both kinds of polarity, where the DFB SOA was biased at 98% threshold, and the probe power was

75 μ W. The home-made 1466-nm laser mount had a modulation bandwidth below the low-frequency cut-off frequency (33 MHz) of the pulse-pattern generator used for the 1306-nm laser. Data signals were therefore generated by biasing the 1466-nm laser below threshold and applying a sinusoidal current from a function generator. This technique limited the data stream to a pulse train of 1's shaped like bullets, as shown at the top of Fig. 7.4. In the inverted-polarity case, an asymmetry is apparent between the two edges of the converted signal: downward switching occurs at a higher data-input power than upward switching. This behavior is indicative of hysteresis.

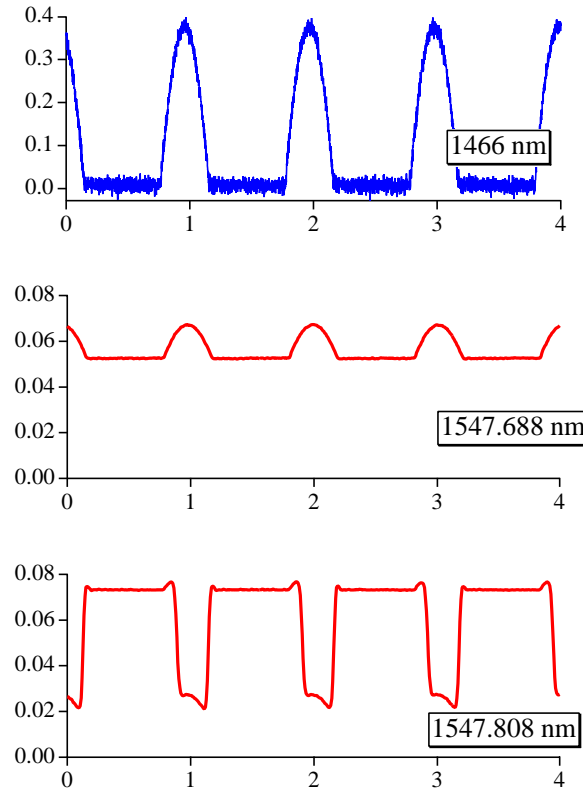


Figure 7.4: Wavelength conversion from a 1466-nm, 1 Mb/s, '11' RZ input signal. Polarity of converted signal depends on the probe wavelength.

7.3.3 Linear and Nonlinear Transfer Functions

The positive-feedback loop leading to optical bistability produces a qualitative difference between the transfer functions of the two polarity types of wavelength conversion, as shown in Fig. 7.5 for 1306-nm data. For polarity-preserved signals, the on–off ratio grows almost linearly with the peak input power. [On–off ratios (for all data) are measured using an alternating ‘10’ RZ data pattern.] However, polarity-inverted signals exhibit a nonlinear, digital-like transfer function. The decreased probe power within the device allows the carrier density to recover, reducing the refractive index and shifting the Bragg resonance further away from the probe wavelength. The relatively flat high- and low-contrast regions are advantageous because they can perform signal reshaping, thereby decreasing the bit-error rate. At 155.5 Mb/s, an on–off ratio of about 4 extends over an input-power dynamic range of 2 mW, for a device driven at 98% lasing threshold [Fig. 7.5(b)]. We expect this range to extend to higher powers.

7.3.4 Data and Probe Signals

Relatively high 1310-nm-signal powers (> 1 mW) were required to pump the SOA, but this power level can be reduced by optimizing the coupling efficiency (e.g., using a 1310-nm-optimized AR coating). Many advantages occur, however, *because* the role of the input signal is to pump the SOA. We found extinction of the 1310-nm signal during the conversion process. Therefore, a post-conversion optical filter is not required to remove the injected data signal. Data transfer was also found to be transparent to the polarization state of the 1310-nm light. Furthermore, data transfer occurred for input signals propagating in the same or opposite direction with respect to the probe signal.

Using a probe power of $3.9 \mu\text{W}$, it was common to realize > 15 -dB fiber-to-fiber conversion gain at the signal peaks (18 dB for Fig. 7.2). The on–off ratio was maximized by aligning the probe polarization with the transverse-electric (TE) mode of

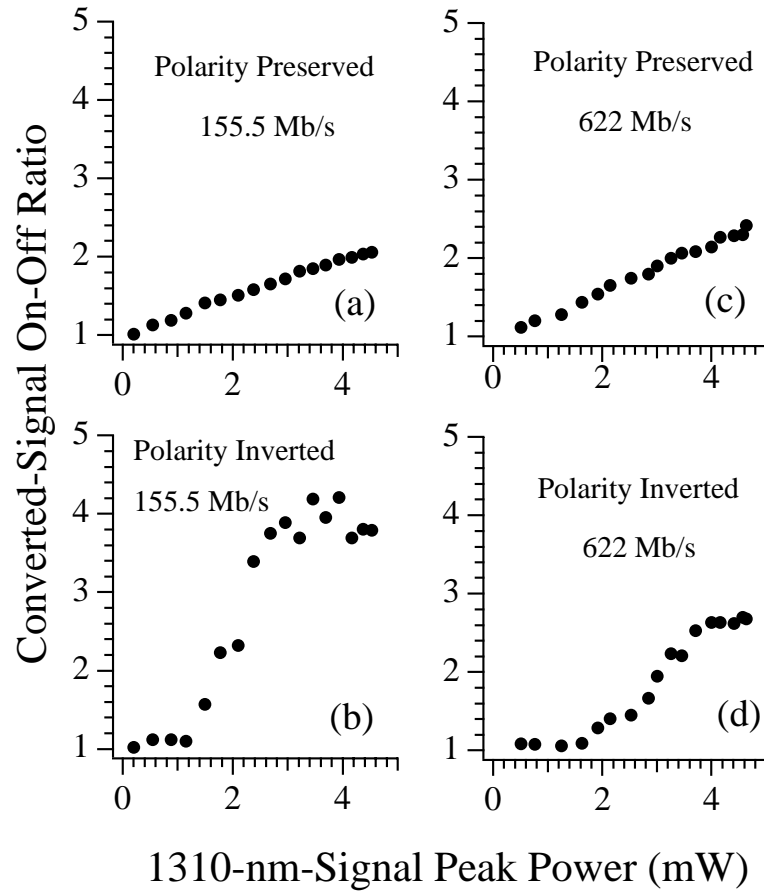


Figure 7.5: Transfer function of wavelength-converted signals. Polarity-preserved signals exhibit a near-linear increase in on-off ratio, while polarity-inverted signals exhibit a digital-like transfer function.

the SOA. We measured the wavelength range of the probe to be 0.068 and 0.02 nm for polarity-preserved and polarity-inverted signals, respectively. Since these spectral ranges are small, data can only be transferred to a single WDM communication channel. A fixed output-wavelength converter is useful; for example, fixed-wavelength devices avoid channel contentions between signals merging onto a single fiber [4].

Precise alignment of the probe wavelength and DFB resonance can be achieved by integrating both devices onto the same chip, using an electron beam to write each grating. Alignment can also be performed by tuning the Bragg resonance via the

injection current. Using polarity-preserved data, for example, a decrease of 0.38 mA (2% of threshold) accommodated a probe-wavelength increase of about 0.03 nm. Similar on–off ratios were maintained at the same data rate (155 Mb/s) and even at 622 Mb/s, as shown in Fig. 7.5(c).

7.3.5 Dependence on Data Rate

As the data rate approaches the carrier lifetime (~ 1 ns), the on–off ratio is expected to decrease. For polarity-preserved conversion, however, the high optical intensity effectively reduces this lifetime through stimulated emission. Polarity-inverted data, with lower intensity, is compromised even at 622 Mb/s, as shown in Fig. 7.5(d) at 98% threshold (similar performance at 96%). At faster rates of 900 and 1250 Mb/s, the on–off ratio dropped to 2.3 and 1.7, respectively. Using a ‘10110100’ data sequence, serious pattern effects were observed above 1 Gb/s resulting, in part, from the modulation bandwidth of the 1310-nm diode laser. Pattern effects began near 700 Mb/s, and became large at 900 Mb/s for NRZ data, as shown in Fig. 7.6 (98% lasing threshold), but remained small for RZ input and converted data.

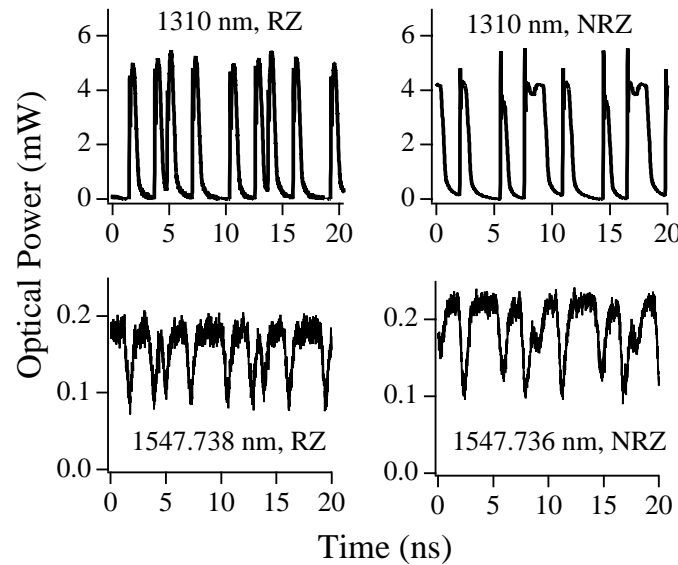


Figure 7.6: Patterning effects at 900 Mb/s for RZ and NRZ signals with a ‘10110100’ data sequence.

7.4 Conversion within the 1550-nm Spectral Window

Although we have focused on wavelength conversion from a shorter wavelength (1306 or 1466 nm) to the communication spectral window centered near 1550 nm, conversion between two signals within the 1550-nm window can also be performed with the DFB SOA. All-optical data conversion between signals of wavelength separation less than 50 nm has been intensively investigated since the early 1990's (e.g., [89], [90]), and has advanced considerably; indeed, all-optical wavelength conversion has recently been demonstrated at 100 Gb/s using a fully integrated and packaged device [6].

Within a DFB SOA, a Bragg resonance can be shifted on and off the probe wavelength (polarity-preserved conversion), or off and on the probe wavelength (polarity-inverted conversion), by using gain-saturating signals. These data signals saturate the gain and *increase* the refractive index experienced by the probe signal, shifting the resonance in the opposite direction as the gain-pumping 1306- and 1466-nm signals described above. We did not study conversion within the 1550-nm window in detail, and present here only its basic demonstration. Polarity-inverted wavelength conversion at 1.25 Gb/s is shown in Fig. 7.7 for NRZ signals, a 3- μ W probe signal, and a DFB SOA driven at 90% lasing threshold. (This high data rate was achieved using an external LiNO₃ modulator, inserted after the data laser in Fig. 7.1.)

7.5 Comparison with Related Research

7.5.1 1310-to-1550 nm Wavelength Converters

The performance of our 1310-to-1550 nm conversion technique is on par with other demonstrations [91]–[94]. For example, the measured on–off ratios (OORs) are similar: a nonlinear optical loop-mirror technique [93] provided a value of 6 ('10011100' RZ at 76 Mb/s); a split-contact device [94] provided 2 [pseudo-random binary-

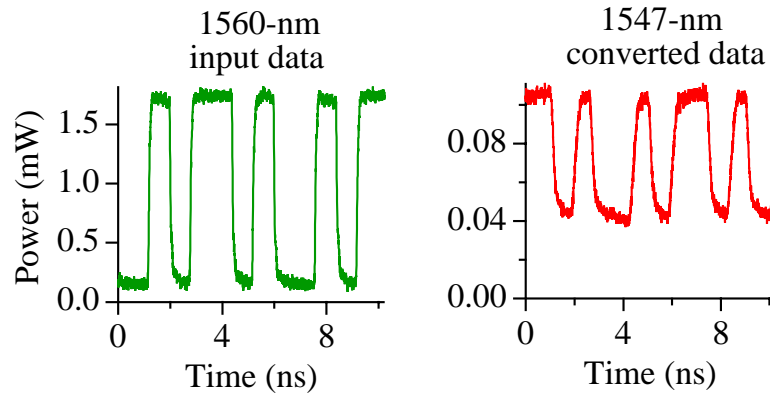


Figure 7.7: Polarity-inverted wavelength conversion from 1560 nm to 1547 nm using ‘10110100’ NRZ data at 1.25 Gb/s.

sequence (PRBS) at 155 Mb/s), and below 2 (‘10’ RZ at 700 Mb/s); a difference-frequency technique [92] and the XPM technique of Ref. [91] were not reported with OOR values, but the later implied poor performance by mentioning methods of improvement. For our converter, we measured OORs of 4, 2.3, and 1.7, at 155.5, 900, and 1250 Mb/s, respectively, using ‘10’ RZ data.

A unique feature found in our all-optical conversion experiments is the inherent, digital-like transfer function shown in Fig. 7.5. Digital transfer functions are beneficial because they produce output pulses of equal peak power, regardless of the input power, as long as it surpasses the threshold region. Moreover, the flat tail of the transfer function is useful for suppressing noise. Conversely, wavelength converters based on interferometric techniques, for example, have an inherently periodic transfer function and typically exhibit a poor dynamic range of the input data power.

Our 1310-to-1550 nm conversion technique is similar to another method that used a split-contact, Fabry–Perot SOA [94]. In such a device, a section in front of the SOA was biased as an absorber for 1550-nm and 1310-nm light. 1310-nm signals entered the absorbing region and moved charge carriers to the conduction band, thereby increasing the gain experienced by the 1550-nm probe signal. We expect that the resulting change in the refractive index was the basis of their data conversion. Both

kinds of data polarity were reported; although a digital-like transfer function was not reported, we expect that one can be achieved.

7.5.2 Interferometric-based Wavelength Converters

Many wavelength-conversion techniques make use Mach-Zehnder Interferometers (MZIs) [6]–[91]. The role of the interferometer is to interfere the probe signal with itself, creating phase conditions of high and low output power. The data signals entering the interferometer change the phase experienced by the probe signal via XPM, thereby changing its output power. Our configuration of wavelength conversion can be thought of as substituting the MZI with a diffraction grating — the key is a device that produces interference of the probe signal. Any resonant-type SOA will work; indeed, in 1987, wavelength conversion was demonstrated within the 1550-nm spectral window using Fabry–Perot SOAs [24]–[26]. Resonant-type SOAs are compact, but cannot make use of the carrier-lifetime-defying tricks implemented in MZI devices, such as placing an SOA in each branch of the interferometer [79].

To achieve 1310-to-1550 nm wavelength conversion, we use signals that *generate* charge carriers and decrease the refractive index. Other wavelength converters based on XPM operate via the the reverse process: *carrier-depleting* signals that increase the refractive index [86], [89], [91]. We expect that these converters can also be used “in reverse” with carrier-generating signals to allow 1310-to-1550 nm wavelength conversion.

7.5.3 All-Optical Flip–Flop

Wavelength conversion demonstrated in this chapter is closely related to the all-optical flip–flop operation discussed in Chapter 6. Indeed, cross-phase modulation (XPM) processes via carrier-depleting signals (for 1550-nm-window conversion) and carrier-generating signals (for 1310-to-1550 nm conversion) were used in tandem as

set and reset signals, respectively (see Section 6.2.2 for a discussion). The flip–flop behavior can be thought of as a kind of data-wavelength conversion *with memory* — the input data is not replicated at the new wavelength, but rather, stored as a new output state.

Memory occurs if the probe beam (i.e., holding beam) is initially tuned within the hysteresis, as shown in Fig. 6.2. Setting the probe beam at the low-input-power side of the hysteresis allows XPM wavelength conversion using carrier-depleting signals (1550-nm-window conversion), and setting the probe beam at the high-input-power side allows XPM wavelength conversion using carrier-generating signals (1310-to-1550 nm conversion); the transfer function of both cases will be nonlinear, assisted by the positive feedback loop that leads to bistable switching. Without hysteresis, memory cannot occur, but data-wavelength conversion can still be achieved; examples are given in Fig. 7.2 (middle plot), and Fig. 7.5 (a) and (c).

7.6 Conclusion

Using a DFB SOA, we transferred data to a 1547-nm signal (which is in the vicinity of the Bragg wavelength) from initial data signals at 1306 nm, 1466 nm, and 1560 nm. Initial data signals at 1560 nm were converted using a gain-saturating XPM technique that has been used in other geometries (e.g., MZI [89]). Conversion from the shorter wavelengths of 1306 and 1466 nm, however, was performed using a gain-pumping XPM technique in which the data signals decreased the refractive index.

The polarity of the converted signal can be selected by the relative location of the probe wavelength with respect to the Bragg wavelength. For polarity-inverted, 1306-to-1547 nm conversion, we measured a digital-like transfer function and an on–off ratio of 4 at 155.5 Mb/s. Conversion from short wavelengths (1306 and 1466 nm) was also found to be transparent to the input-data polarization. The converted on–off ratio reduced to values of 1.7 and 2.5 at 1.25 Gb/s, for input data at 1306

and 1560 nm, respectively (where the 1306-nm data was limited, in part, by the modulation bandwidth of the data laser). The speed of the conversion process is ultimately limited by the carrier lifetime. Unless a way is developed to improve or bypass this limitation, it is unlikely that the techniques demonstrated in this chapter will outperform opto-electronic data-wavelength conversion.

Although the speed of this conversion process is currently limited by the carrier lifetime, our research has demonstrated two general principles: 1) XPM-based wavelength conversion using carrier *generation* can be implemented in gain-biased SOAs, and 2) bistable systems can give rise to a data-wavelength conversion process that exhibits a digital-like transfer function. Both principles are applicable to other data-wavelength conversion schemes. XPM via carrier-generating signals can be applied to any SOA wavelength converter currently based on XPM via carrier-depleting signals (e.g., [89]), and would significantly increase their wavelength range of operation. Carrier-generating signals may also be effective in nonlinear materials governed by the free-carrier plasma interaction [96]. In addition, the highly beneficial digital transfer function can be sought out in other systems that exhibit bistability for the application of data-wavelength conversion.

Chapter 8

Concluding Remarks

8.1 Overview

This thesis explored the nonlinear response of DFB SOAs, and advanced their applicability to fiber-optic communication networks. In this chapter, we summarize four research areas: the spectral range of optical bistability, the shape of the bistable hysteresis curve, all-optical flip–flop operation, and data-wavelength conversion. In each section, we review our major findings, and suggest ideas for future research. We close this chapter with a summary of major contributions.

8.2 Spectral Range of Bistability

As discussed in Section 1.2, the bistable response of typical DFB SOAs exhibits a limited wavelength range. In Chapter 3, we quantified this range by calculating the switching-threshold powers of bistability. We found that switching below 0.1 mW occurs over only a wavelength range of 0.19 nm, and is accompanied by a poor spectral uniformity exhibited by the bistable hysteresis curves. In Chapter 4, we improved the spectral range of bistability by introducing spatial chirp into the Bragg grating. We showed that a linear variation in the grating period of 0.24% nearly triples the spectral range of low-power switching. Spatial chirp breaks the directional

symmetry through the DFB SOA, and we investigated both directions of propagation for signal wavelengths on both sides of the photonic bandgap; the aforementioned improvement in spectral range occurs for optical signals tuned to the long-wavelength side of the stop band and sent into the device in the direction of increasing grating period. For such signals, the spectral uniformity of the bistable hysteresis curve is also improved; a common input power can be selected that falls within the hysteresis curve of signal wavelengths spanning 0.1 nm, and the high and low output powers are well defined over this range.

Demonstration of these improvements to the spectral range and uniformity awaits future research. A promising technique for fabricating continuously chirped gratings using electron-beam lithography has been developed recently [97]. This technique has been used to fabricate complex-coupled DFB SOAs with and without linear spatial chirp. Preliminary experiments on bistable switching in these devices revealed that switching in the chirped-grating amplifier exhibits a wider spectral range, lower switching-threshold powers, and smaller contrast ratios [97]; all of these effects agree with our simulations for switching on the short-wavelength side of the stop band for signals sent into the device in the direction of decreasing grating period. Further testing is needed to explore both directions of propagation for signal wavelengths on both sides of the photonic bandgap, and to study the spectral uniformity of switching.

8.3 Shape of Bistable Hysteresis Curves

In Chapter 3, we discussed the variety of shapes that occur for the hysteresis curve on reflection. We explained this variety in terms of the reflectivity Bragg resonances. These resonances were shown in Chapter 2 to invert from high-amplification peaks to zero-reflection dips as the small-signal gain g_0 was decreased from near lasing threshold. The reflectivity resonances also invert in this manner when the gain is decreased via stimulated emission (i.e., gain saturation). As the initial detuning of

the optical signal from the Bragg resonances is increased, larger optical powers are required to seed bistability, resulting in higher amounts of gain saturation. Therefore, as the detuning is increased, the hysteresis curve deforms from its typical S-shape, to a loop shape, and finally to an inverted S-shape. Our simulations show that the intermediate loop shape is qualitatively different at the two edges of the photonic bandgap.

The family of possible shapes exhibited by the hysteresis curve can be suppressed in devices with spatially chirped gratings, yielding *only* the familiar S-shape. This suppression occurs for the case highlighted in the previous section as having a large spectral range and good spectral uniformity (i.e., the case where optical signals are tuned to the long-wavelength side of the stop band and sent into the device in the direction of increasing grating period). For other propagation conditions, the loop-shaped and inverted-S-shaped hystereses can be enhanced. We predicted that spatial chirp can be used to push the reflectivity resonance down to a low state of reflection, yielding contrast ratio exceeding $10^5:1$. However, this very high contrast ratio occurs only for upward switching, and is accompanied by low amplification, a narrow spectral range, and a small contrast ratio for downward switching.

The large switching contrast provided by the reflectivity dip is nonetheless intriguing. Ideally, the optical signal experiences the low-reflectivity dip *and* a high-reflectivity peak during the switching process, resulting in high-gain, high-contrast switching. Such behavior may be achieved through optimizing device parameters such as the coupling strength and the chirp profile, as well as considering reflectivity resonances away from the photonic bandgap.

8.4 All-Optical Flip-Flop

In Chapter 6, we demonstrated all-optical flip-flop operation of a bistable DFB SOA using techniques that control the bistable output state via auxiliary optical signals. We

demonstrated optical ‘set’ using signal wavelengths between 1533 and 1568 nm, having powers as low as $22 \mu\text{W}$. Optical ‘reset’ was performed with signals at 1306 and 1466 nm, having minimum powers below 1 mW. These control techniques *greatly extend* the wavelength range of flip–flop operation; previous techniques were based on changing the input power of the bistable signal itself, or based on interfering the bistable signal with a reset signal detuned by 0.008 nm. We expect the wavelength range of set and reset signals of the new techniques to exceed 50 nm and 200 nm, respectively. Moreover, the spectral ranges of the set and reset signals conveniently overlap the communication bands centered near 1550 and 1310 nm, respectively. Thus, signals from a wide range of channels in WDM optical networks can serve to set and reset the flip–flop.

Optical set and reset signals increase and decrease the refractive index, respectively, via complementary cross-phase modulation (XPM) techniques. The set signals fall within the SOA gain spectrum, and deplete the carrier density through stimulated emission. This leads to an increase in refractive index at the holding-beam wavelength, as embodied by the linewidth enhancement factor α . The wavelength of the reset signal, however, is outside of the SOA gain curve, on the short-wavelength side; the reset signal is absorbed by the SOA, thereby generating charge carriers and decreasing the refractive index.

XPM shifts the position of the Bragg resonance relative to the bistable signal, which has the effect of shifting the bistable hysteresis curve, to either higher or lower input powers. Set and reset occur when the upward and downward switching thresholds, respectively, are shifted through the (constant) input power of the bistable signal. This control over the bistable hysteresis is noteworthy, in part, because reset can be performed with ‘positive’ optical pulses. The rarity of positive-pulse reset techniques in bistable systems exhibiting a S-shaped hysteresis curve has lead some researchers to denounce them as “impossible” [98]. Although positive-pulse reset techniques have indeed been demonstrated before (e.g., using a thermal nonlinearity

in a passive semiconductor [99]), our technique works over a wide wavelength range and our nonlinear device (the DFB SOA) has the general advantages detailed at the end of Section 1.2.2. The flexible control of the nonlinear response of SOA-based bistable devices encourages further exploration; we expect the same control techniques to apply to other resonant-type SOAs and to other bistable systems based on SOAs.

The DFB SOA can be re-engineered for better performance in future experiments. The devices in our experiments were fabricated for use as directly modulated communication lasers, and were therefore engineered to have a small nonlinearity (small α) to prevent linewidth enhancement — they were multi-quantum well devices, and their Bragg wavelength was fabricated on the short-wavelength side of the gain peak. However, since the optical processing studied here is based on α , it may be beneficial to engineer a large value of α by fabricating the dominant Bragg resonance on the *long*-wavelength side of the gain peak [100], and by using a *bulk* semiconductor active region. A larger α would allow the same change in the refractive index for a smaller change in gain; this would allow the Bragg resonance to remain relatively unsaturated and hence yield a higher on-state amplification and a larger on–off contrast ratio. Ideally, a ratio of 15 dB can be achieved, which is more appropriate for light-wave systems than the 6–8 dB measured in our experiments. Devices with higher α , however, would also exhibit a lower differential gain dg/dN , thereby requiring a stronger injection current to achieve the same gain; this would limit the maximum number density of DFB SOAs even further, but may not be a problem for applications requiring only a couple of devices.

The all-optical flip–flop is a building block to enable digital signal-processing functions that require memory. As an example, we simulated data-format conversion from high-speed RZ signals to low-speed NRZ signals. The high-speed signals can come from a wide range of WDM channels, and can have pulse widths shorter than the SOA carrier lifetime. The generated NRZ signals occur at the wavelength of

the bistable signal, and have long pulse widths commensurate with low-speed, local-access networks and the SOA carrier lifetime. Moreover, the conversion is implemented with only a DFB SOA and a holding-beam laser, so the heat-dissipation problem associated with a large number of closely packed devices is not an issue. Thus, this application overcomes each of the limitations of optical bistability in resonant-type SOAs that were summarized in Section 1.2.2.

Future research can explore signal-processing applications such as retiming, packet-header buffering, and temporal demultiplexing. Since set and reset signals lie in well-separated spectral bands, the all-optical flip-flop is essentially a 3-terminal device; investigations into operations analogous to those performed by electronic transistors should be rewarding. Moreover, using the integrateability of semiconductor technology, photonic circuits can be created which use the sequential processing capability of the all-optical flip-flop together with combinational photonic gates for advanced all-optical processing.

8.5 Data-Wavelength Conversion

In Chapter 7, we demonstrated the transfer of data to a 1547-nm signal (which is in the vicinity of the Bragg wavelength) from initial data signals at 1306 nm, 1466 nm, and 1560 nm. Data at 1560 nm was converted using a gain-saturating XPM technique that has been used in other SOA-based wavelength converters (e.g., MZI [89]). Conversion from the shorter wavelengths of 1306 and 1466 nm, however, was performed using a *gain-pumping* XPM technique in which the data signals decreased the refractive index. We demonstrated how the data-signal polarity can be selected by tuning the probe wavelength to different regions of the Bragg resonance. For 1306-to-1547 nm conversion, polarity-inverted signals exhibited a digital-like transfer function with on-off ratios of 4 and 2.4, at 155.5 and 622 Mb/s, respectively.

For future experiments on wavelength conversion, the bit-error rate (BER) of the

input signal and the converted signal should be measured under a variety of operating conditions. Using pseudo-random binary-sequence (PRBS) data for BER testing and for measuring the on–off ratios would also be helpful, since it simulates actual communication data. These measurements were beyond the capability of our equipment, but are important for thorough characterization and assessment.

Data-wavelength conversion was limited in speed by the inverse of the carrier lifetime to ~ 1 Gb/s. Since this rate does not surpass that achievable by electronic processing, DFB SOAs are unlikely to be implemented for wavelength conversion in their current state. Future research should focus on overcoming this speed limitation. One technique for effectively reducing the carrier lifetime uses a strong gain-saturating signal to sweep away charge carriers [101]; this technique has produced an effective τ of 10 ps. To maintain the same amount of gain, however, the SOA is driven with a stronger electrical bias and therefore generates more heat [36]. It may be possible to apply this technique to wavelength conversion in DFB SOAs for high-speed operation above 10 Gb/s.

Although the speed of this conversion process is currently limited by the carrier lifetime, our research has demonstrated two general principles: 1) XPM-based wavelength conversion using carrier *generation* can be implemented in gain-biased SOAs, and 2) bistable systems can give rise to a data-wavelength conversion process that exhibits a digital-like transfer function. Both principles are applicable to other data-wavelength conversion schemes. XPM via carrier-generating signals can be applied to any SOA wavelength converter currently based on XPM via carrier-depleting signals (e.g., [89]), and would significantly increase their wavelength range of operation. In addition, the highly beneficial digital transfer function can be sought out in other systems that exhibit bistability for the application of data-wavelength conversion.

8.6 Summary of Contributions

This thesis explored the nonlinear response and signal-processing capabilities of DFB SOAs. As evident in the preceding sections, much of our work centered on overcoming the limited wavelength range of operation exhibited by signal processing in such devices. Here, we summarize our contributions to overcoming this limitation, exploring new applications, and understanding the nonlinear response:

- Conceived and demonstrated all-optical flip–flop operation using ‘positive’ control signals that exhibit a very wide wavelength range of operation.
- Conceived and simulated data-format conversion from high-speed RZ to low-speed NRZ formats; this sequential-processing application overcomes all three major limitations of DFB SOAs for signal processing.
- Predicted an increase in the spectral range and spectral uniformity of optical bistability using chirped-grating DFB SOAs.
- Predicted a new shape of the hysteresis curve on reflection from DFB SOAs. For chirped-grating DFB SOAs, this shape exhibits ultra-high contrast ratios.
- Demonstrated data-wavelength conversion using signals that *pump* the SOA gain; this technique allows 1310-to-1550 nm conversion and is applicable to other SOA-based conversion schemes.
- Demonstrated an inherent, digital-like transfer function for data-wavelength conversion.
- First demonstration of all-optical flip–flop operation and data-wavelength conversion using a DFB SOA.

These contributions deepen the understanding of the nonlinear response and signal-processing capabilities of DFB SOAs, and significantly advance their application to fiber-optic communication networks.

Bibliography

- [1] “Optical Networking,” Global Fundamental Equity Research Group, Merrill Lynch, February (2000).
- [2] A. Hadjifotiou, “Optical Components for Future Optical Communication Systems,” Plenary Talk, *Optical Amplifiers and Their Applications*, IWA1, Quebec, CA, July (2000).
- [3] G.P. Agrawal, *Fiber-Optic Communication Systems*, New York: Wiley-Interscience, 1992, chapter 7.
- [4] R. C. Alferness, “WDM Networking Elements and Their Enabling Technologies,” Short Course 138, Optical Fiber Communications (OFC) Conference, Baltimore, MA (2000).
- [5] J. P. Ryan and M. Steinberg, “WDM and Optical Networks: Market Directions,” *Optics and Photonics News*, 25–28, February (1999).
- [6] J. Leuthold, C. H. Joyner, B. Mikkelsen, G. Raybon, J. L. Pleumeekers, B. I. Miller, K. Dreyer, and C. A. Burrus, “100 Gbit/s All-Optical Wavelength Conversion with an Integrated SOA Delayed Interference Configuration,” *Optical Amplifiers and Their Applications*, OWB3, Quebec, CA, July (2000).
- [7] G. P. Agrawal and N. A. Olsson, “Self-Phase Modulation and Spectral Broadening of Optical Pulses in Semiconductor Laser Amplifiers,” *IEEE J. Quantum Electron.* **25**, 2297–2306 (1989).
- [8] N. A. Olsson, “Semiconductor Optical Amplifiers,” *Proc. IEEE*, **80**, 375–382 (1992).
- [9] W. F. Sharfin and M. Dagenais, “High Contrast, 1.3 μm Optical AND Gate with Gain,” *Appl. Phys. Lett.* **48**, 1510–1512 (1986).
- [10] K. Otsuka and H. Iwamura, “Analysis of a Multistable Semiconductor Light Amplifier,” *IEEE J. Quantum Electron.* **19**, 262–263 (1983).

- [11] T. Nakai, N. Ogasawara, and R. Ito, "Optical Bistability in a Semiconductor Laser Amplifier," *Jpn. J. Appl. Phys.* **22**, 1184–1186 (1983).
- [12] K. Otsuka and S. Kobayashi, "Optical Bistability and Nonlinear Resonance in a Resonant-Type Semiconductor Laser Amplifier," *Electronic Lett.* **19**, 262–263 (1983).
- [13] K. Otsuka and H. Iwamura, "Theory of Optical Multistability and Chaos in a Resonant-Type Semiconductor Laser Amplifier," *Phys. Rev. A* **28**, 3153–3155 (1983).
- [14] H. J. Westlake, M. J. Adams, and M. J. O'Mahony, "Measurement of Optical Bistability in an InGaAsP Laser Amplifier at 1.5 μm " *Electronic Lett.* **21**, 992–993 (1985).
- [15] W. F. Sharfin and M. Dagenais, "Nonlinear Semiconductor Laser Amplifiers as Low-Energy Optical Switches," in *Optical Bistability III*, H. M. Gibbs, P. Mandell, N. Peyghambarian, S. D. Smith, Ed. Berlin: Springer, 1986.
- [16] H. Kawaguchi, "Absorptive and Dispersive Bistability in Semiconductor Injection Lasers," *Opt. and Quantum Electron.* **19**, S1–S36 (1987).
- [17] M.J. Adams, "Optical amplifier bistability on reflection," *Opt. Quantum Electron.* **19**, S37–S45 (1987).
- [18] M. J. Adams, "Physics and Applications of Optical Bistability in Semiconductor Laser Amplifiers," *Solid-State Electron.* **30**, 43–51 (1987).
- [19] W. F. Sharfin and M. Dagenais, "Physics of Low Energy Optical Switching," *Proc. SPIE* **860**, 154–160 (1987).
- [20] Z. Pan, H. Lin, and M. Dagenais, "Switching Power Dependence on Detuning and Current in Bistable Diode Laser Amplifiers," *Appl. Phys. Lett.* **58**, 687–689 (1991).
- [21] P. Pakdeevanich and M. J. Adams, "Switching Powers for Optical Bistability in a Semiconductor Laser Above and Below Threshold," *Optics Comm.* **176**, 195–198 (2000).
- [22] H. Kawaguchi, "Multiple Bistability and Multistability in a Fabry–Perot Laser Diode Amplifier," *IEEE J. Quantum Electron.* **23**, 1429–1433 (1987).

- [23] N. Ogasawara and R. Ito, "Static and Dynamic Properties of Nonlinear Semiconductor Lasers Amplifiers," *Jpn. J. Appl. Phys.* **25**, L739–L742 (1986).
- [24] K. Inoue, "High-Speed All-Optical Gate Switching Experiment in a Fabry–Perot Semiconductor Laser Amplifier," *Electron. Lett.* **23**, 921–922 (1987).
- [25] H. Kawaguchi, H. Tani, K. Inoue, "Optical Bistability Using a Fabry–Perot Semiconductor-Laser Amplifier with Two Holding Beams," *Opt. Lett.* **12**, 513–515 (1987).
- [26] R. P. Webb, "Error-Rate Measurements on an All-Optically Regenerated Signal," *Opt. Quantum Electron.* **19**, S57–S60 (1987).
- [27] M. Dagenais and W. F. Sharfin, "Bistable Diode Laser Amplifiers in High Performance Optical Communication and Optical Computing Systems," *Proc. SPIE* **881**, 80–91 (1988).
- [28] Z. Pan and M. Dagenais, "Bistable Diode Laser Amplifiers as Narrow Bandwidth High-Gain Filter for Use in Wavelength Division Demultiplexing," *IEEE Photon. Tech. Lett.* **4**, 1054–1057 (1992).
- [29] D. Psaltis and N. Farhat, "Optical Information Processing Based on an Associative-Memory Model of Neural Nets with Thresholding and Feedback," *Opt. Lett.* **10**, 98–100 (1985).
- [30] K. Inoue, "All-Optical Flip-Flop Operation in an Optical Bistable Device Using Two Lights of Different Frequencies," *Opt. Lett.* **12**, 918–920 (1987).
- [31] W. F. Sharfin and M. Dagenais, "Room Temperature Optical Bistability in In-GaAsP/InP Amplifiers and Implications for Passive Devices," *Appl. Phys. Lett.* **46**, 819–821 (1985).
- [32] P. Likamwa, A. Miller, M. Ogawa, and R. M. Park, "All-Optical Bistable Switching in an Active InGaAs Quantum-Well Waveguide," *IEEE Photon. Tech. Lett.* **3**, 507–509 (1991).
- [33] D. A. H. Mace, M. J. Adams, and C. Seltzer, "Multi-Quantum Well Amplifier Optical Bistability" *Electron. Lett.* **27**, 1363–1365 (1991).
- [34] M. J. Adams, H. J. Westlake, M. J. O'Mahony, and I. D. Henning, "A Comparison of Active and Passive Optical Bistability in Semiconductors," *IEEE J. Quantum Electron.* **21**, 1498–1504 (1985).

- [35] W. F. Sharfin and M. Dagenais, "Femtojoule Optical Switching in Nonlinear Semiconductor Laser Amplifiers" *Appl. Phys. Lett.* **48**, 321–322 (1986).
- [36] W. F. Sharfin and M. Dagenais, "Dynamics of Optically Switched Bistable Diode Amplifiers" *IEEE J. Quantum Electron.* **23**, 303–308 (1987).
- [37] H. J. Westlake, M. J. Adams, and M. J. O'Mahony, "Assessment of Switching Speed of Optical Bistability in Semiconductor Laser Amplifier," *Electron. Lett.* **22**, 541–543 (1986).
- [38] M. J. Adams, "Time Dependent Analysis of Active and Passive Optical Bistability in Semiconductors," *IEE Proceedings*, Pt. J **132**, 343–348 (1985).
- [39] M. J. Adams, "A Tentative Assessment of Semiconductor Laser Optical Bistability" *Int. J. Electron.* **60**, 123–142 (1986).
- [40] M. J. Adams, H. J. Westlake, and M. J. O'Mahony, "Optical Bistability in 1.55 μm Semiconductor Laser Amplifiers," in *Optical Bistability III*, H. M. Gibbs, P. Mandell, N. Peyghambarian, S. D. Smith, Ed. Berlin: Springer, 1986.
- [41] H. G. Winful, J. H. Marburger, and E. Garmire, "Theory of Bistability in Nonlinear Distributed Feedback Structures," *Appl. Phys. Lett.* **35**, 379–381 (1979).
- [42] H. Kawaguchi, K. Inoue, T. Matsuoka, and K Otsuka, "Bistable Output Characteristics in Semiconductor Laser Injection Locking" *IEEE J. Quantum Electron.* **21**, 1314–1317 (1985).
- [43] M. J. Adams and R. J. Wyatt, "Optical Bistability in Distributed Feedback Semiconductor Laser Amplifiers," *IEE Proc.*, Pt. J **134**, 35–40 (1987).
- [44] R. Wyatt and M. J. Adams, "Optical Bistability in Active Distributed-Feedback Structures: An Experimental and Theoretical Study," *CLEO '86 MB5*, San Francisco, CA (1986).
- [45] R. Calvani, M. Calzavara, and R. Caponi, "Steady-State and Dynamic Characteristics of Bistable DFB Amplifiers for All-Optical Switching," *Proc. SPIE* **1787**, 134–141 (1992).
- [46] R. Hui and A. Sapia, "Nonlinearity Difference in the Two Passbands of a Distributed- Feedback Semiconductor Laser Amplifier," *Opt. Lett.* **15**, 956–958 (1990).
- [47] K. Magari, H. Kawaguchi, K. Oe, and M. Fukuda, "Optical Narrow-Band Fil-

- ters Using Optical Amplification with Distributed Feedback,” *IEEE J. Quantum Electron.* **24**, 2178–2190 (1988).
- [48] G. H. M. van Tartwijk, H. de Waardt, B. H. Verbeek, and D. Lenstra, “Resonant Optical Amplification in a Laser Diode: Theory and Experiment,” *IEEE J. Quantum Electron.* **30**, 1763–1768 (1994).
- [49] N. Chinone and M. Okai, “Distributed Feedback Semiconductor Lasers,” in *Semiconductor Lasers: Past, Present, and Future*, G.P.Agrawal, Ed. New York: AIP Press, 1995, Chapter 2.
- [50] H. A. Haus and C. V. Shank, “Antisymmetric Taper of Distributed Feedback Lasers,” *IEEE J. Quantum Electron.* **12**, 532–539 (1976).
- [51] H. Kogelnik and C. V. Shank, “Coupled-Wave Theory of Distributed Feedback Lasers,” *J. Appl. Phys.* **43**, 2327–2335 (1972).
- [52] J. T. Verdeyen, *Laser Electronics*, 3rd ed., London: Prentice, 1995, Chapter 12.
- [53] L. M. Magid, *Electromagnetic Fields, Energy, and Waves*, New York: John Wiley & Sons, 1972, Chapter 9.
- [54] K. David, J. Buus, and R. Baets, “Basic Analysis of AR-Coated, Partly Gain-Coupled DFB Lasers: The Standing Wave Effect,” *IEEE J. of Quantum Electron.* **28**, 427–433 (1992).
- [55] G. P. Agrawal and N. K. Dutta, *Semiconductor Lasers*, 2nd ed. New York: Van Nostrand Reinhold, 1993.
- [56] O. Svelto, *Principles of Lasers*, 3rd ed. New York: Plenum Press, 1989, Chapter 7.
- [57] R. W. Boyd, *Nonlinear Optics*, New York: Academic Press, 1992, Chapter 6.
- [58] C. H. Henry, “Theory of the Linewidth of Semiconductor Lasers,” *IEEE J. Quantum Electron.* **18**, 259–264 (1982).
- [59] G. B. H. Thompson, “A Theory for Filamentation in Semiconductor Lasers Including the Dependence of Dielectric Constant Injected Carrier Density,” *Opto-Electron.* **4**, 257–310 (1972).
- [60] A. K. Jonscher and M. H. Boyle, “The Flow of Carriers and its Effect on the Spatial Distribution of Radiation from Injection Lasers,” *Institute of Physics and Physical Society Symposium on Gallium Arsenide*, 78–84 (1966).

- [61] R. J. Manning, A. D. Ellis, A. J. Poustie, and K. J. Blow, "Semiconductor Laser Amplifiers for Ultrafast All-Optical Signal Processing," *J. Opt. Soc. Am. B* **14**, 3204–3216 (1997).
- [62] M. Yamada and K. Sakuda, "Analysis of Almost-Periodic Distributed Feedback Slab Waveguides Via a Fundamental Matrix Approach," *Appl. Opt.* **26**, 3474–3478 (1987).
- [63] P. Mandel, S. D. Smith, and B. S. Wherrett, *From Optical Bistability Towards Optical Computing: The EJOB Project*, London: North Holland, 1987, Chapter 4.
- [64] D. N. Maywar and G. P. Agrawal, "Transfer-Matrix Analysis of Optical Bistability in DFB Semiconductor Laser Amplifiers with Nonuniform Gratings," *IEEE J. Quantum Electron.*, **33**, 2029–2037 (1997).
- [65] D. N. Maywar and G. P. Agrawal, "Low-Power All-Optical Switching in Active Semiconductor Chirped Periodic Structures," *Optics Express* **3**, 440–446 (1998).
- [66] D. N. Maywar, G. P. Agrawal, and Y. Nakano, "Optical Switching and Memory in Chirped-Grating DFB Amplifiers," IEICE Conference, Osaka, Japan, (1999).
- [67] D. N. Maywar and G. P. Agrawal, "Effect of Chirped Gratings on Reflective Optical Bistability in DFB Semiconductor Laser Amplifiers," *IEEE J. Quantum Electron.*, **34**, 2364–2370 (1998).
- [68] A. D. Lloyd, I. Janossy, H. A. Mackenzie, and B. S. Wherrett, "CW Optical Bistability in Non-Absorbing Liquids and Liquid Crystals," *Opt. Commun.* **61**, 339–344 (1987).
- [69] D. C. Hutchings, A. D. Lloyd, I. Janossy, and B. S. Wherrett, "Theory of Optical Bistability in Metal-Mirrored Fabry-Perot Cavities Containing Thermo-Optic Materials," *Opt. Commun.* **61**, 345–350 (1987).
- [70] G. Assanto and R. Zanonì, "Almost-Periodic Nonlinear Distributed Feedback Gratings," *Opt. Acta* **34**, 89–101 (1987).
- [71] G. Assanto, R. Zanonì, and G. I. Stegeman, "Effects of Taper in Nonlinear Distributed Feedback Gratings," *J. Mod. Opt.* **35**, 871–883 (1988).
- [72] S. Radic, N. George, and G. P. Agrawal, "Analysis of Nonuniform Nonlinear

- Distributed Feedback Structures: Generalized Transfer Matrix Method,” *IEEE J. Quantum Electron.* **31**, 1326–1336 (1995).
- [73] J. Liu, C. Liao, S. Liu, and W. Xu, “The Dynamics of Direction-Dependent Switching in Nonlinear Chirped Gratings,” *Opt. Commun.* **130**, 295–301 (1996).
- [74] H. Kogelnik, “Filter Response of Nonuniform Almost-Periodic Structures,” *Bell System Tech. J.* **55**, 109–126 (1976).
- [75] M. Yamada and K. Sakuda, “Adjustable Gain and Bandwidth Light Amplifiers in Terms of Distributed Feedback Structures,” *J. Opt. Soc. Am. A* **4**, 69–76 (1987).
- [76] G. P. Agrawal and A. H. Bobeck, “Modeling of Distributed Feedback Semiconductor Lasers with Axially-Varying Parameters,” *IEEE J. Quantum Electron.* **24**, 2407–2414 (1988).
- [77] H. Ghafouri-Shiraz, B. S. K. Lo, and C. Y. J. Chu, “Structural Dependence of Three Phase-Shift Distributed Feedback Semiconductor Laser Diodes at Threshold Using the Transfer Matrix Method,” *Semiconductor Science and Technology* **9**, 1126–1132 (1994).
- [78] P. Meystre, “On the Use of the Mean-Field Theory in Optical Bistability,” *Optics Comm.* **26**, 277–280 (1978).
- [79] S. Nakamura, Y. Ueno, and K. Tajima, “Error-Free All-Optical Data Pulse Regeneration at 84 Gbps and Wavelength Conversion at 168 Gbps with Symmetric Mach-Zehnder All-Optical Switches,” *Optical Amplifiers and Their Applications*, PDP4, Quebec, CA, July (2000).
- [80] S. Diez, C. Schubert, U. Feist, R. Ludwig, J. Berger, H. G. Weber, “160 Gb/s All-Optical Demultiplexing Using a Gain-Transparent Ultrafast-Nonlinear Interferometer,” *Optical Amplifiers and Their Applications*, PDP9, Quebec, CA, July (2000).
- [81] P. Horowitz and W. Hill, *The Art of Electronics*, 2nd ed., New York: Cambridge University Press, 1989, Chapter 8.
- [82] H. Kawaguchi, I. H. White, M. J. Offside, and J. E. Carrol, “Ultrafast Switching in Polarization-Bistable Laser Diodes,” *Opt. Lett.* **17**, 130–132 (1992).
- [83] K. Nonaka, H. Tsuda, H. Uenohara, H. Iwamura, and T. Kurokawa, “Opti-

- cal Nonlinear Characteristics of a Side-Injection Light-Controlled Laser Diode with a Multiple-Quantum-Well Saturable Absorption Region,” *IEEE Photon. Tech. Lett.* **5**, 139–141 (1993).
- [84] D. N. Maywar, G. P. Agrawal, and Y. Nakano, “All-Optical Hysteresis Control via Cross-Phase Modulation in Semiconductor Optical Amplifiers,” submitted to *J. Opt. Soc. Am. B*.
- [85] D. N. Maywar, G. P. Agrawal, and Y. Nakano, “Robust Optical Control of an Optical-Amplifier-Based Flip–Flop,” *Optics Express* **6**, 75–80 (2000).
- [86] A. E. Willner and W. Shieh, “Optimal Spectral and Power Parameters for All-Optical Wavelength Shifting — Single Stage, Fanout, and Cascadability,” *IEEE J. Lightwave Tech.* **13**, 771–781 (1995).
- [87] M. J. Adams, D. A. O. Davies, M. C. Tatham, and M. A. Fisher, “Nonlinearities in Semiconductor Laser Amplifiers,” *Opt. Quantum Electron.* **27**, 1–13 (1995).
- [88] I. Cha, M. Kitamura, H. Honmou, and I. Mito, “1.5 μm Band Travelling-Wave Semiconductor Optical Amplifiers with Window Facet Structure,” *Electron. Lett.* **25**, 1241–1242 (1989).
- [89] T. Durhuus, C. Joergensen, B. Mikkelsen, R. J. S. Pedersen, and K. E. Stubkjaer, “All Optical Wavelength Conversion by SOA’s in a Mach-Zehnder Configuration,” *IEEE Photon. Tech. Lett.* **6**, 53–55 (1994).
- [90] B. Glance, J. M. Wiesenfeld, U. Koren, A. H. Gnauck, H. M. Presby, and A. Jourdan, “High Performance Optical Wavelength Shifter,” *Electron. Lett.* **28**, 1714–1715 (1992).
- [91] J. P. R. Lacey, G. J. Pendock, and R. S. Tucker, “All-Optical 1300-nm to 1500-nm Wavelength Conversion Using Cross-Phase Modulation in a Semiconductor Optical Amplifier,” *IEEE Photonics Tech. Lett.* **8**, 885–887 (1996).
- [92] C. Q. Xu, H. Okayama, and M. Kawahara, “1.55 μm Band Efficient Broadband Wavelength Conversion by Difference Frequency Generation in a Periodically Domain-Inverted LiNbO₃ Channel Waveguide,” *Appl. Phys. Lett.* **63**, 3559–3561 (1993).
- [93] D. Mahgerefteh and M. W. Chbat, “All-Optical 1.5 μm to 1.3 μm Wavelength Conversion in a Walk-Off Compensating Nonlinear Optical Loop Mirror,” *IEEE Photonics Tech. Lett.*, **7**, 497–499 (1995).

- [94] P. E. Barnsley and P. J. Fiddymment, "Wavelength Conversion from 1.3 to 1.55 μm Using Split Contact Optical Amplifiers," *IEEE Photonics Tech. Lett.* **3**, 256–258 (1991).
- [95] D. N. Maywar, Y. Nakano, and G. P. Agrawal, "1.3-to-1.5 μm Wavelength Conversion by Optically Pumping a Distributed Feedback Amplifier," *IEEE Photonics Tech. Lett.* **12**, 858–860 (2000).
- [96] N. D. Sankey, D. F. Prelewitz, and T. G. Brown, "All-Optical Switching in a Nonlinear Periodic-Waveguide Structure," *Appl. Phys. Lett.* **60**, 1427–1429 (1992).
- [97] T. Tajima, K. Hayashi, D. N. Maywar, W. Asawamethapant, and Y. Nakano, "Fabrication of a Bistable Distributed Feedback Laser Amplifier with a Completely Linear Chirped Grating by Electron Beam Lithography," submitted to International Semiconductor Laser Conference, San Francisco, CA (2000).
- [98] K. Otsuka, "All-Optical Flip-Flop Operations in a Coupled-Element Bistable Device," *Electron. Lett.* **24**, 800–801 (1988).
- [99] S. S. Tarng, K. Tai, J. L. Jewell, H. M. Gibbs, A. C. Gossard, S. L. McCall, A. Passner T. N. C. Venkatesan, and W. Wiegmann, "External Off and On Switching of a Bistable Optical Device," *Appl. Phys. Lett.* **40**, 205–210 (1982).
- [100] G. Ogita, M. Yano, and H. Imai, "Theoretical Calculation of the Linewidth Enhancement Factor of DFB Lasers," *Electron. Lett.* **22**, 580–581 (1986).
- [101] R. J. Manning, and D. A. O. Davies, and J. K. Lucek, "Recovery Rates in Semiconductor Laser Amplifiers: Optical and Electrical Bias Dependencies," *Electron. Lett.* **30**, 1233–1234 (1994).

Appendix A

DFB SOA used in Experiments

The DFB SOA used for the experimental results reported in this thesis was fabricated to be used as a DFB diode laser in communication systems. We operated this commercial device as a resonant-type SOA by biasing it below lasing threshold (15 mA at 20 C). Its ASE spectrum is shown in Fig. A.1. The Bragg wavelength (≈ 1547 nm) was fabricated on the short-wavelength side of the SOA gain peak (≈ 1567 nm), which yields a relatively small value of the linewidth enhancement factor α (useful for directly modulated communication lasers). The dominant Bragg resonance is located near the center of the photonic bandgap, as shown in the inset; its location within the photonic bandgap is determined by the grating phase at the facets of the SOA. One facet was covered with a high-reflectivity (HR) coating, and the other with an anti-reflection (AR) coating.

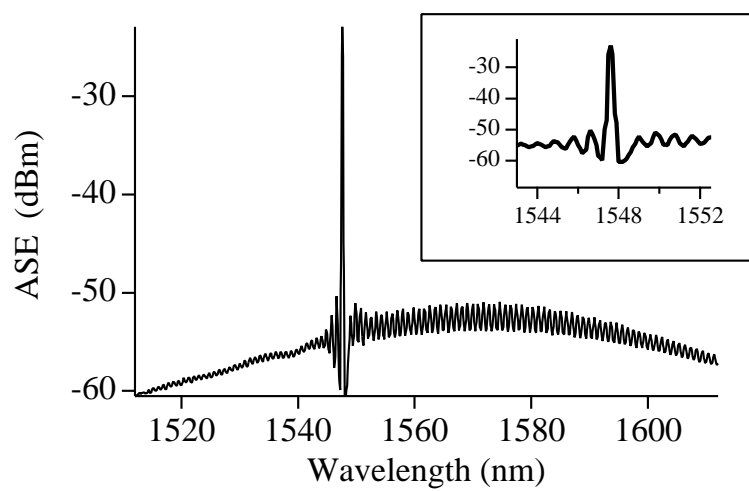


Figure A.1: ASE spectrum of the DFB SOA used in experiments.

Appendix B

Mounting Procedure

DFB SOAs were mounted onto a heatsink covered with a layer of tin, which bonds to the SOA chips and provides electrical contact. This process was performed with a wire-bonding machine, which is typically used to bond thin contact wires onto semiconductor lasers and amplifiers. We use the system only for its heat-generating capability, and use its wire-bonding probe to push the SOA chip into the tin. DFB SOAs were mounted to heatsink using the following method.

1. Adjust Dai Bonder stage so that the wire-bonding needle can raise above the heat sink.
2. Get heat sinks, which are kept in a vacuum box to avoid oxidation.
 - (a) To open box: open side valve, then open lid
 - (b) To seal box:
 - i. open gas tank, counter clockwise
 - ii. adjust pressure to give an output reading of 1
 - iii. adjust gauge to raise ball to top of red line
 - iv. open both box valves

v. wait about 3 minutes and then close in reverse order

3. Make sure heatsink fits into base correctly by considering:

- width of heatsink
- height of fixing hole
- flatness of heatsink top

4. Place heat sink in Dai Bonder. This requires an extra, dummy heatsink for a tight fit.

5. Place laser chip on heatsink. When grabbing the laser chip:

- the non-waveguide sides of the chip have purple coloring, visible without a microscope
- use the sharp tweezers

6. N-side down.

- p-side identification
 - distinct shape of gold-colored contact
 - laser stripe is visible; If the lighting angle is poor, use the point of the bonder as a mirror
 - smooth and shiny surface
- n-side identification
 - rectangular shape of gold-colored contact

- no laser stripe
- gold region is relatively rough and dull
- flip chip by using tape and tweezers

7. Position laser chip on heatsink.

- position face of laser *perpendicular* to heat-sink edge (most important)
- position in middle of heatsink
 - for fiber alignment
 - so there is room for lenses to get close to the laser chip
- position the laser close to one edge
- use the probe to move the chip into place
 - adjust height of probe
 - move slowly

8. Mount.

- adjust height of probe so that it can fall half way down the laser chip, to avoid cracking the laser chip when applying pressure
- turn on heat switch (make sure LINE is off)
- turn heat dial past 400 C
- at about 300 C (determined by the tin), press the chip into the tin using the point of the wire bonder; chips have popped off of the heatsink before, so press well

- hold until about 360 C, or until an imprint is formed in the tin
- turn the heat dial back to 0 C (further increase in temp only increases the amount of oxidation on the heatsink)
- use hair dryer (set to COLD) to cool device below 100 C before removing

9. Record.

- write code number on heatsink, or on heatsink holder
- write position of chip on heatsink in record book, as well as the beginning and ending temperatures of the mounting process

10. Let heatsink cool down one day before using in experiments.